Numerical and Experimental Investigation of Particle Separation and Flow Behavior Inside an Induction Crucible Furnace

By the Faculty of Mechanical, Process and Energy Engineering
of the Technische Universität Bergakademie Freiberg
approved

THESIS

to attain the academic degree of
Doktor-Ingenieur
(Dr.-Ing),

submitted

by M.Sc. Amjad Asad
born on the July 19, 1987 in Damaskus

Reviewers: Prof. Dr.-Ing. habil. Rüdiger Schwarze, TU Bergakademie Freiberg
Prof. Dr.-Ing. Olena Volkova, TU Bergakademie Freiberg

Date of the award: September 16, 2020

Excerpts of this work have been published in peer-reviewed international journals:

A. Asad, C. Kratzsch, S. Dudczig, C. G. Aneziris and R. Schwarze, Numerical Study of Particle Filtration in an Induction Crucible Furnace, International Journal of Heat and Fluid Flow, 2016, vol. 62, pp. 299-312.

A. Asad, E. Werzner, C. Demuth, S. Dudczig, A. Schmidt, C.G. Christos and R. Schwarze, Numerical Modeling of Flow Conditions during Steel Filtration Experiments, Advanced Engineering Materials, 2017, vol. 19, pp. 1700085.

A. Asad, K. Bauer, K. Chattopadhyay and R. Schwarze, Numerical and Experimental Modeling of The Recirculating Melt Flow Inside an Induction Crucible Furnace, 2018, Metallurgical and Materials Transactions B, 2018, vol. 49, pp. 1378-1387.

A. Asad, K. Chattopadhyay and R. Schwarze, Effect of Turbulence Modeling on the Melt Flow and Inclusions Transport in a Steel Filtration Experiment, Metallurgical and Materials Transactions B, 2018, vol. 49, pp. 2270-2277.

A. Asad, M. Haustein, K. Chattopadhyay, C. G. Aneziris and R. Schwarze, Numerical Assessment of a Filtration Experiment Influenced by Microscale Carbon Monoxide Bubbles Arising in Steel, JOM, 2018, vol. 70, pp. 2927-2933.

A. Asad, C. G. Aneziris and R. Schwarze, Numerical Investigation of the Filtration Influenced by Micro-Scale CO-Bubbles in Steel Melt, Advanced Engineering Materials, 2019, vol. 22, pp. 1900591.

Declaration

I hereby declare that I completed this work without any improper help from a third party and without using any aids other than those cited. All ideas derived directly or indirectly from other sources are identified as such.

In the selection and in the use of materials and in the writing of the manuscript I received support from the following persons:

Professor Dr.-Ing. habil. Rüdiger Schwarze

Persons other than those above did not contribute to the writing of this thesis. I did not seek the help of a professional doctorate-consultant. Only persons identified as having done so received any financial payment from me for any work done for me.

This thesis has not previously been submitted to another examination authority in the same or similar form in Germany or abroad.

Acknowledgements

The work reported in the present dissertation was accomplished at the Institute of mechanics and fluid dynamics of the Technische Universität Bergakademie Freiberg within the frame of the Collaborative Research Center (CRC) 920 (Project-ID 169148856, Subproject B06) "Multi-Functional Filters for Metal Melt Filtration - a Contribution towards Zero Defect Materials", which is financially supported by the German Research Foundation (DFG).

I want to first express my gratitude to my doctoral supervisor Prof. Dr.-Ing. habil. Rüdiger Schwarze for his professional support.

Furthermore, I would like to thank my family: My parents and my brother for supporting me spiritually throughout writing this thesis and my life in general. My wife, Gezail has been extremely supportive of me throughout this entire process and has made countless sacrifices to help me get to this point.

Contents

Abstract

During the continuous casting, non-metallic inclusions such as deoxidation or reoxidation products may arise in steel melt due to different reactions. These inclusions have to be removed from the melt with the aim of improving the cleanliness of steel products. There are many approaches in continuous casting to enhance inclusion removal from the melt. However, this Phd thesis focuses particularly on inclusion removal by reactive cleaning and active filtration during the melt casting in an induction crucible furnace using ceramic foam filter developed in CRC 920. For this purpose, a numerical model is developed in OpenFOAM in order to simulate the melt flow and reactive cleaning as well as active filtration. Besides the numerical model, an experimental water model are created to validate the capability of the numerical model to predict the recirculating turbulent flow in the induction crucible furnace.

The results show that reactive cleaning and the formation of carbon monoxide bubbles, which arise on the inclusions, have a positive impact on the melt cleanliness. Reactive cleaning can improve inclusion removal and enhance the melt cleanliness sufficiently. Based on the results, one can conclude that the rate of inclusion removal in case of reactive cleaning is considerably higher than that in case of active filtration. Furthermore, the results indicate the considerable influence of filter position and filter number on the flow field as well as on the cleaning efficiency in the induction crucible furnace. Moreover, the results shows that turbulence modeling has a considerable impact on the prediction of the melt flow and inclusion dispersion in the induction crucible furnace.

List of Figures

List of Tables

Nomenclature

Abbreviations

CFD	Computational fluid dynamics
CFFs	Ceramic foam filters
CRC	Collaborative Research Center
CT	Computed tomography
CW	Continuous waver
DNS	Direct numerical simulation
DPM	Discrete phase model
DRW	Discrete random walk
FVM	Finite volume method
HD	Hydrodynamic
ICF	Induction crucible furnace
ICF1	Reference induction crucible furnace
ICF2	Induction crucible furnace investigated at TU Freiberg
ILES	Implicit Large Eddy Simulation
LBM	Lattice Boltzmann method
LES	Large Eddy Simulation
LPT	Lagrangian particle tracking
MHD	Magnetohydrodynamic
MRF	Multi-reference frame

PIV	Particle image velocimetry
PTV	Particle tracking velocimetry
ppi	Pores per inch
RANS	Reynolds-averaged Navier-Stokes
SAS	Scale-adaptive simulation
SCS	Steel casting simulator
SEM	Scanning electron microscope
SST	Shear-stress transport
URANS	Unsteady Reynolds-averaged Navier-Stokes
VOF	Volume of Fluid
WALE	Wall-adapting local eddy-viscosity

Latin Symbols

$\boldsymbol{A}$	Magnetic vector potential	$\mathrm{V\,s\,m^{-1}}$
A_p	Surface of an inclusion	$\mathrm{m^2}$
a_1, b_1, c_1	Constants in the SST $k-\omega$ turbulence model	–
$\boldsymbol{B}$	Magnetic field induction	T
$C_\mathrm{D}, C_\mathrm{VM}, C_\mathrm{L}$	Drag, virtual mass, lift coefficient	–
C_LD	Dimensioned lift coefficient	–
C, C_μ, C_s	Constants in the SST $k-\omega$ SAS turbulence model	–
C_ω	Constant in the WALE turbulence model	–
$CD_{\mathrm{k}\omega,\mathrm{min}}$	Constant in the SST $k-\omega$ turbulence model	–
CFL	Courant number	–
C_0, C_1	Coefficients in the relation of filtration coefficient	$\mathrm{m^{-1}}$
C_2	Coefficient in the relation of filtration coefficient	–
c	Concentration of carbon	$\mathrm{mol\,m^{-3}}$
c_avg	Volume-averaged concentration of carbon	$\mathrm{mol\,m^{-3}}$

c_{b1}	Constant used for linear increase of volume	$\mathrm{m^3 s^{-1}}$
c_{b2}	Constant used for exponential increase of volume	$\mathrm{s^{-1}}$
c_{min}	Minimal prescribed concentration of carbon	$\mathrm{mol\,m^{-3}}$
D	Diffusion coefficient	$\mathrm{m^2\,s^{-1}}$
D_{p}	Pore diameter	m
$\boldsymbol{d}$	Random vector in dispersion model	$-$
d	Diameter	m
d_{f}	Dimension of filter	m
E	Electrical field intensity	$\mathrm{kg\,m\,s^{-3}\,A^{-1}}$
F_1, F_2	Blending functions for SST $k-\omega$ turbulence model	$-$
F_3	Limitation function for SST $k-\omega$ turbulence model	$-$
F_{SAS}	Constant in SST $k-\omega$ SAS turbulence model	$\mathrm{m^2\,s^{-3}}$
$\boldsymbol{F}_{\mathrm{tot}}$	Total forces acting on inclusions	N
$\boldsymbol{F}_{\mathrm{B}}, \boldsymbol{F}_{\mathrm{G}}$	Buoyancy, gravitational force	N
$\boldsymbol{F}_{\mathrm{D}}, \boldsymbol{F}_{\mathrm{VM}}$	Drag, virtual mass force	N
$\boldsymbol{F}_{\mathrm{L}}, \boldsymbol{F}_{\mathrm{EM}}$	Lift, electromagnetic pressure force	N
f	Frequency	$\mathrm{s^{-1}}$
$\boldsymbol{f}_{\mathrm{lor}}$	Lorentz force	$\mathrm{N\,m^{-3}}$
g	Gravitational acceleration magnitude	$\mathrm{m\,s^{-2}}$
$\boldsymbol{g}$	Gravitational acceleration vector	$\mathrm{m\,s^{-2}}$
H_{f}	Immersion depth of filter	m
H_1, H_2, H_{c}	Dimensions of crucibles	m
I	Time harmonic current	A
$\boldsymbol{J}$	Induced eddy current	A
$\boldsymbol{j}$	Eddy current density	$\mathrm{A\,m^{-2}}$
k	Turbulent kinetic energy	$\mathrm{m^2\,s^{-2}}$
k_{r}	Reaction constant rate	$\mathrm{mol\,m^{-2}\,s^{-1}}$
L_{vk}	Von-Kármán length	m

L_{T}	Turbulent length scale	m
L_{ch}	Characteristic length	m
l_{k}	Kolmogorow length scale	m
m	Mass	kg
$N_{\mathrm{t,p}}$	Total number of inclusions	–
n	Rotational speed	min^{-1}
n	Amount of substance after the reaction	mol
n_0	Current amount of substance	mol
n_{min}	Minimum number of inclusions or bubbles in a cell	–
n_{p}	Number of inclusions in a cell	–
n_{r}	Refractive index	–
P_{k}, $\hat{P}_{\mathrm{k}}$	Production of turbulent kinetic energy	$\mathrm{kg\,s^{-3}\,m^{-1}}$
P_{ω}	Production of specific dissipation	$\mathrm{kg\,s^{-3}\,m^{-1}}$
P_{SAS}	Source term in ω-equation	$\mathrm{m^2\,s^{-3}}$
p	Pressure	$\mathrm{kg\,m^{-1}\,s^{-2}}$
R	Gas constant	$\mathrm{kg\,m^2 s^{-2}}$
		$\mathrm{mol^{-1} K^{-1}}$
$\mathrm{R_m}$	Magnetic Reynolds number	–
Re	Reynolds number	–
$\mathrm{Re_p}$	Reynolds number of particle	–
Re_{ω}	Shear Reynolds number	–
R_1, R_2, R_3	Dimensions of crucibles	m
$R_{\mathrm{c1}}, R_{\mathrm{c2}}$	Dimensions of coil	m
$\underline{\boldsymbol{S}}$	Strain rate tensor	s^{-1}
S	Magnitude of strain rate tensor	s^{-1}
$\underline{\boldsymbol{S}}_{\mathrm{d}}$	Deviatoric symmetric part of the	s^{-1}
	square of the velocity gradient tensor	
$\boldsymbol{S}_{\mathrm{filter}}$	Pressure drop in filter	$\mathrm{N\,m^{-3}}$

S_k	Sink term in the transport equation of carbon	$\mathrm{mol\,m^{-3}\,s^{-1}}$
Sc	Schmidt number	–
T	Temperature	K
T_1, T_2	Functions in the SST $k-\omega$ SAS turbulence model	–
t	Time	s
$\boldsymbol{U}_\mathrm{rel}$	Relative velocity between bubble and inclusion	$\mathrm{m\,s^{-1}}$
$\boldsymbol{u}$	Flow velocity	$\mathrm{m\,s^{-1}}$
$u_\mathrm{p,term}$	Particle terminal velocity	$\mathrm{m\,s^{-1}}$
$\boldsymbol{u}_\mathrm{rel}$	Relative velocity between fluid and particle	$\mathrm{m\,s^{-1}}$
u_rms	Root mean square velocity	$\mathrm{m\,s^{-1}}$
$\boldsymbol{u}'$	Fluctuating velocity components	$\mathrm{m\,s^{-1}}$
V	Volume	$\mathrm{m^3}$
$\boldsymbol{v}$	Inclusion velocity	$\mathrm{m\,s^{-1}}$
y^+	Dimensionless distance from the wall	–

Greek Symbols

α_p	Void fraction of particles	–
β	Ratio of Re_ω to Re_p	–
$\beta_1, \beta_2, \beta^*$	Constants in the SST $k-\omega$ turbulence model	–
γ	Ratio of $u_\mathrm{p,term}$ to u_rms	–
γ_1, γ_2	Constants in the SST $k-\omega$ turbulence model	–
Δ	LES-filter/grid cell size	m
Δs	Penetration depth	m
Δt	Time step	s
ΔV_b	Increase of bubble size	$\mathrm{m^3}$
δ_m	Magnetic skin thickness	m
ϵ	Turbulent dissipation	$\mathrm{m^2\,s^{-3}}$

ζ	Normally distributed random number	$-$
ζ_1	Constant in the SST $k-\omega$ SAS turbulence model	$-$
η	Efficiency/cleanliness level of melt	$-$
κ	Constant in the SST $k-\omega$ SAS turbulence model	$-$
κ_1	Permeability of filter	m^2
κ_2	Forchheimer coefficient of filter	m
Λ	Eddy integral length scale	m
λ	Filtration coefficient	m^{-1}
μ	Dynamic viscosity	$\mathrm{kg\,m^{-1}\,s^{-1}}$
μ_0	Magnetic permeability	$\mathrm{H\,m^{-1}}$
ν	Kinematic viscosity	$\mathrm{m^2\,s^{-1}}$
ν_t	Turbulent viscosity	$\mathrm{m^2\,s^{-1}}$
Π_L	Criteria for the interaction between particles and fluid	$-$
ρ	Density	$\mathrm{kg\,m^{-3}}$
σ	Electrical conductivity	$\mathrm{S\,m^{-1}}$
σ_ϕ	Constants in the SST $k-\omega$ SAS turbulence model	$-$
σ_{k1}, σ_{k2}	Constants in the SST $k-\omega$ turbulence model	$-$
$\sigma_{\omega1}, \sigma_{\omega2}$	Constants in the SST $k-\omega$ turbulence model	$-$
τ	End time	s
$\underline{\boldsymbol{\tau}}^\mathrm{mod}$	Reynolds/subgrid stress tensor	$\mathrm{kg\,s^{-2}\,m^{-1}}$
$\boldsymbol{\phi}$	Coupling term	$\mathrm{N\,m^{-3}}$
φ	Electrical potential	V
χ	Criteria for the interaction between particles	$-$
Ψ	Collision probability	$-$
ψ	Filtration probability	$-$
$\boldsymbol{\Omega}$	Vorticity	$\mathrm{s^{-1}}$
ω	Angular frequency of magnetic field	$\mathrm{s^{-1}}$
ω	Specific dissipation rate	$\mathrm{s^{-1}}$

Subscripts

0	Current/initial
b	Bubble
c	Crucible
cell	Computational cell
eff	Effective
f	Fluid
filter	Filter
lor	Lorentz
m	Magnetic
max	Maximal
min	Minimal
p	Particle/inclusion
r	Radial
rel	Relative
sgs	Subgrid scale
sys	System
t	Turbulent
x, y, z	Cartesian coordinate
ω	Shear

Superscripts

$\overline{\phi}$	Reynolds-averaged/spatial-filtered quantity
ϕ^{i}	Instantaneous value
ϕ^{n}	Current value
ϕ^{o}	Previous value
ϕ^{tot}	Total quantity

1 Introduction

The demand for cleaner steels has become more and more important to improve the performance and the mechanical properties of the final product and to produce zero-defect materials. The presence of non-metallic inclusions, which are mostly deoxidation or reoxidation products, controls among others the cleanliness of steel. If such non-metallic inclusions retain in the melt, they may agglomerate and create larger clusters, which cause internal cracks, slivers and blisters [1]. This leads to poor mechanical properties of the product. Therefore, non-metallic inclusion removal is significant to obtain high quality of steel before they are entrapped in the solidification front [2].

Ceramic foam filters (CFFs) are deployed in more than 50% of the cast iron parts nowadays in order to remove the non-metallic inclusions from the melt [3]. However, steel filtration during continuous casting has still to be more developed and better understood to enhance the filtration efficiency and steel cleanliness. Moreover, the reaction occurring at the filter surface has to be better investigated to gain better thermal and mechanical resistance of the filter and enhance its filtration efficiency. In addition, the interaction between the filter material and the melt is still not understood well. The present work is undertaken within the framework of the Collaborative Research Center 920 (CRC 920) „Multi-Functional Filters for Metal Melt Filtration - a Contribution towards Zero Defect Materials“ at Technische Universität Bergakademie Freiberg. The project aims to enhance the efficiency of the CFFs by developing and testing different filter materials. In order to test the filters under real casting conditions, a steel casting simulator (SCS) is built up [4–6]. The setup of the SCS, which consists mainly of an induction crucible furnace (ICF), a tundish and two molds, is shown in Figure 1.1. The ceramic filter is immersed in the ICF of the SCS for determining its performance. Two types of filters are developed in CRC 920, „active“

and „reactive“ filters. The filtration in case of „active“ filters is based on the deposition of inclusions on filter surface. On the other hand, the filtration by „reactive“ filters is dominated by the reaction between filter's materials and the dissolved oxygen in the steel melt to decrease the occurrence of the inclusions in the melt. Moreover, situ-layers form on the filter surface due to this reaction, which help to increase the filtration efficiency.

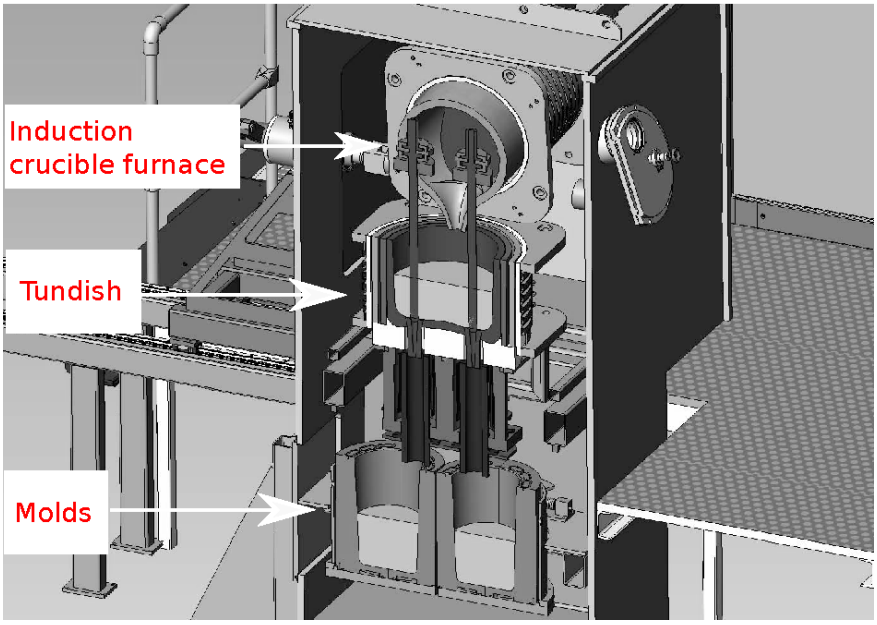

Figure 1.1: Setup of the steel casting simulator employed in the frame of CRC 920 to detect the performance of the ceramic foam filter [4].

No available measurement technique is able to describe the melt flow, active filtration and reactive cleaning of steel melt inside a real ICF because of the high temperature of the melt. This leads to the fact that computational fluid dynamics (CFD) becomes a dominant approach to model and predict such metallurgical processes.

This PhD thesis deals with simulating the melt flow in the ICF, which is a part of the SCS, investigated at TU Bergakademie Freiberg. The main topic of the thesis is reactive cleaning and active filtration of steel melts. For this purpose, a numerical model is developed in OpenFOAM to account for reactive cleaning and the filtration process in the ICF. The numerical model takes into account the effect of the Lorentz force driving the melt in the ICF as well. To consider the reaction between the dissolved oxygen and carbon dissolved from the carbon-bonded filter in case of reactive

cleaning, a transport equation of carbon is included in this model. The model is able to take into account the formation of the carbon monoxide bubbles on inclusions and on filter surface in case of reactive cleaning. Besides the reactive effect of the filters, the numerical model can consider active filtration of the non-metallic inclusions in a ceramic filter immersed inside the melt. A combination of reactive cleaning and active filtration can be considered in the model as well. In addition to the investigation of reactive cleaning and active filtration of the melt, the considerable effect of turbulence modeling on the prediction of the melt flow and inclusion transport in the ICF is clarified in the thesis.

Furthermore, the thesis presents a new experimental setup, which is built up to mimic the turbulent recirculating melt flow, similar to that in the ICF. The experimental results are used to examine the capability of the turbulence models to describe a recirculating turbulent flow.

2 State of the Art

2.1 Non-metallic Inclusions

The ductility and durability of steel products are considerably impaired by large-sized non-metallic inclusions. Non-metallic inclusions cover oxides, nitrides, carbides, sulfides and their composites and compounds [7–10]. Sulfides, nitrides and carbides arise fast during the cooling of steel below the solidus temperatures, while most of large oxide inclusions and some sulfides can form in liquid state of steel [7, 8]. These inclusions have to be removed from the liquid melt before the steel melt is solidified. Otherwise, they give rise to defects in the casting products.

Oxide inclusions in steel are divided, depending on their origin, into exogenous inclusions and endogenous inclusions [7, 8, 11]. The exogenous inclusions origin from external sources, e.g. from slag or refractory. On the contrary, the endogenous inclusions arise in the melt due to the deoxidation, reoxidation, desulfurization or other reactions during secondary metallurgical treatment. If deoxidizers are added to the melt, the deoxidation element reacts with dissolved oxygen in the steel melt. The size of inclusions, which may arise in the steel melt, differs between the exogenous and endogenous inclusions. It was reported in Koch et al. [12] that the endogenous inclusions are typically smaller than 20 µm, while the exogenous inclusions are bigger than 20 µm. The origin of inclusions in steel melt was summarized in Ling et al. [13]. Nano-scale and micro-scale inclusion phenomena were shown by Zhang et al. [14], as can be seen in Figure 2.1. The authors claimed that the nucleation of the endogenous inclusions takes place at nano-scales in time and length due to the Ostwald ripening and Brownian collisions. Moreover, the inclusions grow at micro-scales depending on other phenomena, e.g. turbulent collision and interface reactions. A similar picture of

inclusions collision depending on the dissipation rate was provided in Sahai et al. [7]. However, Haustein et al. [15] showed in their paper that the growth of inclusions because of collision and agglomeration is complexer than shown in Zhang et al. [14]. In the paper of Haustein et al. [15], the authors indicated that the inclusions collision depends on the lubrication force between the inclusions. Moreover, the shape of inclusions, inclusions diameter and flow shear rate affect the collision rate of inclusions. Figure 2.2 indicates the effect of inclusions diameter and inclusion shape on collisions coefficient. Here, it is evident that the particle cluster (star form) has higher probability to collide compared to spherical single particles, i.e. the cluster has higher collision coefficient.

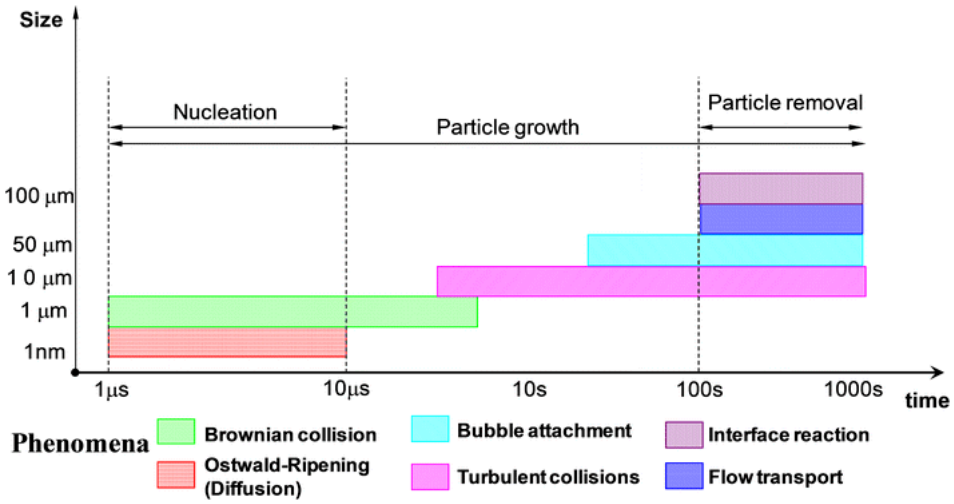

Figure 2.1: Representation of scale and control mechanism during inclusion nucleation, growth, and removal [14].

In the frame of CRC 920, the inclusions present in the steel melt were characterized either by scanning electron microscope (SEM) with energy dispersive X-ray spectroscopy or by ASPEX [17–20]. Schröder et al. [18] investigated the interaction between exogenous magnesia inclusions with endogenous inclusion in high alloyed steel melt. In this article, the authors mentioned that a liquid layer meniscus arises on the exogenous magnesia inclusions. This layer prevents the endogenous particles to agglomerate with exogenous magnesia inclusions because of the low attraction forces. Seleznev et al. [19] investigated the clustering of non-metallic inclusions in cast steel. The maximum size of clusters detected in solidified steel melt by the authors was in the range 90-160 µm.

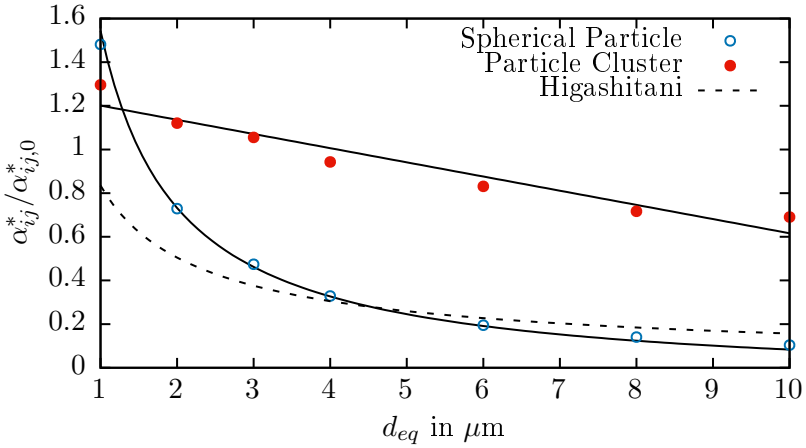

Figure 2.2: The effect of particle diameter d_{eq} and particle shape (particle cluster and spherical particle) on the normalized collision coefficient $\alpha^*_{ij}/\alpha^*_{ij,0}$ [15]. The dashed curve represents the normalized collision coefficient for spherical particles obtained according to Higashitani et al. [16].

As mentioned previously, inclusion removal is important in continuous casting to improve the cleanliness of steel. The flow behavior plays a significant role to obtain high quality of steel. It can enhance the purity of the melt by bringing the inclusions to the free surface [21]. On the other hand, the melt flow can lower the quality of steel by bringing the inclusions to the solidifying front [2]. Various control devices have been utilized in continuous casting to control the melt flow in order to enhance inclusion removal. These devices can be weirs, dams, baffles with holes, pour pads and turbulence suppresses, which have been installed especially within the tundish [8]. Morales-Higa et al. [22] designed a new ladle shroud, which can be used as a control device in the tundish in order to improve inclusion flotation to the slag layer. In addition to installing control devices, inclusion removal can be achieved by injecting argon bubbles from a porous plug in the melt [23]. The inclusions attach to the bubbles, if they come into contact (see Figure 2.3). Then, the bubbles rise and transport the inclusions to the free surface of melt or the slag layer. Moreover, the inclusions can be trapped in the argon bubble wake near to the slag and be drawn to the slag with the rising argon bubble [24]. Additionally, the agglomeration of inclusions takes place in steel melt and leads to inclusions clusters, which can float up fast and reach the slag layer due to the buoyancy [25]. Ling et al. [13] summarized the sources and the removal of inclusions in the molten steel.

The main focus of this work is inclusion removal by using active and reactive filters. Therefore, other possibilities to remove the inclusions are not considered in this work.

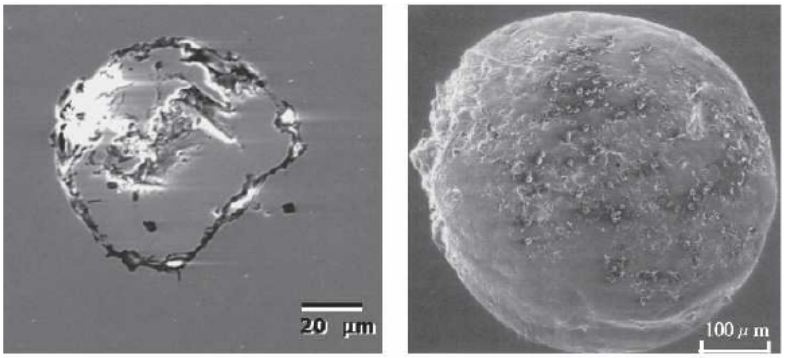

Figure 2.3: Two pictures of bubbles collecting solid inclusions [26]. The left picture shows inclusions on the surface of a bubble captured in ingot steel [27]. The right picture presents inclusions attached to a bubble in continuous cast steel [28].

2.2 Induction Crucible Furnace

The efficiency and the performance of the ceramic foam filters, which are being developed in CRC 920, are tested under real casting conditions by inserting the ceramic filters into the melt in the ICF of SCS. The basic work principle of such ICF is shown in Figure 2.4. The time harmonic current I in the coil induces an alternating magnetic field $\boldsymbol{B}$, which is concentrated in the skin layer close to the walls of the crucible due to its harmonic nature. The magnetic field induces eddy currents $\boldsymbol{J}$ in the skin layer, which interact with $\boldsymbol{B}$. The interaction between $\boldsymbol{J}$ and $\boldsymbol{B}$ results in the Lorentz force $\boldsymbol{f}_{\mathrm{lor}}$ that drives the melt in the ICF to generate one or several toroidal vortices [29, 30]. This stirring enhances the mixing and the chemical homogeneity of the melt in the ICF. Moreover, the magnetic field introduces Joule heating, which heats the melt in the ICF. The main advantage of the ICF is the contactless heating and treating of the melt, which can be important to produce pure final products [31].

The turbulent flow of the melt in the ICF has often been investigated in the last few decades due to its considerable effect on mass and heat transfer in the melt. For this purpose, many numerical and experimental models have been developed in order to study the turbulent melt flow in the ICF. An experimental model was developed by

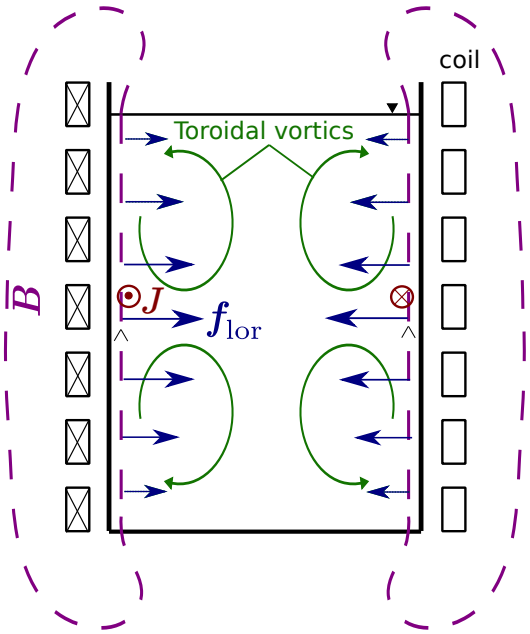

Figure 2.4: Schematic sketch presents the principle of the induction crucible furnace. The interaction between the magnetic field $\boldsymbol{B}$ and the induced eddy current $\boldsymbol{J}$ results in the Lorentz force $\boldsymbol{f}_{\mathrm{lor}}$, which drives the melt inside the induction crucible furnace [32].

Baake et al. [33] in order to measure the recirculating melt flow, taking place in the ICF. In this experimental setup, the authors used Wood's alloy as an operating fluid. This alloy has magnetic properties, which allow to induce the Lorentz force, required to recirculate the flow in the crucible. In order to determine the flow field, magnetic probes were utilized. This experiment was used in the current work to validate the numerical model.

Besides the experimental study of the ICF, Baake et al. [33] tested the capability of the widely used $k-\epsilon$ turbulence model to simulate the melt flow in the ICF. The authors reported that this turbulence model was able to predict the time-averaged flow field well. However, the long-frequency pulsations of velocity, occurring between the two main eddies, could not be estimated well using this model. A Reynolds stress turbulence model was adopted in Schwarze et al. [34] for simulating the melt flow inside an ICF. Those authors reported that this model was able to predict the large flow structures with low frequency. However, it was mentioned in many literature that the unsteady Reynolds-averaged Navier-Stokes (URANS) equation could not describe the heat and mass transfers in the ICF [35–37]. Therefore, it was advised to perform

large eddy simulations (LES) in order to enhance describing such processes. Moreover, LES was a good choice to describe the distribution of the temperature in the ICF [38]. In addition, LES showed a good capability to capture the low-frequency oscillations of the axial velocity [39]. The field of the turbulent kinetic energy resulted from LES simulations was shown in Ščepanskis [40]. Here, it was reported that the maximal turbulent kinetic energy was located between the main toroidal vortices. This aspect was validated by using experimental data from Kirpo [31]. According to them, the field of the turbulent kinetic energy and the velocity field depended on crucible filling level. If the melt was placed symmetrical in the magnetic field, the upper and lower toroidal vortices were symmetrical. However, some differences could still be found due to the differences in boundary conditions. The lower vortex was limited by the crucible wall, while the upper vortex was limited by the free surface of the melt.

In most numerical studies, the free surface of the melt has been treated as a slip wall due to difficulties in coupling the magnetic field solver with CFD-solvers. The reason for that is the different magnetic and electrical properties between the melt and the surrounding gas. However, some publications considered the behavior of the free surface under the effect of an alternating magnetic field. For example, Spitans et al. [41] coupled ANSYS Classic and ANSYS CFX in order to capture the free surface. In this work, the Lorentz force was calculated in the ANSYS Classic and then exported to calculate the flow field and the new position of the free surface by volume of fluid (VOF), which was exported back to ANSYS Classic. If the profile of the free surface changed, a new mesh had to be generated. The disadvantage of such simulations is the high computational time. Buliński et al. [42] coupled ANSYS Fluent for fluid flow and EMAG software for the magnetic field. Here, the energy equation was additionally solved in order to describe the temperature field, which was calculated after the flow and the free surface reached steady state. In this publication, the thermal field obtained from the simulation was validated using infrared camera and immersing thermocouples. The comparison of numerical and experimental results showed good agreement in terms of the free surface shape and the temperature field.

Several investigations have been undertaken with the aim of studying the transport of conductive and non-conductive particles. The Euler-Lagrange approach was one of the most adopted approaches to consider the transport of particles in the melt. Kirpo et al. [43] investigated the transport of non-conductive particles in an ICF. They reported

that the particles accumulated close to crucible side wall between the main large-scale vortices. Ščepanskis et al. [44] performed numerical simulations to determine the concentration of particles, which were initialized from the top surface. Moreover, the authors proposed a technique to detect the concentration of particles by taking samples from the particle-laden Wood's metal. The forces, acting on non-conductive particles in an ICF, were investigated by Ščepanskis et al. [45] by means of LES simulations and Euler-Lagrange approach. Those authors claimed that the drag, lift, buoyancy and the electromagnetic pressure forces have to be applied to consider the particle transport in the ICF. However, the influence of such forces on the particles motion depends considerably on the density ratio between particles and liquid. The effect of turbulence modeling on the particles behavior was shown by Barati et al. [46]. Those authors highlighted the high performance of LES for tracking the particles compared to URANS. However, the authors did not adopt any specific modeling of turbulence influence on the particles.

Several experimental and numerical investigations have been undertaken to predict the velocity field and the turbulent properties of the flow in mechanically stirred vessels. In such stirred vessels, similar recirculating turbulent flow to that in the ICF can be observed. Here, the particle image velocimetry (PIV) was one of the often-used measurement techniques. PIV showed high performance in predicting the flow structures and turbulent properties [47–49]. The 3D particle tracking velocimetry (PTV) was also used to measure the flow in a stirred vessel and compared with the PIV technique in Alberini et al. [50]. These authors reported that the PTV technique was able to predict the mean flow field well. On the contrary, it could not estimate the turbulent properties. The PIV technique was used to investigate the considerable effect of the impeller type and submergence on the mixing and the dispersion of the particles [51, 52]. In other studies, numerical investigations were conducted for predicting the complex turbulent flow in the stirred vessels. Therefore, the Reynolds-averaged Navier-Stokes (RANS) simulation was adopted. Compared with experimental data, RANS simulation could estimate the mean flow reasonably [53–55]. However, the computational grid has to be fine for detecting the turbulent properties precisely, which are needed to describe mixing and particle transport. The LES is another powerful tool that has been often adopted to simulate the vortical flow in the stirred vessel and to predict the turbulent kinetic energy as well as the dissipation rate [56,

57]. However, a finer grid was needed compared to RANS in order to resolve 80% of the turbulent kinetic energy.

2.3 Metal Melt Filtration

2.3.1 Main Mechanisms

As explained previously, non-metallic inclusions have to be removed from the steel to improve its quality and properties. Ceramic foam filters are the simplest way to remove non-metallic inclusions in the melt. Such kind of filters were firstly introduced in 1974 for filtering aluminum melts [58]. The filtration of a single-part mold casting started for alumina melt in 1977 and for cast iron in 1983 [3]. Such ceramic foam filters are produced by the replica method [59, 60], in which a highly porous template (polyurethane sponge) is soaked into a ceramic slurry until all pores are filled. Afterwards, the excess slurry is removed to obtain a ceramic coating over the struts of the original template, which is then dried and heat treated in a furnace. The main advantage of the replica method is the capability of producing a large volume of filters with acceptable properties at relatively low cost.

The porosity of the CFFs is determined by the number of pores per inch (ppi), which is chosen depending on the alloy and the metal liquidity [61–63]. The opened ceramic foam filter delivers higher specific area and higher hydraulic resistance compared to multi-holes filter [64]. The filter material has to withstand the chemical, mechanical and thermal stresses, which could potentially lead to a filter destruction. The filter stressing originates mainly from the thermal shock caused by a sudden temperature increase, as the melt contacts the filter [65]. Further sources for the filter stressing are e.g. filter erosion owing to hydraulic forces and chemical corrosion due to the action of slag.

In the filtration application, three mechanisms dominate the filtration process, as can be seen in Figure 2.5 [3, 67, 68]. These mechanisms can take place separately or combined. Surface filtration (sieving) occurs, as long as the filter medium is clean. Here, the particles, that are larger than the pores, are retained on the surface, whereas the small particles pass the filter pores. If the first layer of solid particles (cake) is

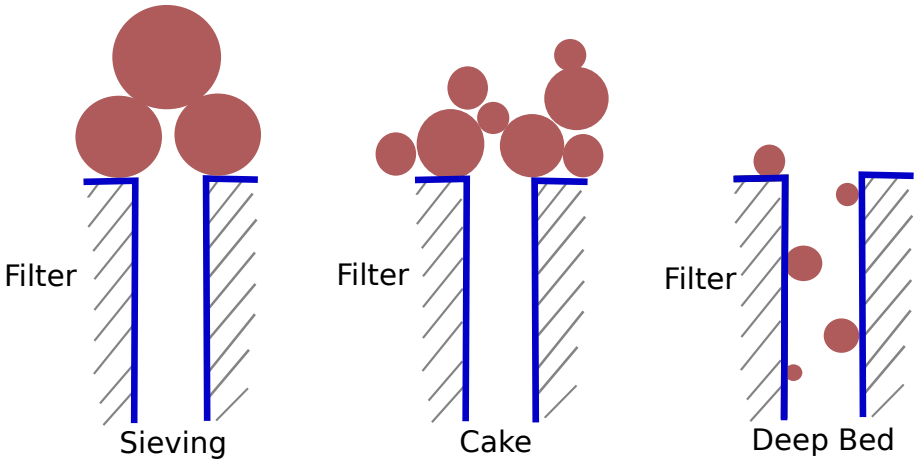

Figure 2.5: Schematic representation of three modes of filtration: sieving, cake and deep bed filtration [66].

formed on the filter surface, the so-called cake filtration takes place. The particles will be separated on the surface of the filter medium and increase the thickness of the cake. In this type of filtration, the cake has the real filtering effect. The deep bed filtration is the dominant filtration mechanism, where the particles, that are smaller than the pores, are retained in deep filter layers. The adhesion of the wall has to be great enough to attract the particles and keep them at filter wall. The interfacial energy between inclusions, filter and metal determines the adhesion strength in this case.

The flow condition (laminar or turbulent), the pore size, the dimension and the shape of the filter as well as the density of the non-metallic inclusions play a significant role in transporting the inclusions from the bulk flow to the filter struts [69]. There are three transport mechanisms, which are relevant for particles in bed filtration. If the inclusions are attached to the ceramic filter, they will undergo solid state sintering with the filter medium and will be permanently deposited at the filter surface [69, 70]. The collision between the non-metallic inclusions and filter wall is determined by several factors, e.g. interception, wetting properties, gravity, inertial forces, Brownian movement and hydrodynamic effects. The interception and gravitation were found to be the dominant mechanisms for the collision [71, 72]. The contribution of gravitation and inertia effects depends on the melt flow rate, whereas the interception correlates more to particle size and collector radius. The effect of gravitation is remarkable only

at low velocity [73]. On the contrary, the effect of inertia increases with increasing flow velocity. Moreover, the wetting of the fluid has a considerable influence on the filtration efficiency and the adhesion energy. Poor wetting between the particle and the fluid induces higher adhesion energy that improves the filtration efficiency of the filter. The poor wettability of the ceramic foam filter leads to formation of nanobubbles on its surface, which increases the adhesion forces and works as capillary bridges adhering the particles to the walls [74].

2.3.2 Reactive Cleaning and Active Filtration

Two approaches of the liquid metal filtration are investigated within CRC 920, active filtration [75] and reactive cleaning [76]. In case of active filtration, the coating of the filter has similar chemistry as the endogenous and exogenous inclusions. Here, the particles can be removed from the melt, if they reach the filter surface. In case of reactive cleaning, the reactive coating of filters reacts with the dissolved gas and can be dissolved in the melt. It is assumed that the reaction leads to formation of carbon monoxide (CO) bubbles, which improves inclusion removal by flotation [20]. Moreover, CO bubbles can form on the inclusions due to this reaction and increase the rising velocity of the inclusions [77]. The reactive effect dominants the filtration process at the beginning till the carbon concentration in the filter is very low. Moreover, it is possible that carbon can not be dissolved from the filter well because of the formed in-situ layers [78]. Afterwards, the filter acts mostly active. However, this assumption can not be proven experimentally because it is not possible to perform measurements in steel melt.

In the frame of CRC 920, it was found that reactive cleaning is more significant to remove non-metallic inclusions compared to active filtration [20]. Oxygen reacts with carbon to form CO bubbles [79]. As mentioned by Storti et al. [20], the CO gas bubbles leave the filter and collect the inclusions and bring them to the free surface of the melt, which promotes inclusion removal. In this paper, the filtration efficiency was measured to be 95%. In a PhD thesis from RWTH Aachen done by Rzehak [80], the formation of CO bubbles at the metal oxides due to the reaction between oxygen and carbon in the melt was investigated. The CO bubbles stay stable on the rough surfaces

of alumina inclusions due to non-wetting properties. In a theoretical investigation by Cournil et al. [81], the spontaneous nucleation of gas cavities in the concave pores of the alumina inclusion surface in case of small particles (5 µm) was studied under thermodynamics conditions for steel melts (see Figure 2.6). The formation of such gas cavities is assumed to promote the agglomeration of inclusions in the steel melt.

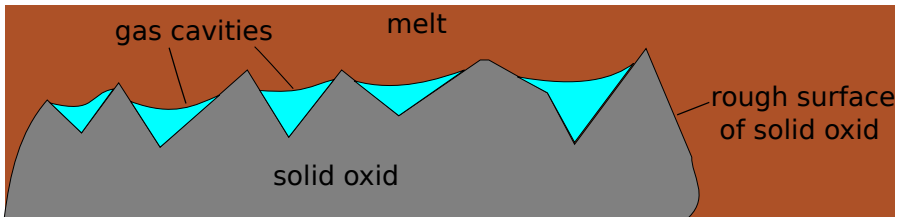

Figure 2.6: Schematic representation of the rough surface of an inclusion and formation of gas cavities.

The heterogeneous nucleation of bubbles at a hydrophobic rough solid wall, similar to the surface of inclusions, was investigated experimentally by Yang et al. [82]. Lohse et al. [83] reported recent findings about nanobubbles at non-wetting surfaces, claiming that multiple nanobubbles can be generated on a hydrophobic particle, which can grow to form microbubbles. The formation of mircobubbles increases the buoyancy force acting on the aggregate (particle and bubble). Thus, the particle with the attached microbubble float up fast to the free surface and are captured by the free surface. In addition, the formation of such nanobubbles was assumed to contribute to the particle-particle and particle-microbubble interaction, which enhances the flotation of particles to the free surface.

Due to difficulties for performing experiments in steel melt, many researchers have developed different experimental water models and numerical simulations in order to investigate the melt flow and inclusions dynamics inside a foam filter without considering the reaction taking place between the filter and melt (active filtration). These investigations were performed by employing different numerical and experimental approaches.

Based on numerical simulations and water modeling, the effect of foam filter structure on inclusion deposition was investigated by Dávila-Maldonado et al. [84]. In this paper, the authors verified the capability of the $k - \epsilon$ turbulence model to predict the velocity profile behind the filter in a casting channel, compared to PIV measurement.

Moreover, the authors reported that the casting velocity and inclusion density do not have major influence on the efficiency of foam filter. On the contrary, the inclusion size is the decisive factor for the deposition probability. Using numerical simulation and experiment, the effective parameters of a ceramic foam filter were determined by Kennedy et al. [85]. A water model experiment was developed by Hwang et al. [86] to mimic the gating system in casting process. In a direct observation of liquid metal flow through ceramic filter done by Hashemi et al. [87], it was found that the ceramic foam filter had a critical role in decreasing the melt velocity (about 50%) and turbulence of the liquid melt. The ceramic foam filter used in this model was responsible to convert the flow pattern of water in a favorable direction. The filter reduced the water velocity and stabilized the stream of the water. Damoah et al. [88] adopted a two-equation turbulence model coupled with Lagrange tracking to simulate the flow of aluminum melt in the channels of 30 ppi filter and to describe the inclusion transport in the filter. This study showed that the inclusions with a larger size were entrapped at the upper part of the foam filter. The 3D computed tomography (CT) scanning was utilized by Werzner et al. [89] to generate the geometry of ceramic foam filters, which was used to simulate the flow inside the filters and to determine the filtration coefficient for different filter structures and porosities for aluminum filtration. In order to investigate aluminum depth filtration, the Lattice Boltzmann method (LBM) was adopted to solve the flow of liquid aluminum in a foam filter and the finite volume method (FVM) was employed to predict the heat transfer in the filter [90]. It was found that the buoyancy force affects the flow in the filter considerably. However, the filtration efficiency was unaffected by buoyancy and temperature-dependent viscosity.

In order to investigate the transient effect during aluminum filtration, the macroscopic mass-balance equations were solved by Tian et al. [91], reporting that the filtration efficiency could increase with the filtration time and inclusions concentration. A 2D Lattice Boltzmann filtration model was adopted by Laé et al. [92] to determine the efficiency of a ceramic foam filter for aluminum filtration. Bao et al. [72] developed an analytical model to describe inclusion removal in commercial ceramic foam filters. Here, the Forchheimer's equation was adopted to calculate the velocity within the filter. In this work, it was shown that the efficiency is correlated considerably with the inclusion size and wettability of the filter.

2.4 Summary

This chapter presents relevant publications related to turbulent flow in an ICF, filtration in a casting form model and the filtration mechanisms inside the filter without considering the instantaneous surrounding flow conditions. However, these publications did not deal with the filtration process in an ICF. Furthermore, they did not consider the formation of CO bubbles in case of reactive cleaning and their contribution to inclusion removal, which has a considerable effect on cleaning efficiency and melt cleanliness. Moreover, the literature did not consider the effect of turbulence modeling on the prediction of the melt flow and inclusion movement. Therefore, the present PhD thesis wants to answer the previous open issues by performing numerical simulations in the ICF and focuses on the following issues:

- Formation of CO bubbles and consideration of their contribution to melt cleanliness in case of reactive cleaning
- Combination between reactive cleaning and active filtration of the steel melt
- Effect of turbulence modeling on predicting melt flow and inclusion transport
- Effect of filter structure on the flow in the ICF
- Water model to mimic the melt flow in the ICF

3 Numerical Model

3.1 CFD library OpenFOAM

All numerical models discussed in the thesis are implemented with the help of open source computational fluid dynamics library OpenFOAM [93]. OpenFOAM uses the finite volume approach [94] to solve the partial differential equations assigned to a 2D or 3D mesh of polyhedral cells. The library contains many solvers for different applications, e.g. incompressible and compressible flows, multiphase flow, magnetohydrodynamics, heat transfer and combustion. However, there is no available solver to consider multiphase flow under the effect of an alternating magnetic field. Furthermore, there is no available solver to consider active filtration of inclusions and the formation of CO bubbles during reactive cleaning process. Therefore, it is required to extend a solver in OpenFOAM in order to account for the previous effects.

`pimpleFoam` is an incompressible solver, based on the PIMPLE algorithm for the pressure-velocity coupling [95]. However, this solver does not take into account the effect of an oscillating magnetic field in case of ICF. Therefore, the solver is modified in order to account for the Lorentz force, which drives the melt in the ICF. In order to track the non-metallic inclusions in the melt, the modified `pimpleFoam` solver is coupled with the library of Lagrangian particle tracking (LPT) in OpenFOAM. Moreover, the electromagnetic pressure force, acting on the non-metallic inclusions in the melt, is implemented in LPT. Additionally, new models are included in LPT to consider the filtration of inclusions and their transport in the ceramic filter. In addition, the model is extended to consider the formation of CO bubbles on the rough surface of inclusions. Moreover, the formation of CO bubbles on filter surface is taken

into account in this model. In the next sections, the development of the numerical models and the adopted equations are discussed in detail.

3.2 Electromagnetic Field

The alternating magnetic field in the ICF is controlled due to its harmonic nature by the so-called skin effect. This effect implies that the time harmonic magnetic field and the induced eddy currents are concentrated close to walls in the magnetic skin with a thickness δ_m, defined in terms of the angular frequency ω of the magnetic field, the electrical conductivity of the steel melt σ_f and the magnetic permeability μ_0 as follows:

$$\delta_m = \sqrt{\frac{2}{\sigma_\mathrm{f}\,\mu_0\,\omega}}. \tag{3.1}$$

Maxwell's equation system of electromagnetism is typically adopted in order to describe the electromagnetic problems and to determine the Lorentz force $\boldsymbol{f}_\mathrm{lor}$ [96]. These equations can be simplified for magnetohydrodynamic engineering applications. Maxwell's equations are reduced by assuming that the displacement currents can be disregarded compared with the eddy current density $\boldsymbol{j}$:

$$\nabla \cdot \boldsymbol{E} = 0 \qquad \text{Charge conservation,} \tag{3.2}$$

$$\nabla \cdot \boldsymbol{B} = 0 \qquad \text{Solenoidal nature of } \boldsymbol{B}, \tag{3.3}$$

$$\nabla \times \boldsymbol{B} = \mu_0\,\boldsymbol{j} \qquad \text{Ampere's law,} \tag{3.4}$$

$$\nabla \times \boldsymbol{E} = -\frac{\partial \boldsymbol{B}}{\partial t} \qquad \text{Faraday's law.} \tag{3.5}$$

In these equations, $\boldsymbol{B}$ and $\boldsymbol{E}$ represent the magnetic induction and the intensity of the electrical field, respectively. In addition to Maxwell's equations, Ohm's law is applied:

$$\boldsymbol{j} = \sigma_\mathrm{f}\,\left(\boldsymbol{E} + \boldsymbol{u} \times \boldsymbol{B}\right), \tag{3.6}$$

where $\boldsymbol{u}$ denotes the melt velocity. The effect of the conducting fluid on the magnetic field can be neglected due to the fact that the magnetic Reynolds number R_m defined as:

$$\mathrm{R_m} = u_{\mathrm{ch}}\, \sigma_{\mathrm{f}}\, \mu_0\; L_{\mathrm{ch}}, \tag{3.7}$$

is much smaller than 1 in the ICF investigated here. In addition, the electromotive field $\boldsymbol{u} \times \boldsymbol{B}$ is negligible compared to the induced field $\boldsymbol{E}$ because $\mathrm{R_m} << \omega\, \sigma_{\mathrm{f}}\, \mu_0\, L_{\mathrm{ch}}^2$ [97]. Here, it is taken into account that the characteristic velocity u_{ch} is equal to the magnitude of maximal velocity in the ICF and the characteristic length L_{ch} to the radius of crucible. As a results, Ohm's law is simplified to:

$$\boldsymbol{j} = \sigma_{\mathrm{f}}\, \boldsymbol{E}. \tag{3.8}$$

Induction equation of $\boldsymbol{B}$ can be derived by taking the curl from the Ohm's law (Equation (3.8)) and combining it with Maxwell's equations:

$$\frac{\partial \boldsymbol{B}}{\partial t} = \frac{1}{\mu_0\, \sigma_{\mathrm{f}}}\, \nabla^2 \boldsymbol{B}. \tag{3.9}$$

The Lorentz force acting on the melt is determined using the following equation:

$$\boldsymbol{f}_{\mathrm{lor}} = \boldsymbol{j} \times \boldsymbol{B}. \tag{3.10}$$

$\boldsymbol{f}_{\mathrm{lor}}$ is decomposed into a mean and an oscillating part. Since the frequency of the time harmonic magnetic field f exceeds $50 - 1000$ Hz, the melt flow is not able to follow the oscillating part because of inertia [97]. This aspect has been often verified by means of experiment and simulation [98, 99]. Therefore, the oscillation part of $\boldsymbol{f}_{\mathrm{lor}}$ is disregarded in the investigated ICF.

The previous mentioned equations are solved in the MaxFEM software in order to determine the mean field of $\boldsymbol{f}_{\mathrm{lor}}$ [100, 101]. For this purpose, a 2D axial symmetrical model of the ICF is created. In the model, the presence of the walls of the crucible is neglected because they are made of non-conductive materials, which means that they do not affect the magnetic field lines. The Dirichlet boundary condition with a magnetic vector potential $\boldsymbol{A} = 0$ is applied on the outer boundary of the model.

The potential drop in the melt is set to $\Delta\varphi = 0$. Then, the distribution of $\boldsymbol{f}_{\mathrm{lor}}$ is interpolated on the full 3D grid for CFD simulations in OpenFOAM by using the "KDTree algorithm for nearest neighbor lookup" [102] in order to simulate the flow in the ICF (see next section). In the present PhD thesis, the heating of melt due to the Joule dissipation is not considered.

3.3 Flow Field

The flow in the crucible is described in Eulerian framework and is assumed to be incompressible, isothermal and turbulent. In the present work, the flow is simulated by performing three different approaches, URANS, RANS/LES and LES. Therefore, the motion of the Newtonian melt in the crucible is described by the unsteady Reynolds-averaged Navier-Stokes or the spatial-filtered Navier-Stokes equations for mass and momentum conservation depending on the used approach:

$$\nabla \cdot \overline{\boldsymbol{u}} = 0 \tag{3.11}$$

$$\frac{\partial \overline{\boldsymbol{u}}}{\partial t} + \nabla \cdot (\overline{\boldsymbol{u}}\,\overline{\boldsymbol{u}}) = -\frac{1}{\rho_{\mathrm{f}}} \nabla \overline{p} + \nabla \cdot (\nu_{\mathrm{f}} \nabla \overline{\boldsymbol{u}}) + \nabla \cdot \underline{\boldsymbol{\tau}}^{\mathrm{mod}} + \overline{\boldsymbol{f}}_{\mathrm{lor}} + \boldsymbol{S}_{\mathrm{filter}}. \tag{3.12}$$

$\overline{\boldsymbol{u}}$ and $\overline{p}$ are the Reynolds-averaged or spatial-filtered velocity and pressure, respectively. ρ_{f} and ν_{f} represent the density and kinematic viscosity of the melt, respectively. The mean field of Lorentz force $\overline{\boldsymbol{f}}_{\mathrm{lor}}$, arising because of the magnetic field, is included in Equation (3.12) to drive the molten metal in the crucible of the ICF. As mentioned previously, the oscillating field of Lorentz force is neglected. $\boldsymbol{S}_{\mathrm{filter}}$ is an additional source term that is responsible for the pressure drop in the ceramic filter. This term will be explained later in more detail (see section 3.3.2). $\underline{\boldsymbol{\tau}}^{\mathrm{mod}}$ is the Reynolds stress or the subgrid stress tensor that must be approximated by employing the proper turbulence model.

3.3.1 Turbulence Modeling

In the PhD thesis, different turbulence models are employed to approximate the stress tensor $\underline{\boldsymbol{\tau}}^{\mathrm{mod}}$. The main reason for choosing different turbulence models is to investigate

the effect of turbulence modeling on the melt flow in the ICF and on inclusion transport. The following paragraphs discuss the employed turbulence modeling.

SST $k-\omega$ Model

In the URANS simulation, the shear-stress transport (SST) $k-\omega$ turbulence model, that is mainly developed by Menter [103], is employed in order to approximate the Reynolds stress tensor $\underline{\boldsymbol{\tau}}^{\mathrm{mod}}$. The main idea of the SST $k-\omega$ turbulence model is using blending functions to combine the standard $k-\epsilon$ turbulence model in the free stream region and the $k-\omega$ turbulence modeling in the near wall region [104, 105]. The combination between the two models offers a better possibility to predict the flow separation under adverse pressure gradients. Moreover, it provides better robustness and computational cheapness. The implementation of the SST $k-\omega$ turbulence model in OpenFOAM is presented by Menter et al. [106]. The transport equations for the turbulent kinetic energy k and turbulent specific dissipation rate ω are expressed as follows:

$$\frac{\partial k}{\partial t} + \nabla \cdot (\overline{\boldsymbol{u}}\, k) = \hat{P}_k - \beta^* \, k\, \omega + \nabla \cdot \left[(\nu_{\mathrm{f}} + \sigma_k \nu_t) \, \nabla \, k \right], \tag{3.13}$$

$$\frac{\partial \omega}{\partial t} + \nabla \cdot (\overline{\boldsymbol{u}}\, \boldsymbol{\omega}) = \frac{\gamma}{\nu_t} P_\omega - \beta \, \omega^2 + \nabla \cdot \left[(\nu_{\mathrm{f}} + \sigma_w \nu_t) \, \nabla \, \omega \right] + \frac{2}{\omega} \, (1 - F_1) \, \sigma_{w2} \, \nabla k \, \nabla \omega. \tag{3.14}$$

The turbulent viscosity ν_t is calculated as follows:

$$\nu_t = \frac{a_1 \, k}{\max \left(a_1 \, \omega, S \, b_1 \, F_2 \, F_3 \right)}. \tag{3.15}$$

S is the magnitude of the strain rate. F_1 and F_2 are the blending functions, which are equal to 0 in the free stream region and become 1 close to the wall. F_3 is a function that is developed by Hellsten [107] in order to prevent the limitation in ν_{t} in case of rough wall flows. This function is disabled in case of smooth walls. Moreover, a production limiter is utilized in order to avoid the production of turbulence in

stagnation region:

$$\hat{P}_\mathrm{k} = \min\left(P_\mathrm{k}, c_1\,\beta^*\,k\,\omega\right), \tag{3.16}$$

$$P_\omega = \min\left(P_\mathrm{k}, \frac{c_1}{a_1}\beta^*\,\omega\;\cdot\;\max\left[a_1\,\omega, b_1\,F_2\,F_3\,S\right]\right), \tag{3.17}$$

with the turbulent production:

$$P_k = 2\,\nu_\mathrm{t}\left[\frac{1}{2}\left(\nabla\overline{\boldsymbol{u}} + \nabla\overline{\boldsymbol{u}}^T\right)\right]. \tag{3.18}$$

The coefficients of the SST model are taken from Menter et al. [108]:

$$\begin{aligned} a_1 &= 0.31, & b_1 &= 10, & \gamma_1 &= 5/9, & \gamma_2 &= 0.44,\\ \sigma_\mathrm{k1} &= 0.85, & \sigma_\mathrm{k2} &= 1, & \sigma_{\omega1} &= 0.4, & \sigma_{\omega2} &= 0.85,\\ \beta^* &= 0.09, & \beta_1 &= 0.075, & \beta_2 &= 0.0828, & c_1 &= 10,\\ CD_{\mathrm{k}\omega,\mathrm{min}} &= 10^{-10}. \end{aligned}$$

SST $k-\omega$ SAS Model

Hybrid RANS/LES approaches are developed in order to obtain the typical LES-behavior with lower computational costs. One kind of these approaches is the scale-adaptive simulation (SAS) [109, 110]. The basic idea of this approach is to include an additional source term P_SAS in the ω-equation of the SST $k-\omega$ turbulence model [103, 106]. This allows the unsteadiness of the flow to be developed in the unsteady regions, which is normally damped out by the turbulent viscosity in case of the SST $k-\omega$ model. P_SAS is defined as follows [111]:

$$P_\mathrm{SAS} = F_\mathrm{SAS}\max\left(T_1 - T_2, 0\right), \tag{3.19}$$

$$T_1 = \xi_2\,\kappa\,S\left(\frac{L_\mathrm{T}}{L_\mathrm{vK}}\right), \tag{3.20}$$

$$T_2 = C\,\frac{k}{\sigma_\phi}\max\left(\frac{|\nabla\omega|^2}{\omega^2}, \frac{|\nabla k|^2}{k^2}\right), \tag{3.21}$$

with $F_\mathrm{SAS} = 1.25$, $\zeta_2 = 3.52$, $\kappa = 0.41$, $C = 2$ and $\sigma_\phi = 0.66$. The turbulent length scale L_T and the von-Kármán length L_vK are calculated by employing the following

expressions:

$$L_{\mathrm{T}} = \frac{\sqrt{k}}{C_{\mu}^{0.25}\,\omega}, \tag{3.22}$$

$$L_{\mathrm{vK}} = \max\left(\kappa\frac{\sqrt{S}}{|\Delta\overline{\boldsymbol{u}}|}, C_{\mathrm{s}}\sqrt{\frac{\kappa\,\zeta_2}{\beta/\beta^* - \alpha}}\,\Delta\right), \tag{3.23}$$

with $C_{\mu} = \beta^* = 0.09$ and $C_{\mathrm{s}} = 0.11$.

The occurrence of unsteadiness in the flow is examined by the ratio between the strain rate and velocity Laplacian in L_{vK}. If the ratio becomes low, the description of L_{vK} is then proportional to the grid cell size Δ. Since the grid cell size is sufficient small, L_{vK} is small compared to L_{T}. This may lead to a higher T_1 compared to T_2. Thus, P_{SAS} is positive and acts as an additional production of ω. As a consequence, ω increases in the flow field, which decreases the turbulent viscosity and the unsteadiness of the flow can be developed to have a LES like-behavior.

WALE Subgrid-scale Model

The wall-adapting local eddy-viscosity (WALE) is one of the subgrid turbulence model that is used in LES. In WALE, the large scales are resolved, while the scales, which are smaller than the grid size, are modeled adopting this subgrid-scale turbulence model. In the WALE model, the turbulent viscosity is damped close to the wall without using any additional damping function. In this model, the definition of the turbulent viscosity is based on magnitude of the deviatoric symmetric part of the square of the velocity gradient tensor $\underline{\boldsymbol{S}}_{\mathrm{d}}$ and the strain rate tensor $\underline{\boldsymbol{S}}$ [112]. The turbulent viscosity is computed in the model as follows:

$$\nu_t = (C_{\omega}\,\Delta)^2\,\frac{(\underline{\boldsymbol{S}}_{\mathrm{d}}\,\underline{\boldsymbol{S}}_{\mathrm{d}})^{3/2}}{(\underline{\boldsymbol{S}}_{\mathrm{d}}\,\underline{\boldsymbol{S}}_{\mathrm{d}})^{5/4}\,(\underline{\boldsymbol{S}}\,\underline{\boldsymbol{S}})^{5/2}} \tag{3.24}$$

with $C_{\omega} = 0.325$. The WALE turbulence model is known to be suitable to reproduce laminar to turbulent transitional flow [112].

ILES Approach

The Implicit Large Eddy Simulation (ILES) is an approach to model the subgrid scales in case of the LES simulation by adopting a certain spatial numerical discretization scheme of the convection terms in Equation (3.12) [113, 114]. As a consequence, the numerical truncation error acts as a subgrid-scale turbulence model and is used to model the subgrid stress tensor. The advantage of ILES is that no explicit subgrid models are required to model the subgrid stress tensor. This means that the computational effort is less in case of ILES because no additional equations for the turbulence modeling have to be solved in OpenFOAM.

3.3.2 Porous Medium

The ceramic foam filter immersed in the melt is considered as being a homogeneous isotropic porous medium with constant permeability. The additional pressure drop inside the filter is taken into account by including the source term $\boldsymbol{S}_{\text{filter}}$ in Equation (3.12), which is estimated according to the Darcy-Forchheimer's law:

$$\boldsymbol{S}_{\text{filter}} = -\left(\frac{\mu_{\text{f}}}{\kappa_1} + \frac{\rho_{\text{f}}}{\kappa_2}\,|\overline{\boldsymbol{u}}|\right)\,\overline{\boldsymbol{u}}. \tag{3.25}$$

Here, μ_{f} represents the dynamic viscosity of the fluid. κ_1 and κ_2 stand for the permeability and Forchheimer coefficient, respectively. They are obtained from a direct numerical simulation (DNS) of the melt flow inside an open-cell ceramic foam filter, whose geometry is reconstructed from computed tomography (CT) scan images, acquired with a voxel resolution of 34 µm [115]. The detailed flow simulations are performed by subproject B02 (in CRC 920) using an in-house code that is based on the LBM. In the LBM-simulation, the physical domain is discretized adopting a Cartesian grid, which consists of voxels with a resolution of the CT scan data. The voxels are assigned to be either part of the fluid or part of the filter's struts [89, 90, 115]. The properties of the filter can be found in Table 3.1.

Table 3.1: Properties of the ceramic foams with a pore density of 10 ppi and 20 ppi [115].

	10 ppi	20 ppi
Geometric properties		
Porosity [−]	0.80	0.73
Pore density [m^{-3}]	$1.03 \cdot 10^{7}$	$3.48 \cdot 10^{7}$
Pore diameter D_p [m]	$6.05 \cdot 10^{-3}$	$3.81 \cdot 10^{-3}$
Strut diameter [m]	$0.91 \cdot 10^{-3}$	$0.75 \cdot 10^{-3}$
Window diameter [m]	$3.80 \cdot 10^{-3}$	$2.84 \cdot 10^{-3}$
Hydrodynamic resistance		
Permeability κ_1 [m^2]	$1.96 \cdot 10^{-7}$	$7.56 \cdot 10^{-8}$
Forchheimer coefficient κ_2 [m]	$2.78 \cdot 10^{-3}$	$1.59 \cdot 10^{-3}$
Filtration coefficient (see section 3.5)		
C_0 [m^{-1}]	1.35	3.60
C_1 [m^{-1}]	0.558	1.23
C_2 [−]	0.346	0.41

3.4 Inclusion Transport

The transport of the disperse phase (inclusions or bubbles) is described by using the discrete phase model (DPM) [116, 117]. Each inclusion is tracked as an individual point particle in a Lagrangian way by solving its equation of motion, while the melt flow is described as continuum on the fixed computational grid in the Eulerian framework. Furthermore, the inclusions are assumed to be rigid spheres for estimating the forces.

It is assumed that the disperse phase does not affect the flow structure (one-way coupling). This assumption is valid, since the following relation mentioned by Loth [118] is fulfilled:

$$\Pi_L = \frac{\alpha_p \, L_{ch} \, |\rho_p - \rho_f| \, g}{\rho_f \, u_{ch}^2} \ll 1, \tag{3.26}$$

where g and ρ_p represent the gravitational acceleration magnitude and the inclusion density, respectively. This relation indicates the change in the net macroscopic

momentum or turbulence of the continuous phase owing to the presence of the dispersed particles. The characteristic length L_{ch} is equal to the radius of crucible and the characteristic velocity u_{ch} to the magnitude of maximal velocity ($u_{\mathrm{ch}} \approx 0.05\ \mathrm{m\,s^{-1}}$). The void fraction of inclusions α_{p} for the multiphase simulations is approximated to $2 \cdot 10^{-7}$. The previous relation is valid for all simulations performed in the present work. Therefore, the influence of inclusions on the turbulent flow in the crucible can be neglected.

The interaction between the inclusions (four-way coupling) can be neglected in the simulations as well because the following criterion described in Loth [118] is valid for the considered cases:

$$\chi = \frac{N_{\mathrm{t,p}} \pi \Lambda\, d_{\mathrm{p}}^2}{V_{\mathrm{c}} \sqrt{(\gamma^2 + 1)}} \ll 1, \tag{3.27}$$

where $N_{\mathrm{t,p}}$ is the total number of inclusions present in the melt, d_{p} is the diameter of an inclusion, γ denotes ratio of the particle terminal velocity $u_{\mathrm{p,term}}$ to root mean square velocity u_{rms} of the turbulent fluctuations, V_{c} denotes the volume of the utilized crucible. Λ represents the eddy integral length scale and is assumed to be equal to the radius of crucible. For the simulation parameters, χ lies within the range of $0.003 - 0.009$. Other criteria can be found in literature to examine the validity of the previous assumptions, e.g. particle loading of fluid [119]. As mentioned previously, the inclusions are tracked in the Lagrangian approach by solving their equations of motion:

$$m_{\mathrm{p}} \frac{\mathrm{d}\boldsymbol{v}}{\mathrm{d}t} = \boldsymbol{F}_{\mathrm{tot}}. \tag{3.28}$$

Here, m_{p} and $\boldsymbol{v}$ stand for the mass and the velocity of an inclusion, respectively. $\boldsymbol{F}_{\mathrm{tot}}$ is the total forces acting on an inclusion that are addressed in the following paragraphs.

Buoyancy and gravitational force

The buoyancy force $\boldsymbol{F}_\mathrm{B}$ and gravitational force $\boldsymbol{F}_\mathrm{G}$ are estimated in OpenFOAM by means of the following equation:

$$\boldsymbol{F}_\mathrm{B} + \boldsymbol{F}_\mathrm{G} = \frac{(\rho_\mathrm{p} - \rho_\mathrm{f})\,\pi\,d_\mathrm{p}^3}{6}\,\boldsymbol{g}, \tag{3.29}$$

where $\boldsymbol{g}$ represents the vector of the gravitational acceleration.

Drag force

The drag force arises due to the pressure distribution and shear stress around the inclusion. This force can be calculated by:

$$\boldsymbol{F}_\mathrm{D} = \frac{3}{4}\frac{\mu_\mathrm{f}}{\rho_\mathrm{p}\,d_\mathrm{p}^2}\,C_\mathrm{D}\,\mathrm{Re}_\mathrm{p}\,(\boldsymbol{u} - \boldsymbol{v}) \;\text{ with }\; \mathrm{Re}_\mathrm{p} = \frac{\rho_\mathrm{f}\,d_\mathrm{p}\,|\boldsymbol{u} - \boldsymbol{v}|}{\mu_\mathrm{f}}. \tag{3.30}$$

The drag coefficient of a spherical particle C_D depends on the Reynolds number of the particle Re_p [120, 121]. At low Re_p, C_D decreases with increasing Re_p. This is assigned to the Stokes flow regime ($\mathrm{Re}_\mathrm{p} < 1$). With increasing Re_p, the inertial range is reached and the particle has a nearly constant value of C_D. At critical Reynolds number $\mathrm{Re}_\mathrm{p,cr}$, the boundary layer becomes turbulent. As a consequence, a sudden reduction in C_D can be observed. Many studies have been carried out in order to estimate C_D for the total range of Re_p (see references [120, 121]). In the present work, C_D of the spherical inclusions is estimated by means of an empirical relation implemented in OpenFOAM for spherical solid particle, which is expressed as follows [122, 123]:

$$C_\mathrm{D} = \begin{cases} \frac{24}{\mathrm{Re}_\mathrm{p}}\left[1 + \frac{1}{6}\,\mathrm{Re}_\mathrm{p}^{\frac{2}{3}}\right] & ;\mathrm{Re}_\mathrm{p} \leq 1000 \\ 0.424 & ;\mathrm{Re}_\mathrm{p} > 1000. \end{cases} \tag{3.31}$$

Virtual mass force

The virtual mass force $\boldsymbol{F}_\mathrm{VM}$ originates from an accelerated motion of the particle in the flow field. It can be considered as an additional resistance to the accelerated

motion of the particle. $\boldsymbol{F}_{\mathrm{VM}}$ is computed as:

$$\boldsymbol{F}_{\mathrm{VM}} = C_{\mathrm{VM}}\,\rho_{\mathrm{f}}\frac{\pi\,d_{\mathrm{p}}^3}{6}\left(\frac{D\boldsymbol{u}}{\mathrm{D}t} - \frac{\mathrm{d}\boldsymbol{v}}{\mathrm{d}t}\right). \tag{3.32}$$

According to Odar [124] and Crowe et al. [121], C_{VM} of a spherical particle is equal to 0.5.

Saffman lift force

A dynamic lift force $\boldsymbol{F}_{\mathrm{L}}$ acts on a particle in the flow field due to the rotation of the velocity field that can be imposed normally from the shear flow. $\boldsymbol{F}_{\mathrm{L}}$ moves the particle toward the region with higher velocity of the continuous phase, if the relative velocity between fluid and particle $\boldsymbol{u}_{\mathrm{rel}}$ is positive. Otherwise, the particle is pushed to low-velocity region. The lift force $\boldsymbol{F}_{\mathrm{L}}$ is calculated in OpenFOAM using the following equation:

$$\boldsymbol{F}_{\mathrm{L}} = C_{\mathrm{L}}\rho_{\mathrm{f}}\frac{\pi\,d_{\mathrm{p}}^3}{6}\left(\boldsymbol{u}-\boldsymbol{v}\right)\times\left(\nabla\times\boldsymbol{u}\right). \tag{3.33}$$

C_{L} is the lift coefficient that is firstly derived by Saffman [125] and extended by Mei [126]. It is estimated in this work according to its standard implementation in OpenFOAM:

$$C_{\mathrm{Ld}} = \begin{cases} 6.46f & ;\mathrm{Re}_{\mathrm{p}} < 40 \\ 0.339\sqrt{\beta} & ;\mathrm{Re}_{\mathrm{p}} \geq 40 \end{cases} \tag{3.34}$$

The coefficients appearing in Equation (3.34) are calculated as follows:

$$\beta = \frac{1}{2}\frac{\mathrm{Re}_{\omega}}{\mathrm{Re}_{\mathrm{p}}}, \tag{3.35}$$

$$f = (1-\alpha)\,e^{-0.1\,\mathrm{Re}_{\mathrm{p}}} + \alpha, \tag{3.36}$$

$$\alpha = 0.3314\sqrt{\beta}. \tag{3.37}$$

Here, the shear Reynolds number Re_ω is determined by

$$\mathrm{Re}_\omega = \frac{\rho_\mathrm{f} \left|\nabla \times \boldsymbol{u}\right| d_\mathrm{p}^2}{\mu_\mathrm{f}}. \tag{3.38}$$

In order to get the correct non-dimensional form of the lift coefficient C_L, C_Ld is scaled as follows:

$$C_\mathrm{L} = \frac{3}{2\pi\sqrt{\mathrm{Re}_\omega}}\, C_\mathrm{Ld}. \tag{3.39}$$

Then, C_L is included in Equation (3.33) in order to calculate $\boldsymbol{F}_\mathrm{L}$.

Electromagnetic Pressure Force

Since the electrical conductivity of the non-metallic inclusions differs from that of the melt, the inclusions experience an electromagnetic pressure force $\boldsymbol{F}_\mathrm{EM}$. This force arises due to inhomogeneity in a locally homogeneous magnetic field. $\boldsymbol{F}_\mathrm{EM}$ moves the inclusions in the opposite direction of the imposed Lorentz force $\overline{\boldsymbol{f}}_\mathrm{lor}$, in other words, in the direction of the crucible's wall [127, 128]. This can help to remove the inclusions from the melt. An expression to estimate this force can be derived by solving the Laplace equations for current density and simplified in case of steady magnetic field to [129–131]:

$$\boldsymbol{F}_\mathrm{EM} = -\frac{3}{2}\,\frac{\sigma_\mathrm{f} - \sigma_\mathrm{p}}{2\,\sigma_\mathrm{f} + \sigma_\mathrm{p}}\, V_\mathrm{p}\, \overline{\boldsymbol{f}}_\mathrm{lor}. \tag{3.40}$$

Here, σ_p and V_p represent the electrical conductivity and the volume of an inclusion, respectively. The inclusions in the flow field are assumed to be non-conductive. Thus, σ_p is equal to 0; hence, the expression of $\boldsymbol{F}_\mathrm{EM}$ can be simplified to:

$$\boldsymbol{F}_\mathrm{EM} = -\frac{3}{4}\, V_\mathrm{p}\, \overline{\boldsymbol{f}}_\mathrm{lor}. \tag{3.41}$$

$\overline{\boldsymbol{f}}_\mathrm{lor}$ is interpolated during the simulation from the cell, where the inclusion exists.

3.4.1 Dispersion Model

In case of URANS and SAS simulations, the instantaneous velocity of melt flow $\boldsymbol{u}$, which is experienced by the inclusions, has to be modeled to describe the inclusion dispersion in the turbulent flow. For this purpose, the Discrete Random Walk (DRW) dispersion model or „eddy lifetime“ model is applied. Here, the fluctuating velocity components of the melt $\boldsymbol{u}'$ are kept constant over the eddy lifetime. The value of $\boldsymbol{u}'$ obeys a Gaussian probability distribution. It then follows the assumption of isotropic turbulence:

$$\boldsymbol{u}' = \xi \, \boldsymbol{d} \sqrt{\frac{2k}{3}}, \tag{3.42}$$

where ξ is a scalar formed by normally distributed random numbers. $\boldsymbol{d}$ is a random vector added in OpenFOAM to consider the spatial randomness of turbulence.

Finally, $\boldsymbol{u}'$ is added to the instantaneous flow velocity $\overline{\boldsymbol{u}}$ with respect to the Reynolds decomposition:

$$\boldsymbol{u} = \overline{\boldsymbol{u}} + \boldsymbol{u}'. \tag{3.43}$$

Then, $\boldsymbol{u}$ is adopted for calculating $\boldsymbol{F}_{\mathrm{D}}$, $\boldsymbol{F}_{\mathrm{VM}}$ and $\boldsymbol{F}_{\mathrm{L}}$.

In contrast to URANS simulations, the DRW model is not applied in case of LES and ILES simulations because $\boldsymbol{u} \approx \overline{\boldsymbol{u}}$ can be assumed for these simulations.

3.5 Active Filtration of Inclusions

The removal of non-metallic inclusions, which pass the filter, is considered by the law of depth filtration, which provides the probability ψ for an inclusion to be filtered. The following model is developed for the ceramic foam filters, which is being manufactured

in CRC 920, to determine ψ in case of filtration in ceramic foam filters. ψ is defined as a function of the penetration depth Δs and the filtration coefficient λ:

$$\psi = 1 - e^{-\lambda \Delta s}. \tag{3.44}$$

The filtration coefficient λ is determined in the simulation as a function of the local Reynolds number of the melt using the following relation, which has been derived by performing a pore-scale simulation in two ceramic foam filters with a pore density of 10 ppi and 20 ppi in case of $d_\mathrm{p} = 20$ µm [115]:

$$\lambda = \mathrm{f(Re)} = \sqrt[5]{C_0^5 + \left(C_1 \, \mathrm{Re}^{C_2}\right)^5} \quad \text{with Re} = \frac{\rho_\mathrm{f} |\boldsymbol{u}| \, D_\mathrm{p}}{\mu_\mathrm{f}}. \tag{3.45}$$

D_p represents the pore diameter of the ceramic foam filter. The coefficients C_0, C_1 and C_2 for 10 ppi and 20 ppi ceramic filters are listed in Table 3.1. The variation of the filtration coefficient in terms of Re is shown in Figure 3.1. From this figure, it is clear that λ is higher in case of 20 ppi.

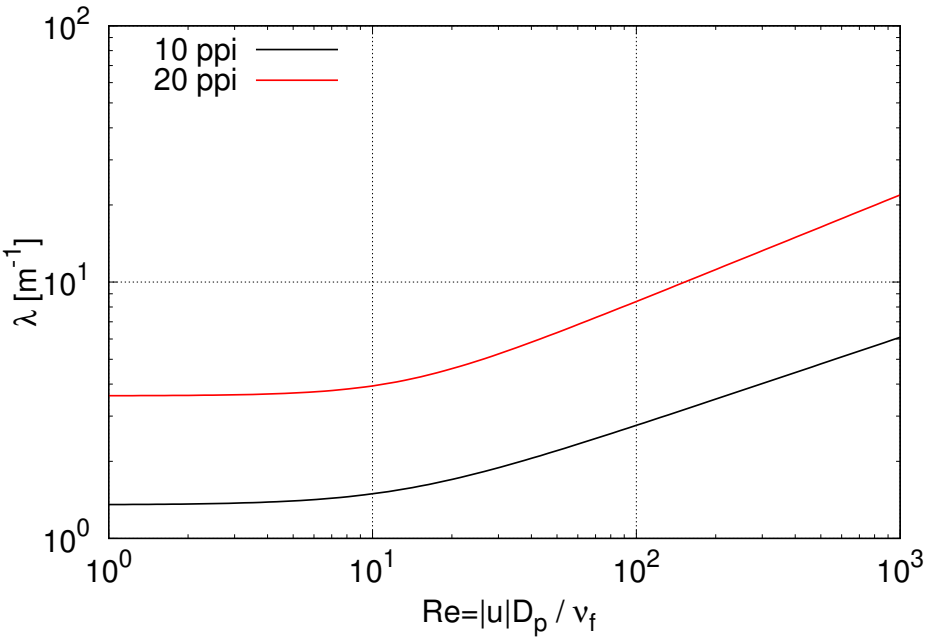

Figure 3.1: Variation of the filtration coefficient λ with the local Reynolds number Re, depending on the melt velocity $\boldsymbol{u}$, pore diameter D_p and kinematic viscosity ν_f, for filters with pore density of 10 ppi and 20 ppi [115].

The filtration probability of the inclusions being in the filter depends considerably on the varying melt velocity inside the filter. For this reason, the filtration probability should be accumulated and an effective filtration probability ψ_{eff} of each inclusion needs to be computed during the simulation. For this purpose, the following expression is used for each inclusion entering the filter [115]:

$$\psi_{\text{eff}}^{\text{n}} = \psi_{\text{eff}}^{\text{o}} + (1 - \psi_{\text{eff}}^{\text{o}})\ \psi^{\text{i}}, \tag{3.46}$$

where the superscripts "n" and "o" stand for the current value and the value calculated at a previous time step in the solution procedure, respectively. Equation (3.44) is employed in order to determine the instantaneous filtration probability ψ^{i}, which is a function of the local Reynolds number of the melt and the step that the inclusion travels in the current time step. ψ_{eff} is compared with a distributed random number $\zeta \in [0, 1]$, when the inclusion leaves the filter. If $\zeta < \psi_{\text{eff}}$, the inclusion is assumed to be filtered and then deleted from the simulation.

3.6 Creation of CO Bubbles on Inclusion Surface

The previous numerical model is extended to consider the creation of CO bubbles on inclusions. The extension of the model has already been published by Asad et al. [77]. The filters, developed in CRC 920, are bonded with carbon, which dissolves in the melt and reacts with oxygen available in the melt. As result of the reaction, a CO Bubble can form on the inclusion. The extended model is not able to account for the reaction between all elements available in the melt to estimate the exact amount of gas that may arise in the melt. The main aim of this model is to approximate the volume of bubbles and to show the effect of bubble creation on the cleanliness of the melt. Please note that the disperse phase includes the inclusion-bubble aggregates and inclusions in this case. To simplify the model, the agglomeration of the inclusion-bubble aggregates and inclusions are neglected in the model due to the fact that the void fraction of these aggregates and inclusions is very low. This means that the contact probability is very low [118, 119].

3.6.1 Transport of Carbon

As mentioned previously, carbon C can be transported from the filter into the melt. The transport of C in the melt flow can be computed using the following transport equation:

$$\frac{\partial\, c}{\partial\, t} + \nabla \cdot (\overline{\boldsymbol{u}}\, c) = \nabla \cdot \left[\left(\frac{\nu_\mathrm{f}}{\mathrm{Sc}} + \frac{\nu_\mathrm{t}}{\mathrm{Sc_t}} \right) \nabla\, c \right] + S_\mathrm{k}. \tag{3.47}$$

Here, the concentration of carbon is represented by c. The turbulent Schmidt number is assumed to be $Sc_\mathrm{t} = 1$ [132]. The Schmidt number $\mathrm{Sc} = \nu_\mathrm{f}/D$ is calculated with the diffusion coefficient of carbon in steel melt $D = 10^{-8}\ \mathrm{m^2\,s^{-1}}$ [133]. S_k accounts for the reduction of the carbon concentration because of the reaction. Due to the fact that ν_t cannot be calculated explicitly in case of the ILES simulation, it is estimated according to the Smagorinsky subgrid model in this case [134]:

$$\nu_\mathrm{t} = 0.094\, V_\mathrm{cell}^{1/3}\, {k_\mathrm{sgs}}^{0.5}, \tag{3.48}$$

where V_cell is the volume of the cell and k_sgs represents the subgrid turbulent kinematic energy.

3.6.2 Reaction Model

The equation system, which is used to determine the bubble size, is represented in Figure 3.2a. The reaction between carbon and oxygen is assumed to be first order. The current amount of substance of carbon n_0 is estimated as a function of c and V_cell. If inclusions are present in the computational cell, a bubble will arise on the inclusion surface due to the reaction. Thus, n_0 decreases to n. This depends on the number of inclusions in the computational cell n_p, surface area of an inclusion A_p, the time step Δt and the reaction rate constant k_r, which is equal to 14.9 $\mathrm{mol\,m^{-2}\,s^{-1}}$ for melt temperature of 1873 K [135]. The increase of bubble size in each cell ΔV_b can be determined as a function of the reduction of n_0, ideal gas constant R, melt temperature T and pressure p. Then, the increase of bubble size for each inclusion is calculated by $\Delta V_\mathrm{b}/n_\mathrm{p}$. Finally, the sink term S_k is evaluated in order to determine the reduction of c in each cell.

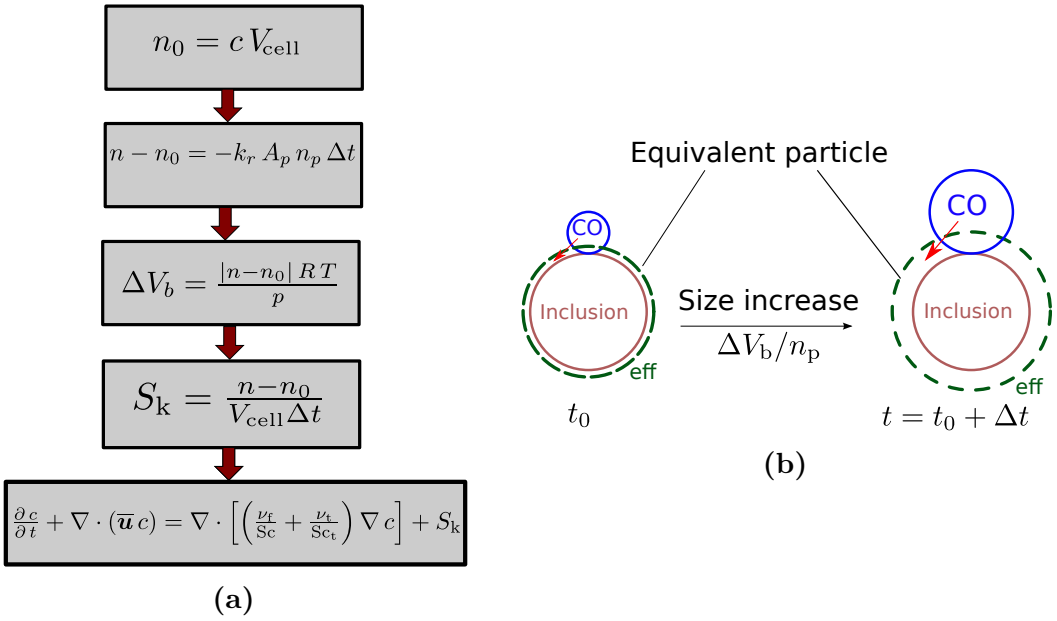

Figure 3.2: a) The equations system implemented in OpenFOAM to account for the reaction between carbon and oxygen and b) the equivalent particle (eff) consisting of an inclusion with a constant diameter and a gas layer. The volume of this gas layer corresponds to the increased volume of the attached CO bubble [77].

3.6.3 Equivalent Particles

The extended model is based on the assumption that the CO bubbles can form directly in the concave pores of an inclusion due to the reaction between carbon and oxygen. Moreover, the arising CO bubble is assumed to create a gas layer surrounding the inclusion, which can grow. Then, the inclusion with the attached gas layer floats fast to the free surface of the melt. The aggregate of inclusion and arising gas layer is represented in this extended model by an equivalent particle of spherical shape (see Figure 3.2b). The surface of the equivalent particle is indicated by the dashed green line in Figure 3.2b. The equivalent particle has an effective mass m_{eff}, effective volume

V_{eff}, effective density ρ_{eff} and effective diameter d_{eff}:

$$V_{\text{b}} = V_{\text{b},0} + \Delta V_{\text{b}}/n_{\text{p}}, \tag{3.49}$$

$$V_{\text{eff}} = V_{\text{b}} + V_{\text{p}}, \tag{3.50}$$

$$m_{\text{eff}} = \rho_{\text{b}}\, V_{\text{b}} + \rho_{\text{p}}\, V_{\text{p}}, \tag{3.51}$$

$$\rho_{\text{eff}} = \frac{m_{\text{eff}}}{V_{\text{eff}}}, \tag{3.52}$$

$$d_{\text{eff}} = \left(\frac{6}{\pi}\, V_{\text{eff}}\right)^{\frac{1}{3}}. \tag{3.53}$$

In the model, the size of inclusion does not change during the simulation. The increase of the bubble size is taken into account by adding $\Delta V_{\text{b}}/n_{\text{p}}$ to the current bubble volume $V_{\text{b},0}$. The density of bubble ρ_{b} is estimated during the simulation according to the ideal gas law. The inclusion density ρ_{p} is assumed to be constant. The effective parameters (e.g. d_{eff}, m_{eff} and ρ_{eff}) are then included in the equations of motion (Equation (3.28)) in order to consider the forces acting on the equivalent particles and to predict their transport in the melt. In this case, the relation (3.26) is not valid because the bubbles diameter increases to reach higher values ($\approx 700\,\mu\text{m}$). This means that the interaction between the disperse phase and the continuous phase has to be considered. Therefore, a source term $\boldsymbol{\phi}$ has to be included to Equation (3.12). This term is defined as follows:

$$\boldsymbol{\phi} = -\frac{1}{V_{\text{cell}}} \sum \boldsymbol{F}_{\text{tot}}. \tag{3.54}$$

Here, a loop over all inclusions present in each computational cell has to be done and the total force acting on an inclusion $\boldsymbol{F}_{\text{tot}}$ has to be calculated.

3.7 Creation of CO Bubbles on Filter Surface

The numerical model is further extended to consider pure bubble formation without inclusion on the filter surface. The extension of the model has already been published by Asad et al. [136]. It is difficult to realize the separation of the bubble from the filter surface in the simulation. Therefore, bubbles with an initial diameter are initialized at

certain points at the filter walls. Moreover, the bubble growth owing to the reaction at the filter surface can not be captured correctly because the filter is considered using the Darcy Forchheimer's law. This means that the different mechanisms of this reaction, e.g. formation of in-situ layers [78], effect of the surface tension on the rough surface of the filter [137], etc., cannot be reproduced in the simulation. Therefore, it is attempted to cover the possible processes to show the effect of bubble formation at filter surface on inclusion removal. For this purpose, the numerical model assumes that the bubble volume can increase till the bubble reaches the prescribed bubble diameter. The increase of the bubble volume is assumed to be either linear or exponential in order to cover a large range. Furthermore, the bubbles are injected with a certain diameter, which remains constant during the simulation. In these cases, two-way coupling between the bubbles and the melt is taken into account.

3.7.1 Increase of Bubble Size

Linear Increase

The volume of bubble V_b increases in this case linearly as a function of time t until the bubble reaches the maximal diameter $d_\mathrm{b,max}$ at the prescribed end time τ. The volume of the bubble increases according to the following equation:

$$V_\mathrm{b} = V_\mathrm{b,0} + c_\mathrm{b1}\, t. \tag{3.55}$$

Here, $V_\mathrm{b,0}$ is the initial volume of the bubble. The constant c_b1 is calculated using the following equation in order to ensure that the bubble will reach the maximal volume $V_\mathrm{b,max}$ and the corresponding maximal diameter:

$$c_\mathrm{b1} = \frac{V_\mathrm{b,max} - V_\mathrm{b,0}}{\tau}. \tag{3.56}$$

Exponential Increase

The volume of bubble V_b rises in this case exponentially as a function of time t until the bubble reaches the maximal diameter at τ. The volume of the bubble increases

according to the following equation:

$$V_{\mathrm{b}} = V_{\mathrm{b},0} \cdot \, e^{c_{\mathrm{b}2}\, t}. \tag{3.57}$$

The constant $c_{\mathrm{b}2}$ is computed by means of the following equation in order to reach the maximal volume and the corresponding diameter:

$$c_{\mathrm{b}2} = \frac{\ln\left(V_{\mathrm{b,max}}/V_{\mathrm{b},0}\right)}{\tau}. \tag{3.58}$$

3.7.2 Bubble-Inclusion Attachment

During the simulations, it is assumed that bubble-inclusion attachment takes place, if the bubble and the inclusion come into contact. If this bubble-inclusion attachment occurs, the inclusion is deleted from the simulation and assumed to be removed from the melt. Furthermore, it is assumed that inclusions are not re-dispersed from the bubbles into the melt. The contact between the inclusions is not taken into account. Moreover, bubble coalescence is not considered.

The collision probability Ψ between bubbles and inclusions is determined as follows [138]:

$$\Psi = \frac{0.25\,\pi\,\left(d_{\mathrm{b}} + d_{\mathrm{p}}\right)^2\,\left|\boldsymbol{U}_{\mathrm{rel}}\right|\,\Delta t\,n_{\mathrm{min}}}{V_{\mathrm{cell}}}. \tag{3.59}$$

The determination of Ψ depends on the relative velocity between bubble and neighbour inclusions $\boldsymbol{U}_{\mathrm{rel}}$, time step Δt, volume cell V_{cell}, bubble diameter d_{b}, inclusion diameter d_{p} and the minimum number of inclusions or bubbles in the cell n_{min}. Ψ is calculated only between the bubbles and inclusions in the same cell. A random number ζ is generated here. If $\Psi > \zeta$, the collision between bubbles and inclusions takes place and the inclusion is deleted from simulation. This implementation is used in OpenFOAM as a standard function to detect the particles collision.

4 Results

The current chapter presents first a pure hydrodynamic (HD) model, which is created in order to mimic the recirculating melt flow in the ICF. Furthermore, the numerical results of the HD model are compared to the experimental results with the aim of validating the numerical model and the capability of the turbulence models to describe recirculating turbulent flow. Additionally, a magnetohydrodynamic (MHD) model is used to predict the flow in two configurations of the ICF. The MHD model is validated by using experimental data from literature. The calculation of the magnetic field and Lorentz force acting on the melt in the ICF is discussed here as well.

Furthermore, three hypotheses and their effect on inclusion removal are discussed. The first hypothesis is that the CO bubbles arise directly on inclusions in case of reactive cleaning. The second hypothesis is the formation of CO bubbles on the filter surface in case of reactive cleaning. The third hypothesis is the deposition of inclusions on the ceramic foam filter in case of active filtration. Moreover, the effect of the combination between reactive cleaning and active filtration on inclusion removal is presented. Finally, the effect of turbulence modeling on the prediction of the flow field and inclusion transport in the ICF is investigated in details.

4.1 Hydrodynamic Model

This section demonstrates the experimental water model that is employed to mimic the turbulent recirculating flow of the steel melt in the ICF. Partial results of the present section have already been published in Asad et al. [139].

4.1.1 Experimental Setup

The experimental configuration, which is built up to mimic the recirculating turbulent melt flow in the ICF, is displayed in Figure 4.1a. The important dimensions of the water model are shown in Figure 4.1b. The experimental setup features a solid square silicone (Elastosil RT601) container surrounded by plexiglass. Additionally, the silicone container has a hollow cylindrical center with a diameter of 18 cm, which is filled with a water-glycerin mixture (42:58 mass ratio). This mass ratio helps matching the refractive index of the silicone of the container ($n_\mathrm{r} = 1.4095$). This mixture is used instead of pure water in order to avoid the optical distortion. The mixture height is equal to the height of the cylindrical center. An impeller with a diameter of 6 cm is utilized in order to create similar recirculating turbulent flow to that taking place in the ICF. The impeller is located approximately at the half of the total height. The impeller is connected to a motor that is able to rotate the impeller in both directions and to drive the flow in the vessel with different rotational velocities. Moreover, eight guiding blades are located above the impeller. The main idea of using the guiding blades is to control the flow inside the vessel to generate the typical double vortex flow pattern, occurring in the ICF. The same impeller and same guiding blades are used by Stefani et al. [140] and Heinicke et al. [141] to generate a toroidal movement of liquid metal.

Measurement

PIV measurements are carried out to visualize the flow in the water model. For this purpose, the flow is seeded with polyamide particles, having a mean diameter of $d = 22$ µm and a similar density as the water-glycerin mixture. The tracer particles are illuminated by a continuous waver (CW) laser light sheet (Raypower 2000, Dantec) in the central cross section of the cylindrical vessel. A high speed camera (Phantom V12.1) acquires images of the illuminated cross section of the cylindrical vessel at a rate of 400 frames per second, thus leading to an exposure time of 2.5 ms. This time is short enough to avoid in-motion unsharpness by the CW-laser. The camera is equipped with a 35 mm lens (Nikon Nikkor 35 mm) and has an image resolution of 1280 px $\times$ 800 px. Then, the velocity vector maps are extracted from a cross correlation

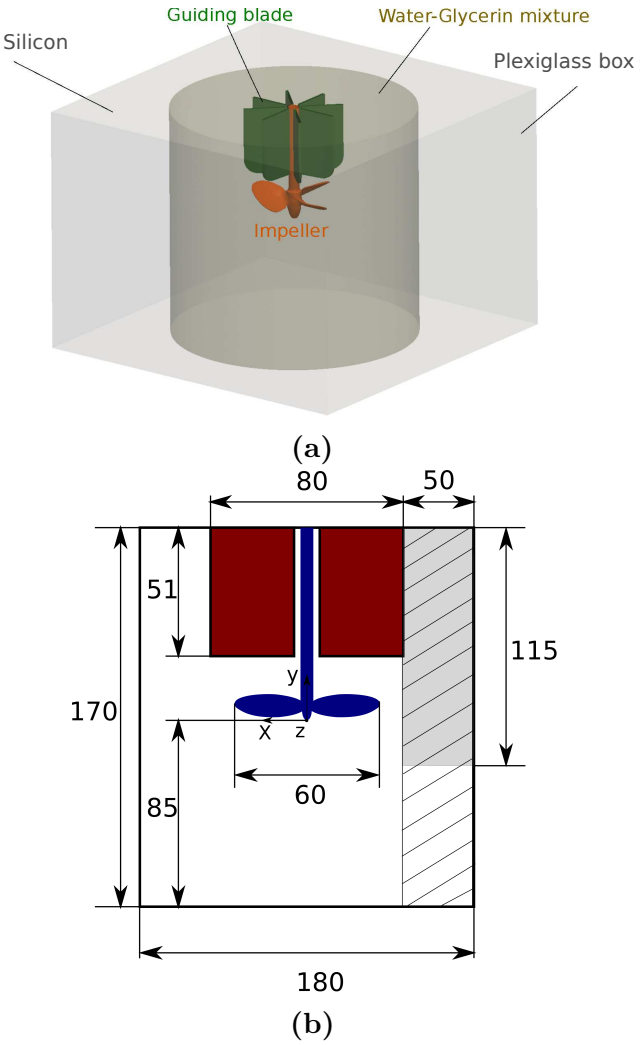

Figure 4.1: a) 3D sketch showing the component of the experimental setup and b) 2D sketch showing the important dimension of the experimental setup (units in mm); the gray area is the evaluated region in the experiment, while the hatched area represents the evaluated area in the simulation, the origin of the coordinate system is located at the tip of the impeller [139].

by using DaVis 8.4.0 software [142]. The interrogation window size is 16 px × 16 px with an overlapping of 50 %, leading to a resolution of 0.8 mm/vector. The rotational speed of the impeller is set to be $n = 400$ min^{-1} to prevent the occurrence of cavitation and to avoid the formation of air bubbles in the water tank. With this rotational speed, the Reynolds number, based on the maximal velocity and the radius of the vessel, is equal to Re $\approx$ 15000. Additionally, the rotating direction of the impeller is chosen to ensure similarity to the flow field in the ICF. Almost 3200 images are taken

over 8 s using the high speed camera. Each image is then evaluated only in the gray area shown in Figure 4.1b because it is not possible to evaluate the whole area with an acceptable resolution in the experiment. The extracted flow field from each image is used to determine the time-averaged flow field and turbulence properties.

4.1.2 Numerical Setup

The SST $k-\omega$ SAS turbulence model and ILES are used in order to simulate the flow inside the water model, which is created in order to mimic the recirculating turbulent flow in the ICF. In order to consider the rotation of the impeller, the sliding mesh approach is adopted with the appropriate interpolation schemes in order to realize the interaction between the fixed zone and the rotating zone over the interfaces. Multi-Reference frame (MRF) is another approach to consider the movement of the impeller, which provides steady-state solution with lower computational costs compared with the sliding mesh approach. However, the MRF approach is not able to reproduce reasonable results in this work because the impeller is relatively large compared to the diameter of the vessel [143]. The impeller rotates with a rotational velocity of $n = 400\ \mathrm{min}^{-1}$. The standard solver `pimpleDyMFoam` of OpenFOAM is adopted to perform the simulation. Table 4.1 lists the properties of the water-glycerin mixture in the simulation. The discretization schemes for the performed simulations are summarized in Table 4.2.

The geometry of the water model and the area, which is evaluated in the simulation, can be seen in Figure 4.1b. A computational grid with 6 million cells is used in the performed simulations. The grid is created using CFMesh software [144]. The maximal cell size in the rotor zone is set to 0.6 mm and in the fixed zone to 1.1 mm. The grid is locally refined on the impeller surface in order to align its complex geometry with a maximal cell size of 0.4 mm. Three boundary layers are generated at the walls of the impeller, guiding blades and water tank.

Table 4.1: Properties of the water-glycerin mixture.

Properties	Mixture (water-glycerin)
Density ρ_f $[\mathrm{kg\,m^{-3}}]$	1145
Dynamic viscosity μ_f $[\mathrm{kg\,s^{-1}\,m^{-1}}]$	$9.6 \cdot 10^{-3}$

Table 4.2: Discretization schemes for the performed simulations and their notation in OpenFOAM.

For all simulations and turbulence models			
Term	Equation	Discretization scheme	OpenFOAM
$\frac{\partial \overline{\boldsymbol{u}}}{\partial t}$	3.12	Backward differencing	`backward`
$\nabla \overline{\boldsymbol{u}}$	3.12	Central differencing	`Gauss linear`
∇p	3.12	Central differencing	`Gauss linear`
$\nabla \cdot (\nu_\mathrm{f} \nabla \overline{\boldsymbol{u}})$	3.12	Central differencing	`Gauss linear corrected`
$\nabla \cdot (\overline{\boldsymbol{u}}\, \overline{\boldsymbol{u}})$	3.12	Linear-upwind stabilized transport	`Gauss LUST unlimitedGrad(U)`
SST $k-\omega$ and SST $k-\omega$ SAS model			
$\frac{\partial \boldsymbol{k}}{\partial t}$	3.13	Backward differencing	`backward`
$\frac{\partial \boldsymbol{\omega}}{\partial t}$	3.14	Backward differencing	`backward`
∇k	3.13	Central differencing	`Gauss linear`
$\nabla \omega$	3.14	Central differencing	`Gauss linear`
$\nabla \cdot (\overline{\boldsymbol{u}}\, k)$	3.13	Upwind	`Gauss upwind`
$\nabla \cdot (\overline{\boldsymbol{u}}\, \omega)$	3.14	Upwind	`Gauss upwind`
Reaction model			
$\frac{\partial \boldsymbol{c}}{\partial t}$	3.47	Backward differencing	`backward`
$\nabla \cdot (\overline{\boldsymbol{u}}\, \boldsymbol{c})$	3.47	Linear-upwind stabilized transport	`Gauss LUST unlimitedGrad(U)`
$\nabla \cdot \left[\left(\frac{\nu_\mathrm{f}}{Sc} + \frac{\nu_\mathrm{t}}{Sc_\mathrm{t}}\right) \nabla c\right]$	3.47	Central differencing	`Gauss linear corrected`

The Courant number is set to be CFL = 1 during both simulations. This implies that the time step is varied during the simulation to ensure CFL = 1. The numerical results are time-averaged over 8 s.

4.1.3 Results

Velocity Field

Figure 4.2 compares the streamlines and the velocity magnitude of the time-averaged flow field obtained from experiment and simulations. This figure depicts that the flow pattern consists of two toroidal vortices. However, the lower vortex can not be seen completely in the figure of the experimental results (Figure 4.2a). Similar toroidal vortices can be found in the ICF.

The entire hatched area in Figure 4.1b is considered to show the results of numerical predictions. Comparing the results from experiment and simulations (see Figure 4.2), it is evident that the upper vortex is present as well in both simulations. The center of the upper vortex is placed approximately at the same position comparing flow patterns obtained experimentally and numerically. Nevertheless, the shape of the vortex in the simulation shows a minor deviation from that in the experiment. Additionally, Figure 4.2 indicates that both turbulence models predict similar toroidal vortex and velocity fields accurately.

The vorticity field $\Omega_z = \nabla \times \overline{\boldsymbol{u}}$ of the experiment is compared with that predicted numerically in Figure 4.3, which indicates that the numerical vorticity field deviates slightly from the experimental one close to the walls of the water tank. Moreover, the experimental results differ from that of the numerical simulations close to the impeller and the guiding blades. The reason for that difference may be the complexity of the flow in this region and the low capability of PIV and the numerical tools to predict the turbulent flow. As can be seen, the vorticity is higher in the upper vortex and near the wall of the tank, where the shear gradient is typically higher.

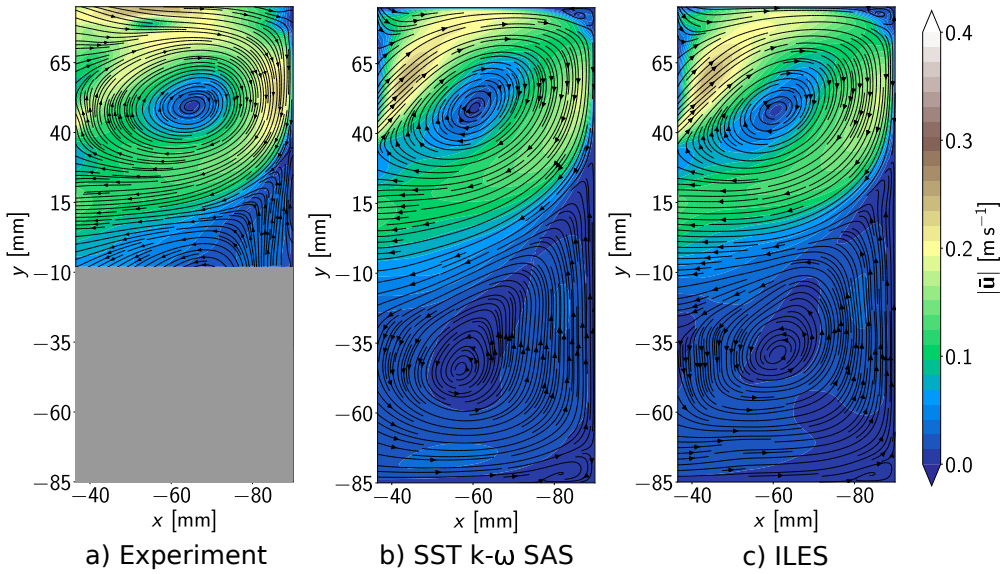

Figure 4.2: Streamlines and velocity magnitude of the time-averaged flow field of the experiment and simulations (ILES and SST $k-\omega$ SAS) in an axisymmetrical vertical plane of the water model [139].

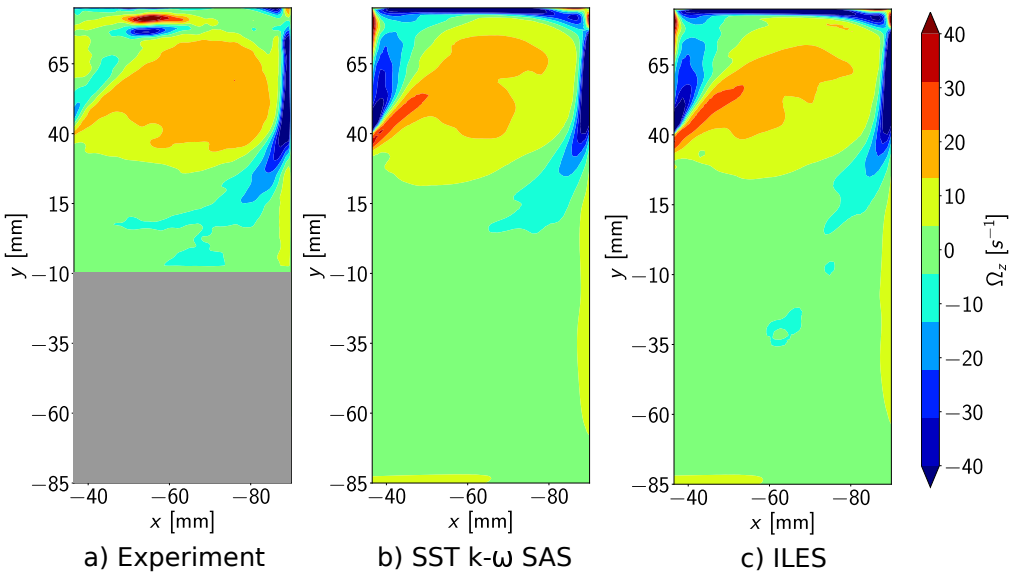

Figure 4.3: Comparison of the experimental vorticity field Ω_z with that predicted using simulations (ILES and SST $k-\omega$ SAS) in an axisymmetrical vertical plane of the water model [139].

Turbulent Kinetic Energy

The resolved turbulent kinetic energy in both numerical simulations is calculated as follows:

$$k = 0.5\,(\overline{u_x'^2} + \overline{u_y'^2} + \overline{u_z'^2}). \tag{4.1}$$

Figure 4.4 compares the turbulent kinetic energy resulting from the experiment with the numerical results. As can be seen, the numerical results of both simulations deviate from the experimental results. A possible reason for this deviation is the assumption of the isotropic turbulence in the evaluation of the experimental data that is used to determine the third contribution of the velocity vector. The turbulent kinetic energy in the simulations is higher in the region close to the impeller, where the flow is pushed upwards. Comparing the numerical results, the resolved turbulent kinetic energy is slightly higher in case of ILES.

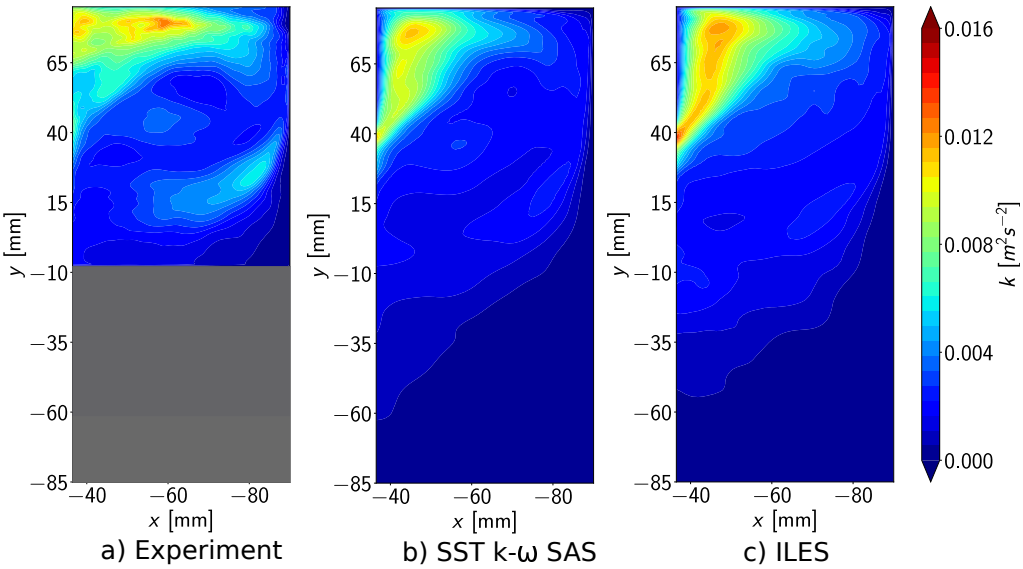

Figure 4.4: Comparison of turbulent kinetic energy k determined from the experiments with that predicted using numerical simulations (ILES and SST $k-\omega$ SAS) in an axisymmetrical vertical plane of the water model [139].

Summary

It can be concluded from the previous results that the simulations and the experiments show an acceptable agreement. That means that ILES as well as SST $k-\omega$ SAS turbulence modeling is able to predict a turbulent recirculating flow similar to that taking place in the ICF. Therefore, these models will be used further in this PhD thesis to simulate the recirculating turbulent flow of the melt in the ICF.

4.2 Magnetohydrodynamic Model

Two configurations are used in order to investigate the melt flow under alternating magnetic field in an ICF. The first configuration (ICF1) is an experimental setup investigated by Baake et al. [33]. It is employed to validate the full MHD numerical model. The flow velocity in ICF1 was measured by magnetic sensors. The second configuration (ICF2) is investigated at TU Bergakademie Freiberg in the frame of CRC 920 to test the efficiency of ceramic foam filters. It is not possible to measure flow velocity of the steel melt in this configuration. The following section compares the Lorentz force distribution and the flow field of ICF1 and ICF2. Some results of the current section have already been published in Asad et al. [32].

4.2.1 Simulation Setup

The operating fluid in ICF1 is Wood's alloy, whereas the operation fluid in ICF2 is steel melt. Table 4.3 summarizes the operating parameters of ICF1 and ICF2 as well as the properties of the operating liquids. ICF1 and ICF2 have different dimensions and geometries (see Figure 4.5). ICF1 has a sharp lower corner, while ICF2 exhibits a curved corner with a radius R_3. Table 4.4 contains the important dimensions of ICF1 and ICF2.

Table 4.3: Operation parameters of induction crucible furnaces and liquid properties [31–34].

Process parameters of the induction furnaces		
Quantity	ICF1	ICF2
Coil current (rms) I [A]	2000	180
Frequency f [Hz]	400	3400
Number of coil windings n [-]	12	10
Coil length l [m]	0.57	0.4
Magnetic field strength B [T]	0.069	0.01
Liquid properties		
Quantity	Wood melt	Steel melt
Density ρ_f [$\mathrm{kg\,m^{-3}}$]	9400	7000
Dynamic viscosity μ_f [$\mathrm{kg\,m^{-1}\,s^{-1}}$]	$4.2 \cdot 10^{-3}$	$6 \cdot 10^{-3}$
Magnetic permeability μ_0 [$\mathrm{H\,m^{-1}}$]	$1.257 \cdot 10^{-6}$	$1.257 \cdot 10^{-6}$
Electrical conductivity σ_f [$\mathrm{S\,m^{-1}}$]	$1 \cdot 10^{6}$	$7 \cdot 10^{5}$

Table 4.4: Important dimensions of the reference configuration (ICF1) and the induction crucible furnace investigated at TU Bergakademie Freiberg (ICF2) [32].

Dimensions [mm]	ICF1	ICF2
H_1	0	165
H_2	0	120
H_c	570	400
R_{c1}	197	222.5
R_{c2}	207	240
R_1	158	110
R_2	158	105
R_3	-	20
H_f	-	60
d_f	-	10

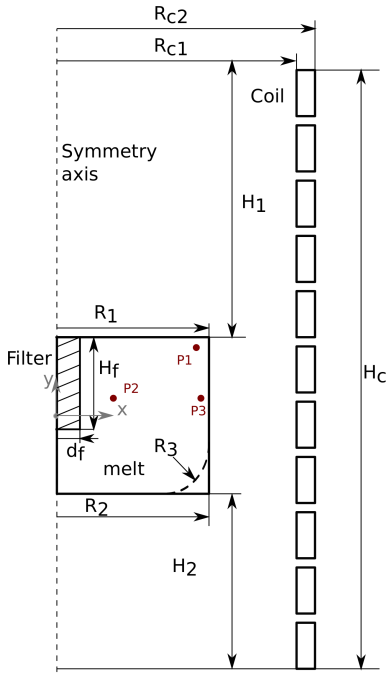

Figure 4.5: Axisymmetrical section of the reference configuration (ICF1) and the induction crucible furnace investigated at TU Bergakademie Freiberg (ICF2) with the important dimensions. Points P1, P2 and P3 are monitoring points in ICF2, which are located at (100 47 0), (60 10 0) and (105 10 0) mm [32].

In both simulations, ILES is adopted to describe the turbulent melt flow in ICF1 and ICF2. The computational grid is generated using CFMesh software [144]. The grid of ICF1 and ICF2 has approximately $4 \cdot 10^6$ computational cells with a maximal cell size of 2.3 mm. Three boundary layers are created at the walls and top surface of the crucibles. The free surface is considered as a flat slip wall and its deformation is disregarded. This means that the fluid can only be accelerated in the horizontal direction. The crucible's walls are considered to be no-slip walls. In the simulations, no wall function is used. The dimensionless wall distance y^+ exhibits at the crucible walls an averaged value of $y^+ = 1$, which ensures enough description of the flow close to the wall in the LES simulation [145, 146]. Table 4.2 summarizes the discretization schemes in the simulation.

The numerical results of all simulations are averaged over 300 s. In order to avoid the effect of initial flow field on the time-averaged flow field, the time-averaging is started

after the flow is completely developed ($t = 30$ s). In the simulations, the time step is set to be 0.001 s.

4.2.2 Magnetic Field

Figure 4.6 provides the distribution of the Lorentz force in an axisymmetrical section of ICF1 and ICF2. As expected, the Lorentz force is concentrated and higher close to the crucible wall due to the skin effect in the ICF. Comparing the distribution of the Lorentz force in ICF1 and ICF2, it is evident that the Lorentz force is much higher in case of ICF1 because of the higher magnetic field induction in this case. The distribution of the Lorentz force in ICF1 is mirror symmetrical as can be seen in Figure 4.6a. The explanation for the symmetrical distribution of the Lorentz force in ICF1 is the symmetrical position of the melt in the magnetic field relative to the coil ($H_1 = H_2 = 0$). Moreover, one can see that the magnitude of the Lorentz force has nearly similar value along the wall of ICF1. On the contrary, the distribution of the Lorentz force in ICF2 is not mirror symmetric by comparing the upper and lower corners of the melt. The asymmetry of the Lorentz force is caused by the asymmetrical position of the melt relative to the coil ($H_1 \approx 4/3\ H_2$) and the asymmetrical geometry. Furthermore, it is clear that the Lorentz force varies along the wall of ICF2 and has higher values close to the upper and lower corners.

4.2.3 Time-Averaged Flow Field

Figure 4.7a shows the time-averaged flow field and flow streamlines in ICF1. From this figure, it is evident that the time-averaged flow field in the vertical midplane consists mainly of two toroidal vortices. This toroidal flow structure originates from the interaction between the flow coming from the top and bottom of the crucible along the side wall. Additionally, high velocities can be found close to crucible sidewalls, while low velocities can be observed in the region between the upper and lower vortices. Despite the long averaging time, a slight asymmetry can still be found due to the long-term oscillations of the flow, which typically dominate the flow in the ICF [33, 35–37]. The upper and lower toroidal vortices are located nearly symmetrical because the Lorentz force distribution acting on the liquid is symmetrical along the side wall

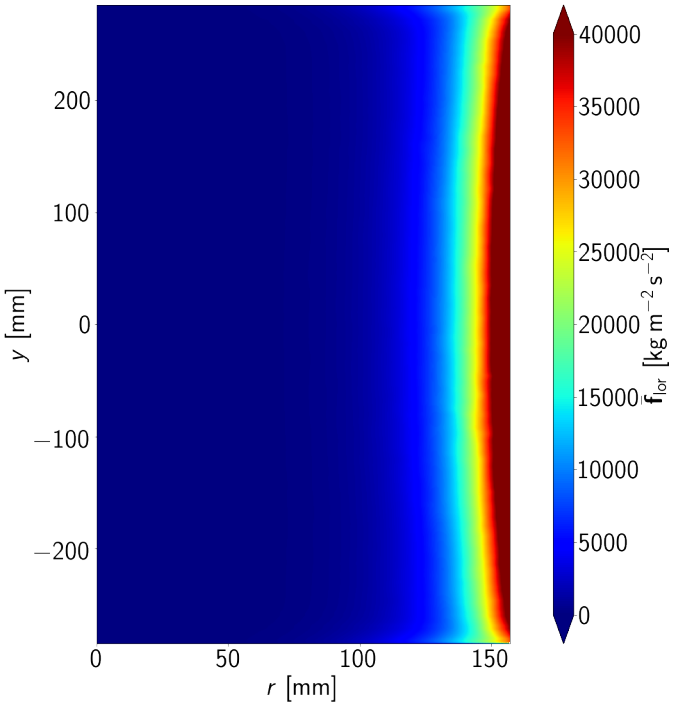

(a) ICF1

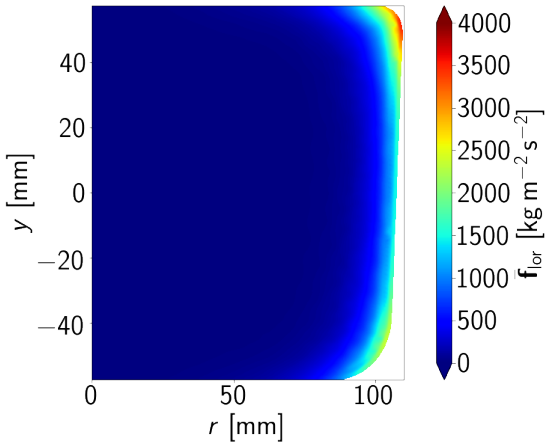

(b) ICF2

Figure 4.6: Distribution of the Lorentz force $\overline{\boldsymbol{f}}_{\mathrm{lor}}$ in an axisymmetrical section of the investigated induction crucible furnaces (ICF2 and ICF2) [32].

of the crucible (see Figure 4.6a). The horizontal plane possesses secondary vortices and slight asymmetry as well.

Figure 4.7b presents the time-averaged velocity field and flow streamlines of ICF2. As can be seen, the flow is dominated by a large toroidal vortex in the vertical plane. Moreover, a small toroidal vortex can be seen close to the upper corner of the melt. The asymmetry between the lower and upper vortex is caused by the asymmetrical distribution of the Lorentz force along the side wall of the crucible (see Figure 4.6b). Secondary vortices and fluctuations exist in the time-averaged flow field in the horizontal plane. Despite the axisymmetrical flow setup and relatively long averaging time, the time-averaged flow field in the vertical and horizontal plane has a slight asymmetry due to the typical long-term oscillation of the flow.

In order to validate the performance of the numerical model to reproduce the flow field in the ICF, the vertical velocity of the flow $\overline{u}_{\mathrm{y}}$ obtained from the simulation is compared with the experimental data of ICF1 over Line 1 (see Figure 4.7a) in Figure 4.8 [33]. Here, it is shown that the numerical model is able to reproduce the mean flow field in the ICF. The numerical velocity profile agrees well with the experimental one. In the following sections, only ICF2 will be investigated using the validated numerical model.

Summary

One can conclude from the previous results that the Lorentz force distribution has a considerable impact on the melt flow in the ICF. The shape of the toroidal vortices and the velocity field in the ICF rely on the relative position of the coil to the melt and the level of the melt in the crucible.

The MHD model is validated in the previous section as well and shows a good capability to predict the MHD flow in the ICF. Consequently, the model will be used later to simulate the melt flow in ICF2.

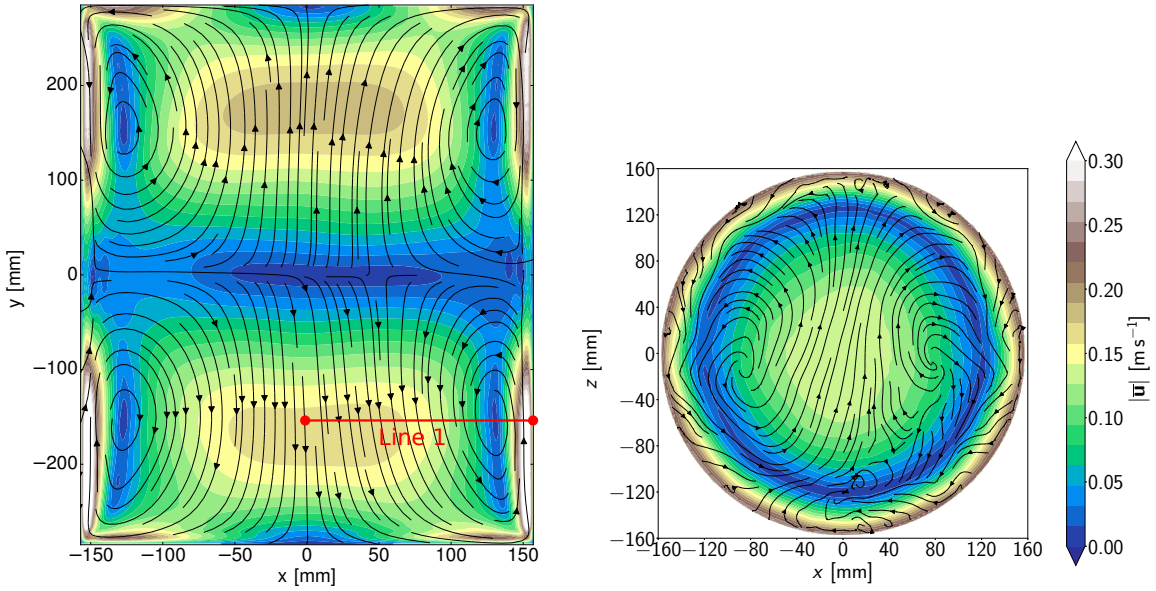

(a) ICF1

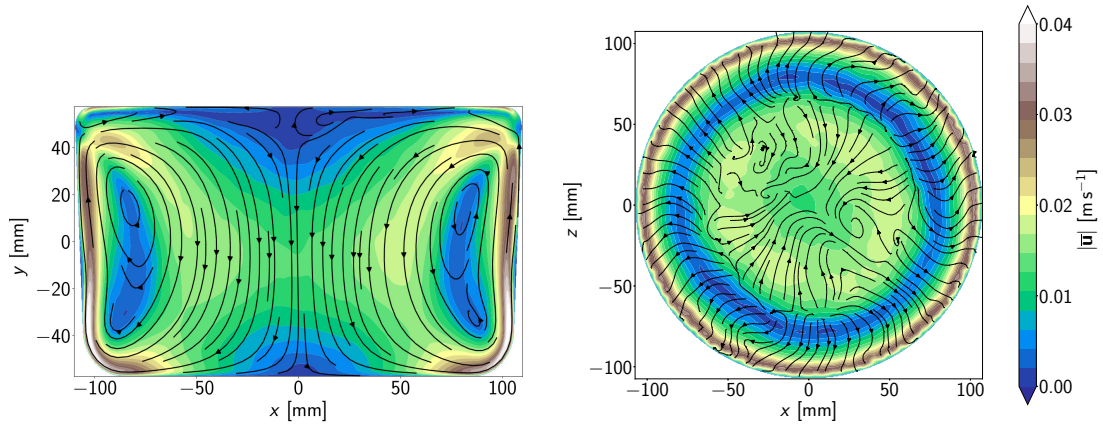

(b) ICF2

Figure 4.7: Magnitude of the time-averaged flow velocity and streamlines in the vertical midplane (left) and in a horizontal plane (right) of ICF1 and ICF2. The horizontal plane is located at $y = 150$ mm for ICF1 and at $y = 0$ for ICF2. Line 1 is a sampling line to compare the numerical and experimental results of ICF1 and is placed at y = -158 mm between $x = 0$ and $x = 158$ mm [32].

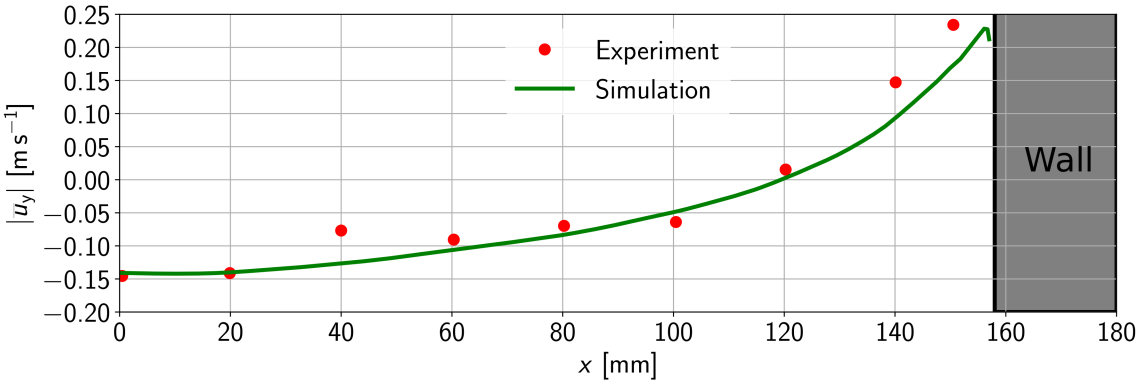

Figure 4.8: A comparison between the numerical results of the time-averaged vertical flow velocity in ICF1 $\overline{u}_y$ and the experimental data [33] over Line 1 (see Figure 4.7a) [32].

4.3 Reactive Cleaning

The efficiency of the ceramic foam filters immersed into the steel melt in ICF2 was determined numerically by Asad et al. [115] and experimentally by Storti et al. [20]. The comparison between the numerical and experimental results indicates that the filtration efficiency of the filter detected in the simulation is greatly less than that determined in the filtration experiment in spite of the long filtration time in the simulation. A possible reason for this huge difference might be that the simulation has not considered the reactive effect of the filter and the possible formation of CO bubbles on inclusions and filter surface.

Therefore, the effect of reactive cleaning and CO bubble formation on melt cleanliness is investigated in ICF2. Furthermore, the impact of bubble formation on the flow field is shown in the following results. These bubbles can form owing to the reaction between carbon dissolved from the filter and oxygen available in the melt. Here, it is assumed that this reaction takes place either on the inclusion surface or on the filter surface. A comparison of the cleanliness level of the melt obtained in case of bubble formation on inclusions with that determined in case of bubble formation on the filter surface is discussed through the following results. Partial results about the effect of bubble formation at inclusion surface and filter surface on the flow field, concentration field, particle distribution and melt cleanliness have already been published in Asad et al. [77, 136].

4.3.1 Simulation Setup

The same grid of ICF2 used in section 4.2 is employed in the following simulations. ILES is adopted to simulate the melt flow in ICF2. The discretization schemes used here are summarized in Table 4.2. In the simulations, the time step is equal to $\Delta t = 0.001$ s.

After the flow is fully developed ($t = 30$ s), $2 \cdot 10^6$ inclusions with a diameter of $d_\mathrm{p} = 5$ µm and a density of $\rho_\mathrm{p} = 3200\ \mathrm{kg\,m^{-3}}$are injected at random positions over the whole top surface of the melt (free surface). Afterwards, the inclusions are mixed in the melt for further 30 s of flow time. After the inclusions are well distributed in the flow field, the filter is inserted in the melt for 10 s. Then, the filter is removed from the melt and the alternating magnetic field is disabled similar to the experiment conducted by Dudczig et al. [4] and Storti et al. [20]. The solidification time is approximately 10 min after the magnetic field is disabled as determined in the experiment. Therefore, the simulation is continued for further 100 s after disabling the magnetic field in order to mimic the aspect, that the inclusions can float up until the steel melt is solidified. However, it is worth mentioning that the solidification is not taken into account in the model.

For the case of bubble formation on inclusion surface, the transport equation of carbon (see Equation 3.47) is solved to consider the transport of carbon from the filter into the melt. Firstly, it is assumed that the concentration of carbon in the filter is equal to $c = 1\ \mathrm{mol\,m^{-3}}$ and does not decrease during the immersion time of the filter (10 s). However, the concentration of carbon may decrease on the outer surface of the filter in the filtration process because of many reasons, e.g. the formation of in-situ layers on the filter wall [78]. These layers prevent carbon to diffuse to the outer surface of the filter. Therefore, the effect of the possible decrease of carbon concentration on melt cleanliness is investigated. Here, it is assumed that the concentration can decrease either linearly or exponentially to a certain prescribed concentration c_min during the immersion time of the filter. In all simulations, the initial concentration of carbon in the melt is set to be $c = 0$. The filter is the only source of carbon in the flow domain. Moreover, it is assumed that the concentration of oxygen does not decrease in the flow field and the melt has enough oxygen for the reaction.

For the case of bubble formation on filter surface, the bubble volume is assumed to increase linearly or exponentially to cover the possible quick and slow increase of the bubble volume. The bubble volume is increased until the bubble diameter reaches the prescribed maximal bubble diameter $d_{\mathrm{b,max}}$ as described in section 3.7. Each bubble can reach $d_{\mathrm{b,max}}$ after 10 s from the injection time. For these cases, it is assumed that the bubble leaves the filter with a diameter of 1 µm. This assumption is supported by the fact that it is not possible to detect, at which diameter the bubble can leave the filter. Besides the assumption of volume increase, the bubbles are initialized with $d_{\mathrm{b,max}}$, which remains constant during the simulation. Due to the fact that it is impossible to detect the position at which the bubble forms in the real filtration experiment, the bubbles are initialized at the filter surface from 32 points. The points are located only in the lower half of the filter to ensure a long residence time of the bubbles in the melt before leaving the flow domain. 100 bubbles per second are injected from each point on the filter surface. For these investigations, three maximal diameters are chosen, $d_{\mathrm{b,max}} = 100, 300, 500$ µm. This range is chosen to ensure that the bubble remains spherical during the simulations [120]. In contrast to the case of bubble formation on inclusion surface, the transport of carbon in the melt is disregarded in this case.

In the following simulations, filters with a pore density of 10 ppi are utilized. The properties of the filters are summarized in Table 3.1. It is worth mentioning that the inclusions can not be removed by the filter in this section in order to focus on the effect of bubble formation on melt cleanliness.

4.3.2 Bubble Formation on Inclusions

In this section, the effect of CO bubble growth at inclusion surface on the cleaning efficiency as well as on melt cleanliness is investigated. The volume of these bubbles can only increase due to the reaction between carbon and oxygen as described in section 3.6. Here, it is worth noting that an equivalent particle represents an inclusion with a rising CO bubble in the following results. As mentioned previously, the agglomeration of inclusions and equivalent particles is neglected to simplify the model in this case.

Case 1: Constant Concentration

The concentration of carbon in the filter is kept constant during the immersion time of the reactive filter (10 s), which means that the filter is a constant source of carbon during this time. Carbon can be dissolved from the reactive filter and transported into the melt, which leads to an increase in carbon concentration in the flow field.

Time-Averaged Flow Field

The flow field is averaged only over the immersion time of the filter (10 s) during the acting of the magnetic field. It dose not make sense to average the flow field after disabling the magnetic field because the flow velocity decreases quickly till the melt is at rest owing to the absence of the driving Lorenz force. Figure 4.9 presents the time-averaged flow field in the vertical midplane and in the horizontal plane at $y = 0$. From this figure, it is distinct that the flow is affected by inserting the filter in the melt. The filter lowers the velocity in the central region of the crucible because of the flow resistance of the porous filter. Similar to the case without using a filter (see Figure 4.7b), the flow is dominated by a large toroidal vortex as can be seen in the vertical plane. It is evident that the melt velocity is higher close to the filter compared to the case without bubble formation discussed later in section 4.6. This is caused by the quick flotation of the large equivalent particles during the immersion time close to the filter and the two-way coupling between the equivalent particles and the melt. This phenomenon enhances the transportation of carbon from the filter into the melt by increasing the velocity close to the filter. In the horizontal plane, the time-averaged flow field possesses deviation from axisymmetry, where small secondary vortices can still be seen in spite of time-averaging of the flow. Moreover, one can see that the filter leads to a decrease in the flow velocity in the filter region.

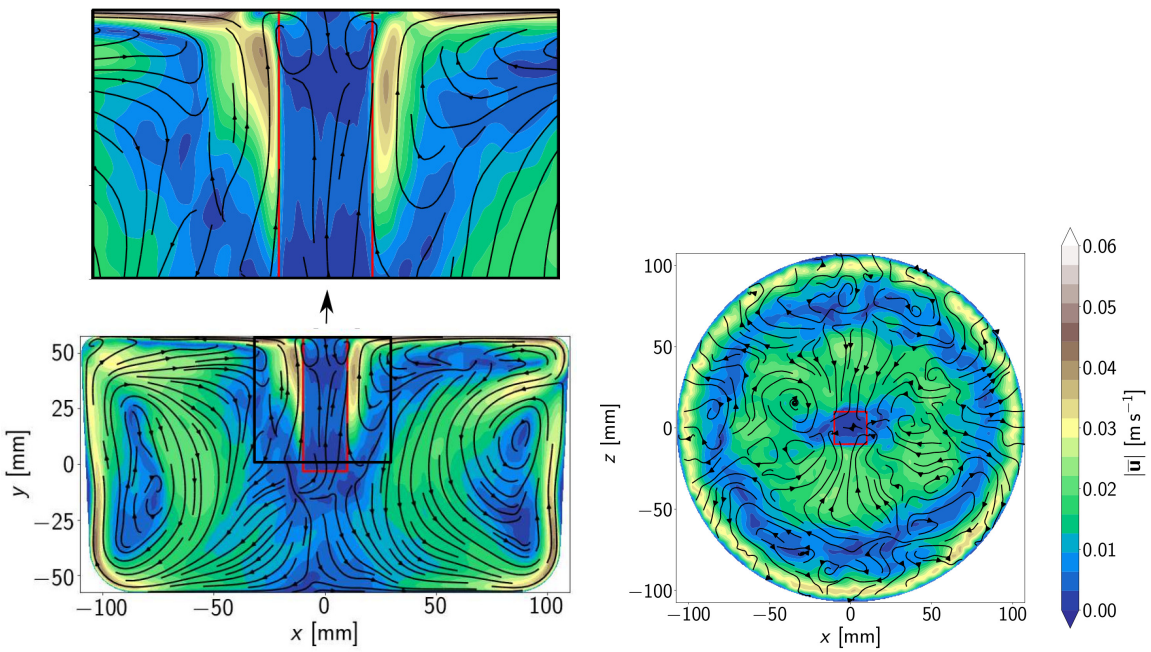

Figure 4.9: Magnitude of the time-averaged velocity field $\overline{\boldsymbol{u}}$ and streamlines of the melt in the vertical midplane (left) and in the horizontal plane at $y = 0$ (right) of the induction crucible furnace (ICF2). The red rectangle represents the location of the filter.

Instantaneous Flow Field

Figure 4.10 depicts a snapshot of the instantaneous velocity field at $t = 10\,\mathrm{s}$ in the vertical midplane and in the horizontal plane at $y = 0$ of ICF2. As can be seen, the flow field shows many turbulent structures in both planes, which are known to improve the mass and heat transport in the melt. Similar to the time-averaged flow field, the melt velocity is high close to the filter because of the quick flotation of large equivalent particles. Moreover, the velocity is high at some positions inside the filter because of the quick flotation of the equivalent particles inside the filter. As mentioned previously, the particles can not be captured by the filter in this case.

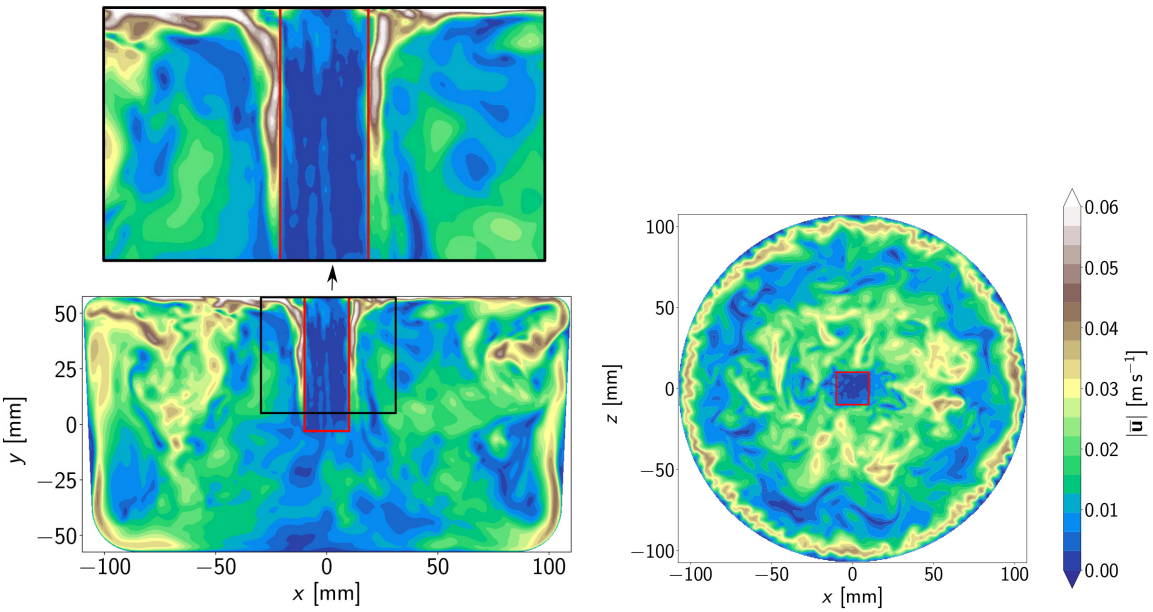

Figure 4.10: Instantaneous velocity field $\overline{\boldsymbol{u}}$ in the vertical midplane (left) and in the horizontal plane at $y = 0$ (right) of the induction crucible furnace (ICF2) at time $t = 10$ s. The red rectangle represents the location of the filter [77].

Carbon Concentration

The carbon concentration in the flow field at $t = 1$ s and $t = 10$ s is displayed in the vertical midplane and in the horizontal plane at $y = 0$ in Figure 4.11. This figure shows that the carbon concentration is higher close to the filter. Comparing the carbon concentration at $t = 1$ s and $t = 10$ s, one can see that the carbon concentration is increased at new positions in the flow field with increasing simulation time. This means that the reaction can take place also at regions far from the filter.

Figure 4.12 presents the volume-averaged concentration of carbon c_{avg} in the flow field. Here, the concentration is averaged over the whole flow domain except the region where the filter is located. This figure indicates the increase of c_{avg} during the immersion time of the filter because the filter supplies continuously carbon to the melt in this time period. After the filter is removed from the melt, c_{avg} decreases rapidly to zero because carbon can still react with oxygen on the inclusions. This leads to a reduction in the carbon concentration. As mentioned, the reduction of carbon is described by the sink term in the transport equation of carbon (see Equation 3.47).

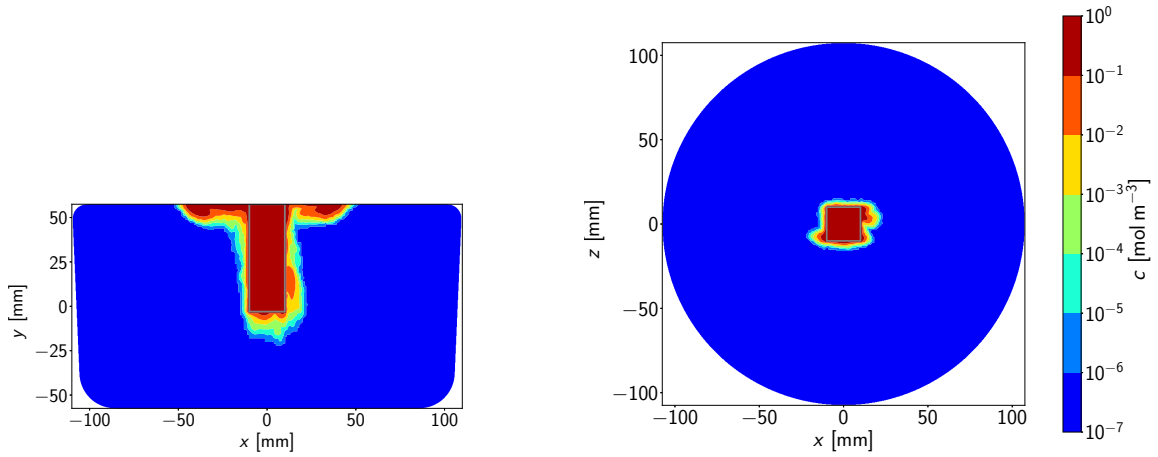

(a) $t = 1$ s

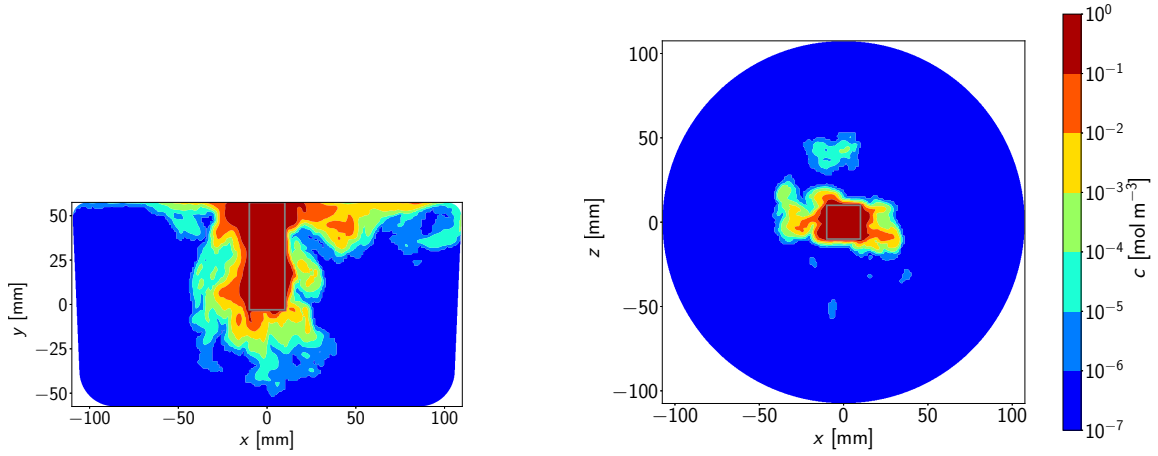

(b) $t = 10$ s

Figure 4.11: Concentration of carbon in the vertical midplane and in the horizontal plane at $y = 0$ of ICF2 at two different time steps [77]. The gray rectangle represents the location of the filter.

Particle Size Distribution

The distribution of the equivalent particles at two different time steps is displayed in Figure 4.13. In this figure, only equivalent particles with a diameter $d_{\text{eff}} > d_{\text{p}}$, are displayed. Here, one can see that the size of the equivalent particles is larger close to the filter due to the high concentration of carbon in this region as already shown in Figure 4.11. In this region, the equivalent particle grows and floats up quickly to the free surface of the melt.

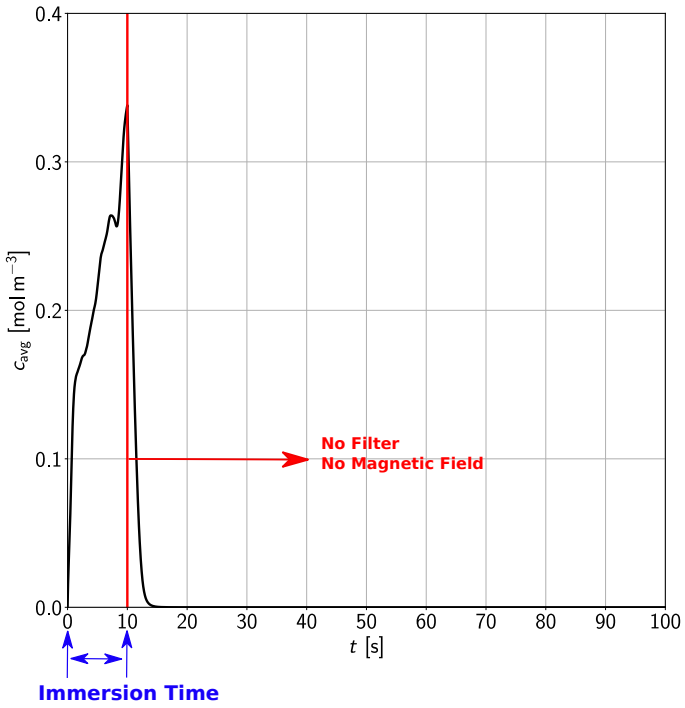

Figure 4.12: Plot of the volume-averaged concentration of carbon c_{avg} over time.

Carbon is better transported away from the filter over simulation time. This means that the reaction can take place close to the filter as well as in the side regions of the crucible. Then, CO bubbles can form on the inclusions, which are present far from the filter as well. This explains the reason for increasing the size of equivalent particles existing far from the filter. Because of the wetting properties, the inclusions reaching the free surface have very low probability to be re-dispersed into the melt. Therefore, each particle, that reaches the free surface, is assumed to stick there. Then, it is deactivated. This means that they can not follow the melt flow again. Moreover, these particles can not grow further because of the reaction.

Figure 4.14 compares the size distribution of the equivalent particles at two different time steps. The size distribution includes the particles, which stick at the free surface as well. From this figure, it is distinct that the particles size increases with time due to the reaction. The particles number with the initial diameter (5 µm) decreases comparing the size distribution at $t = 1$ s and $t = 10$ s.

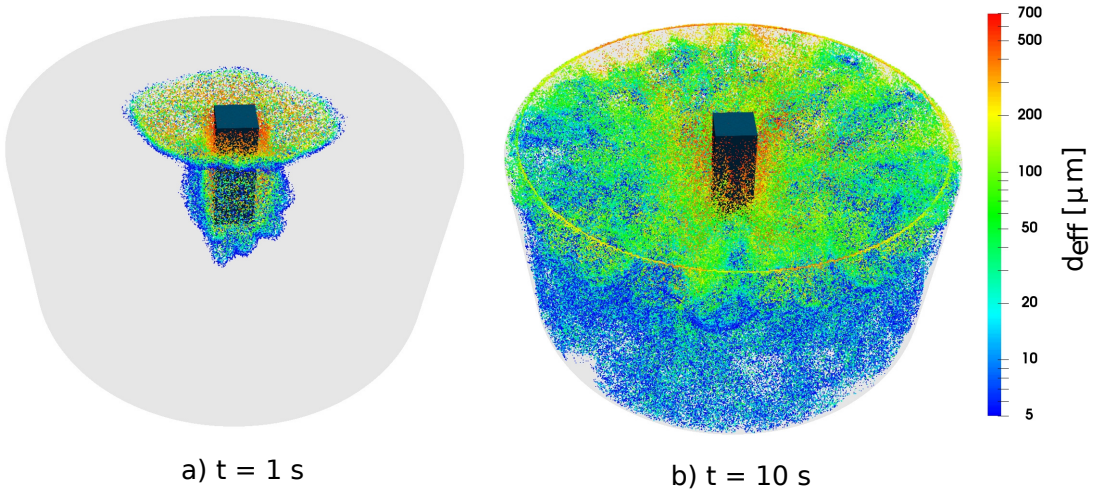

Figure 4.13: Distribution of equivalent particles at different times after immersion of the filter at $t = 0$ s. The equivalent particles have grown because of the formation of bubbles on their surfaces. The dark green cuboid denotes the position of the filter [77].

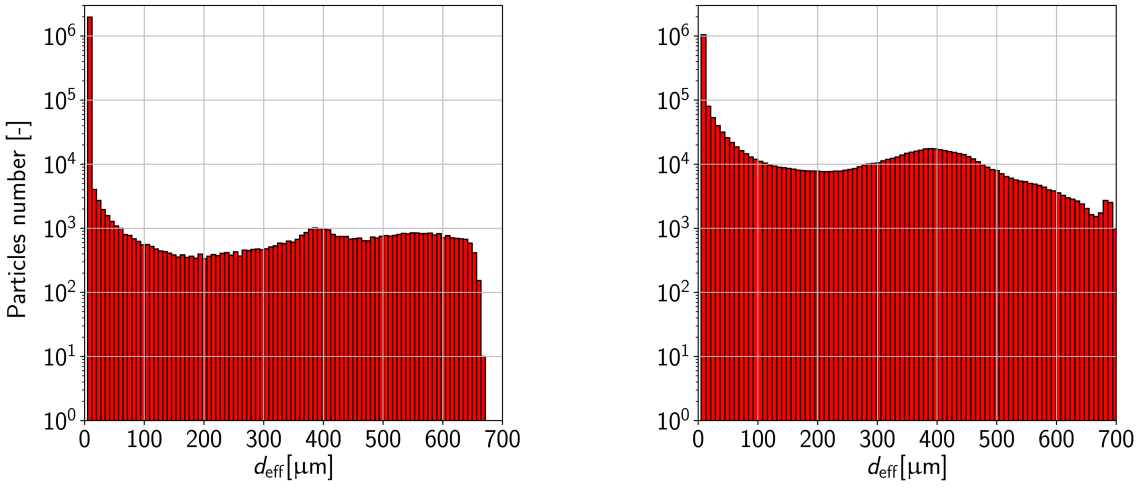

(a) $t = 1$ s **(b)** $t = 10$ s

Figure 4.14: Size distribution of the equivalent particles at two different time steps in case of the bubble formation on inclusion surface and constant concentration of carbon in the filter.

Cleanliness of Melt

Figure 4.15 indicates the considerable influence of the formation of CO bubbles on the melt cleanliness. The ratio of the initial number of inclusions to the number of inclusions captured by the free surface represents the cleanliness level of the melt η. As can be seen in Figure 4.15, it is clear that the number of inclusions reaching the free surface, increases over simulation time. About 30 % of the inserted inclusions are captured by the free surface after 10 s. This finding indicates the significant influence of bubble formation on the cleanliness of the steel melt. The inclusions can still float up and reach the free surface after the magnetic field is disabled (after 10 s), which enhances the melt cleanliness. In Figure 4.15, it is evident that η increases over 60 % after 100 s of simulation time.

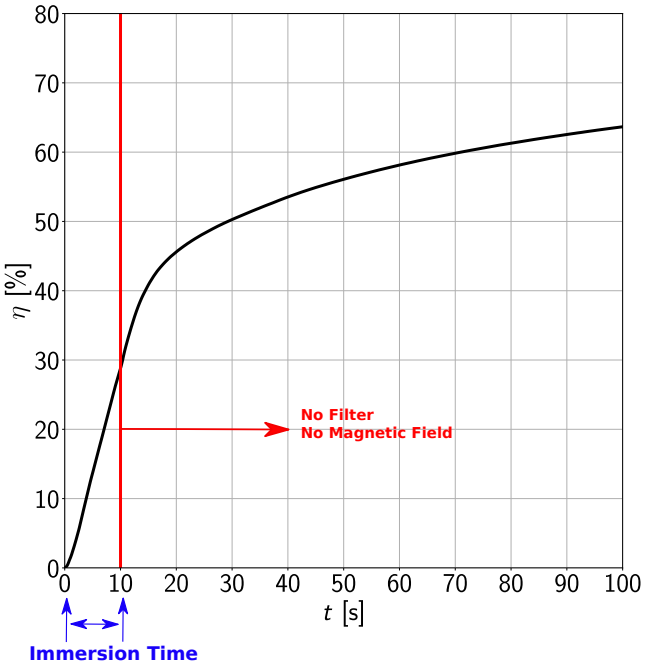

Figure 4.15: Increase of steel cleanliness during simulation time due to the effect of carbon monoxide bubble arising on inclusions [77].

A similar filtration experiment was conducted by Storti et al. [20], where samples of solidified steel were analyzed by ASPEX analyzing approach. The authors found that $60 - 95$ % of inclusions were removed from the melt due to reactive cleaning. Moreover, the authors shown that this value depended considerably on the filter type.

The bubble formation may indicate the reason for the deviation between the low filtration efficiency determined by Asad et al. [115] and that measured in Storti et al. [20], where Asad et al. [115] considered only pure active filtration in ICF2.

One can conclude that the bubble formation on inclusions contributes considerably to enhance the cleanliness of the melt. A high cleanliness level of the melt is obtained during a relatively short immersion time of the filter. It is much higher than that detected in the simulation of active filtration performed by Asad et al. [115]. This indicates that reactive cleaning and activating the bubble formation on inclusions play a significant role to improve the level of melt cleanliness.

Case 2: Concentration Decrease

In contrast to the previous section, the carbon concentration in the filter decreases either linearly or exponentially over the immersion time of the filter to reach the prescribed minimal concentration of carbon $c_{\min}$ at the end of the immersion time (10 s). The minimal concentration is assumed to be either $c_{\min} = 0 \text{ mol m}^{-3}$ or $c_{\min} = 0.5 \text{ mol m}^{-3}$.

As the flow field here is similar to that in case of constant concentration, it is skipped here to avoid any kind of repetition.

Carbon Concentration

Figure 4.16 compares the concentration distribution of carbon in the vertical midplane of the flow field at $t = 10$ s, if the concentration decreases linearly or exponentially to $c_{\min}$. In case of $c_{\min} = 0 \text{ mol m}^{-3}$, a big difference between the exponential and linear decrease is clearly to be seen. At $t = 10$ s, the carbon concentration is nearly zero in the whole flow field in case of the exponential decrease with $c_{\min} = 0 \text{ mol m}^{-3}$. This implies that the reaction between carbon and oxygen can not take place after removing the filter because carbon is not available in the flow field for further reaction. That has certainly a negative effect on inclusion removal. On the contrary, the concentration is high close to the filter in case of the linear decrease with $c_{\min} = 0 \text{ mol m}^{-3}$. In case of $c_{\min} = 0.5 \text{ mol m}^{-3}$, the concentration distribution is similar in both cases.

The concentration is clearly higher than the cases with $c_{\min} = 0\ \mathrm{mol\,m^{-3}}$, especially close to the filter. This plays a significant role in the bubble formation and inclusion removal because the reaction can take place further after removing the filter from the melt as well. CO bubbles can continue to grow and form on inclusions.

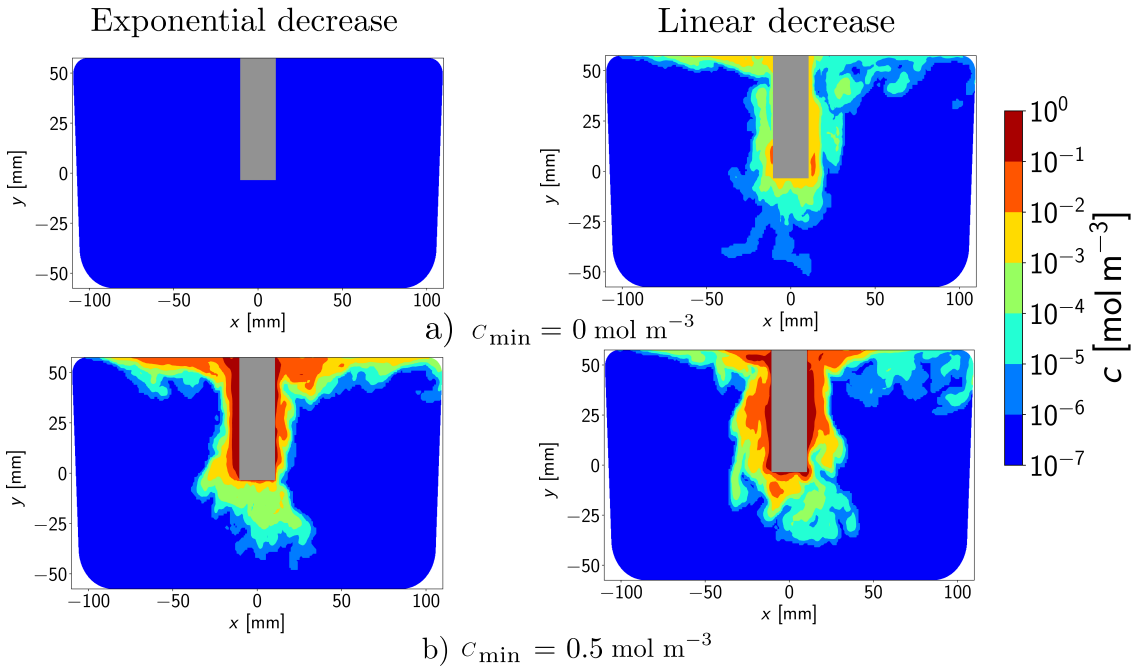

Figure 4.16: Concentration of carbon in the midplane of ICF2 for two different values of $c_{\min}$ at $t = 10$ s. The gray rectangle represents the position of the filter.

Particle Size Distribution

A comparison of the size distribution of equivalent particles between the considered cases at $t = 10$ s is shown in Figure 4.17. In this figure, the equivalent particles in case of the exponential decrease with $c_{\min} = 0\ \mathrm{mol\,m^{-3}}$ are much smaller than the equivalent particles in the other investigated cases. The reason for this fact is the low concentration of carbon in the flow field compared to the other cases as demonstrated in Figure 4.16. Then, the reaction can not often take place. As shown previously, the concentration field is nearly similar in case of the linear and exponential decrease with $c_{\min} = 0.5\ \mathrm{mol\,m^{-3}}$. This reflects the similar size distribution of the particles for these cases.

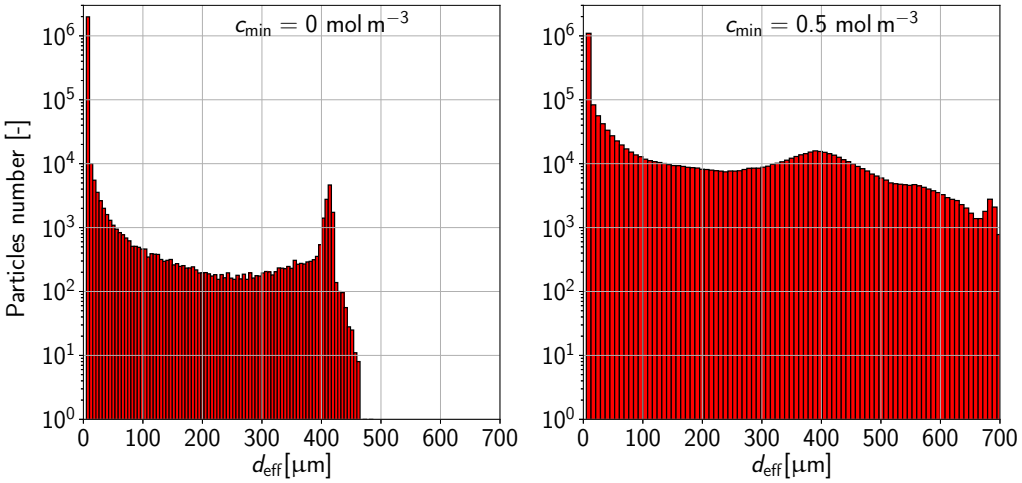

(a) Exponential decrease

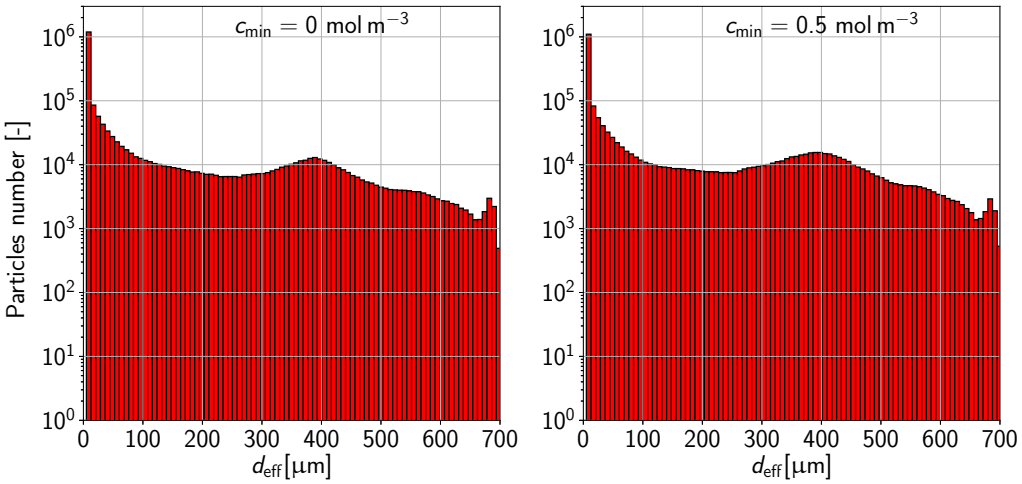

(b) Linear decrease

Figure 4.17: Size distribution of the equivalent particles in case of the exponential and linear decrease of carbon concentration in the filter over its immersion time at $t = 10$ s.

Cleanliness of Melt

The effect of the concentration reduction on the melt cleanliness in case of $c_{\min} = 0\ \mathrm{mol\,m^{-3}}$ is compared with the case of constant concentration of carbon (see section 4.3.2) in Figure 4.18, which shows that the concentration decrease has a negative effect on the melt cleanliness and inclusion removal. If the carbon concentration in

the filter decreases, the number of the removed inclusions is reduced. The number of the inclusions floating to the free surface of the melt is remarkably low in case of the exponential decrease compared to the other cases.

Comparing η in Figure 4.19, one can notice that the difference between the linear and exponential decrease in case of $c_{\min} = 0.5\ \mathrm{mol\,m^{-3}}$ is not huge in contrast to the case of $c_{\min} = 0\ \mathrm{mol\,m^{-3}}$. However, η is still higher in case of the constant concentration compared to the other cases.

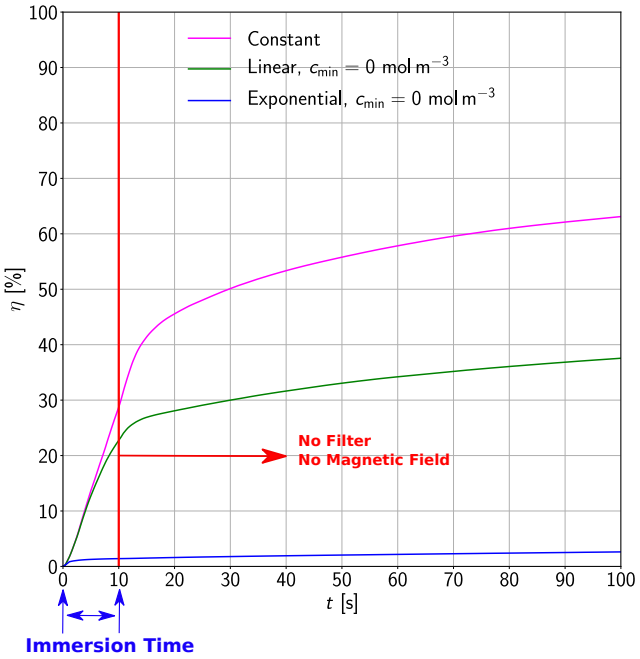

Figure 4.18: Increase of steel cleanliness during simulation time due to the effect of carbon monoxide bubble arising on inclusions in case of the concentration decrease with a minimal value of $c_{\min} = 0\ \mathrm{mol\,m^{-3}}$.

Summary

The results of the numerical simulations performed in the previous section indicate the importance of bubble formation on inclusions for enhancing inclusion removal and the corresponding melt cleanliness. By activating the bubble formation on inclusions, a high level of melt cleanliness is achieved within a short immersion time of the filter. Moreover, the results may explain the main difference between the filtration

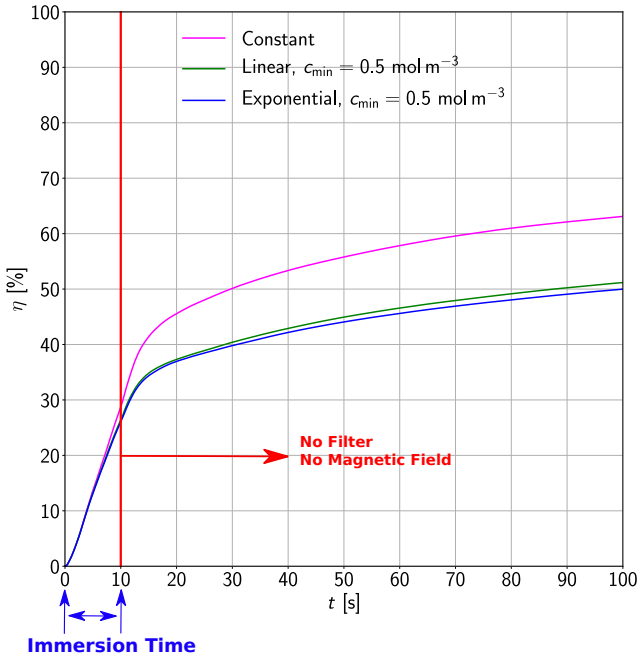

Figure 4.19: Increase of steel cleanliness during simulation time due to the effect of carbon monoxide bubble arising on inclusions in case of the concentration decrease with a minimal value of $c_{\min} = 0.5\ \mathrm{mol\,m^{-3}}$.

experiment conducted by Storti et al. [20] and the numerical investigation performed by Asad et al. [115], where the reactive effect of the filter are not taken into account.

Moreover, the results show that the decreasing tendency of carbon in the filter has an influence on the concentration field and on the size of the CO bubbles as well as on the size of the corresponding aggregate of bubbles and inclusions. This affects certainly the cleanliness of the melt. Therefore, it is important to study the possible reasons for the reduction of carbon on the filter surface. For instance, the formation of in-situ layers has to be studied in more details to enhance the diffusion of carbon to the outer surface of the filter.

4.3.3 Bubble Formation on Filter Surface

The impact of the bubble formation at the filter surface on the cleaning efficiency is investigated in this section. It is not possible to describe the real process of the bubble formation on the rough surface of the filter because the filter is represented only as a region with defined permeability and Forchheimer's coefficients in the simulations

(see section 3.3.2). Therefore, some assumptions have to be considered with the aim of investigating the impact of bubble formation at the filter surface on inclusion removal.

The volume of the bubble can increase either linearly or exponentially until the bubble reaches the prescribed maximum diameter $d_{\mathrm{b,max}}$. The linear and exponential increase are investigated in order to cover the quick and slow possible increase of the bubble volume. The increase behavior of the bubble volume for both cases is explained in section 3.7. In another case, the bubbles are injected at the filters wall with $d_{\mathrm{b,max}}$ and their volume remains constant until they leave the flow field in order to cover the case, if the bubble diameter does not grow. As mentioned in section 4.3.1, the bubbles are injected from points located only in the lower half to ensure a long residence time of the bubbles in the flow domain.

Please note that only the bubble-inclusion attachment is considered here. The contact between inclusions as well as the agglomeration of inclusions are not taken into account.

The simulation time is limited to $t = 70\,\mathrm{s}$ because no further bubbles will be available in the flow field after this time.

The formation of CO bubbles at the filter surface leads to high flow velocities close to the filter. This phenomenon is similar to that shown in Figure 4.9 and Figure 4.10. Therefore, the velocity field is not shown here.

Bubble Distribution

Figure 4.20 demonstrates the distribution of CO bubbles in case of the exponential increase at $t = 10$ s after they are initialized at the filter surface. From this figure, it is clear that the bubbles, which are still small, move first downwards and follow the melt flow. As the bubble size increases significantly, the buoyancy force acting on the bubble becomes high enough to move the bubble to the top of the crucible. For the case with $d_{\mathrm{b,max}} = 500$ µm, the bubbles can rise up faster compared to the case with $d_{\mathrm{b,max}} = 100$ µm.

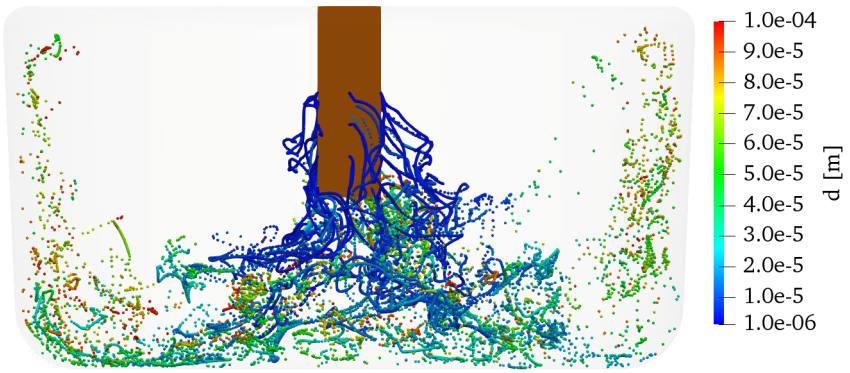

(a) $d_{\mathrm{b,max}} = 100$ µm

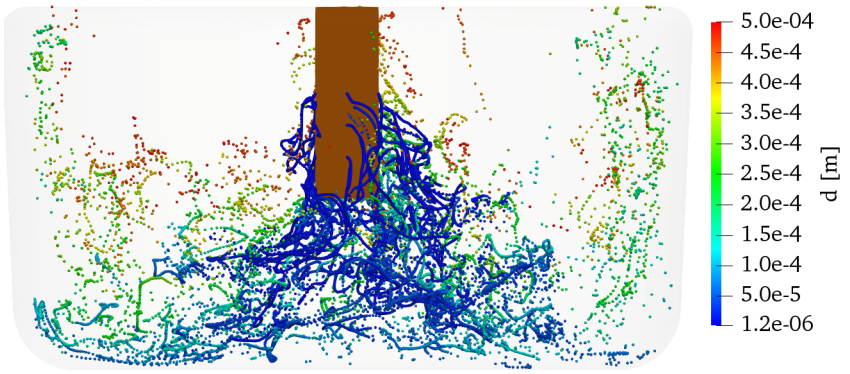

(b) $d_{\mathrm{b,max}} = 500$ µm

Figure 4.20: Bubble distribution in case of the exponential increase of bubble volume for different maximal bubble diameter at $t = 10$ s [136].

Figure 4.21 depicts the cases of the linear increase of bubble volume. The bubbles move upwards faster than in case of the exponential increase because the bubble can grow faster in this case. For $d_{\mathrm{b,max}} = 500$ µm, the bubble size increases fast. Therefore, the bubbles can not be distributed in the flow field and can rise up close to the filter, where they are created.

As can be seen, the bubble distribution is completely different in case of the linear increase with $d_{\mathrm{b,max}} = 500\,\mu\mathrm{m}$ compared to the other cases. The reason for that is the quick increase of bubble volume and the corresponding bubble diameter in this case (see Figure 4.22). This means that the buoyancy force acting on the bubbles increases extremely quickly. The distribution in the other cases is nearly similar. This may be attributed to the increase behavior of the bubble diameter as shown in Figure 4.22. At the beginning, the bubble diameter is similar in case of the exponential increase

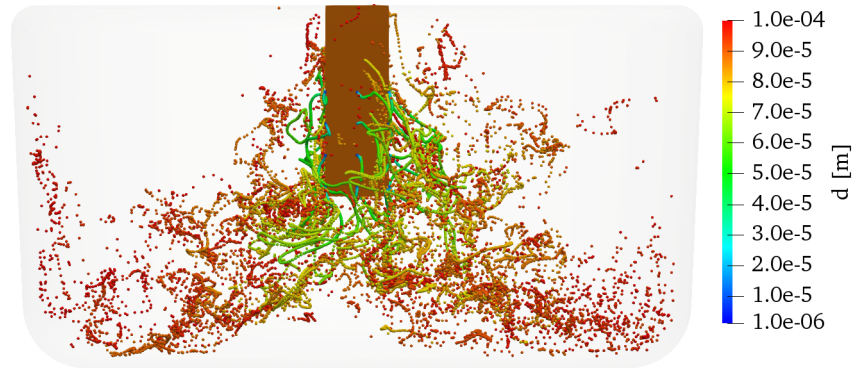

(a) $d_{\mathrm{b,max}} = 100$ µm

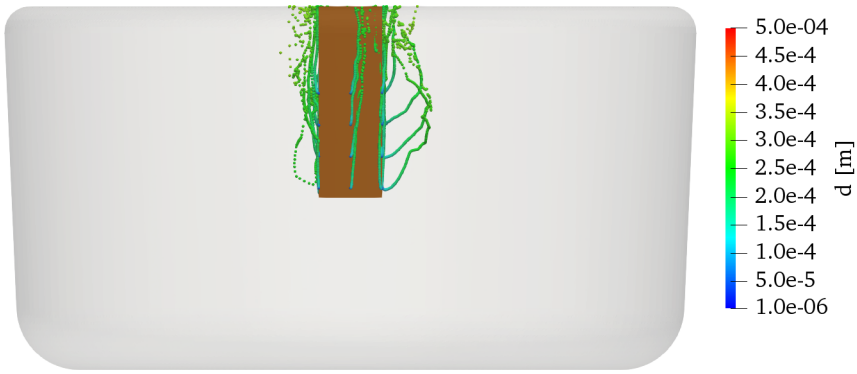

(b) $d_{\mathrm{b,max}} = 500$ µm

Figure 4.21: Bubble distribution in case of the linear increase of bubble volume for different maximal bubble diameter at $t = 10$ s [136].

of volume with $d_{\mathrm{b,max}} = 100$ µm and $d_{\mathrm{b,max}} = 500$ µm. Moreover, the diameter of a bubble is smaller in case of the exponential increase with $d_{\mathrm{b,max}} = 500$ µm than the diameter in case of linear increase with $d_{\mathrm{b,max}} = 100$ µm before $t \approx 7.2$ s. Afterwards, it is higher.

For sake of brevity, the distribution of the bubbles in case of the constant bubble volume is not shown here because the distribution of the bubbles is nearly similar to that shown in case of linear increase. The bubbles in case of $d_{\mathrm{b,max}} = 500$ µm float directly to the free surface.

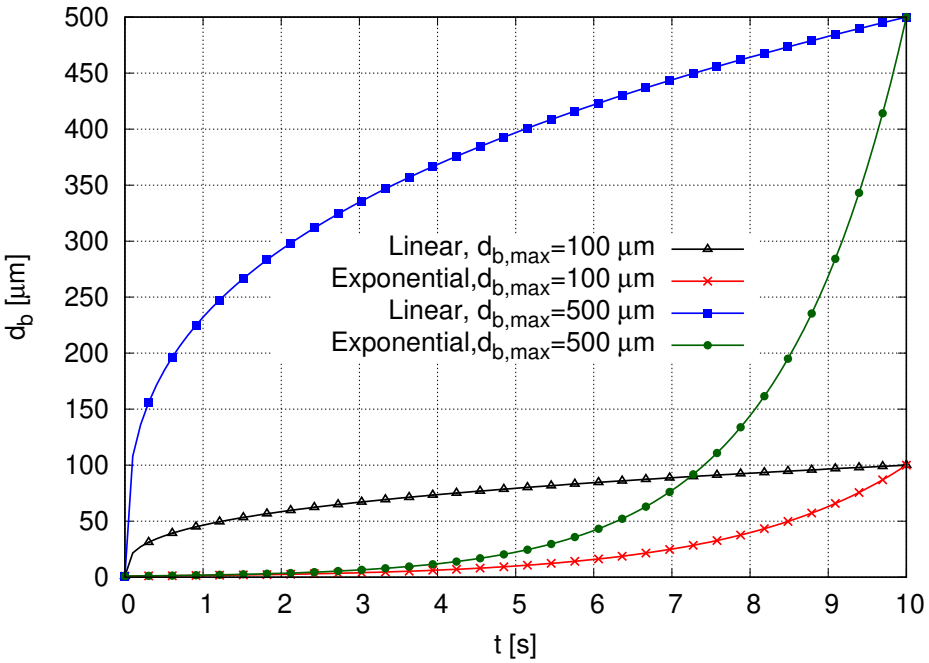

Figure 4.22: Growth behavior of the bubble diameter in case of the linear and exponential increase for $d_{\mathrm{b,max}} = 100$ µm and $d_{\mathrm{b,max}} = 500$ µm.

Cleanliness of Melt

Table 4.5 displays a comparison between the level of melt cleanliness η in case of bubble formation on filter walls (section 4.3.3) with that in case of bubble formation on inclusions (section 4.3.2). Table 4.5 shows the results for the exponential and linear increase in the bubble volume. Moreover, the results without an increase in the bubble volume can be found in this table. In case of bubble formation on the filter surface, η is determined as the ratio of the initial number of inclusions in the melt to the number of inclusions removed from the melt by the rising bubbles, generated at the filter surface. It is evident in Table 4.5 that η remains very low (about 6% at maximum) for bubble formation on the filter, whereas it is much higher in case of bubble formation on inclusions (about 29% and 61%, respectively). The level of the melt cleanliness in case of bubble formation on inclusion surface is closer to that detected in the filtration experiment conducted by Storti et al. [20]. This underlines that the main reason for high η in the experiment might be the formation of bubbles on the rough surface of inclusions.

In the assumption of bubble formation on the filter surface, the small bubbles have less contact probability with the inclusions. Moreover, the large bubbles rise fast to the free surface because of high buoyancy without capturing many inclusions. The maximum η for the case of bubble formation on the filter surface is obtained in case of exponential increase with $d_{\mathrm{b,max}} = 500$ µm at $t = 70$ s because the bubble size increases slowly compared to linear increase. This means that the bubble can stay longer in the flow field and has more contact probability with the inclusions.

Table 4.5: Comparison of the obtained level of the melt cleanliness between the investigated cases, bubble formation on the filter surface and on inclusions [136].

$t = 10$ [s]				
$d_{\mathrm{b,max}}$ [µm]	η [%]			
	On filter			On inclusions
	Linear	Exponential	Without increase	
100	0.05	< 0.01	0.14	29.0
300	0.42	0.04	0.67	
500	0.57	0.18	1.02	
$t = 70$ [s]				
$d_{\mathrm{b,max}}$ [µm]	η [%]			
	On filter			On inclusions
	Linear	Exponential	Without increase	
100	0.79	0.62	0.61	61.0
300	0.58	3.48	0.70	
500	0.65	5.76	1.05	

Summary

The previous results conclude that the bubble formation on the filter surface in case of reactive cleaning has a negligible positive effect on inclusion removal compared to the case of bubble formation on inclusions, where an increase in the level of melt cleanliness is very low. The reason for that may be either the low contact probability between bubbles and inclusions or the quick flotation of the bubbles.

4.4 Active Filtration

Besides the hypotheses of reactive cleaning, the impact of active filtration on inclusion removal is investigated briefly in this PhD thesis. In this section, the inclusions can be deposited on the filter surface according to the filtration law explained in section 3.5. The flow field is not shown here because it has the similar characterization shown later in section 4.6.

4.4.1 Simulation Setup

The filtration probability ψ is not constant and varies depending on the filtration rate and penetration depth according to the filtration's law. The calculation of ψ during the simulations is explained in more details in section 3.5. Two filters with different pore density (10 ppi and 20 ppi) are used in the simulations. Their permeability and Forchheimer-coefficient are listed in Table 4.3. ILES is adopted to describe the turbulence in ICF2. The inclusions, initialized in the simulations, has a diameter of $d_\mathrm{p} = 20$ µm. This diameter is chosen because the filtration law is developed only for this diameter of inclusions. The filter is located on the central axis of ICF2 (see Figure 4.5). The results, which are shown below, do not depend on the number of the injected inclusions and on the time step.

The same grid used in section 4.3 is employed here. The time step is set to 0.001 s. The filtration time is 300 s. The discretization schemes are listed in Table 4.2.

Filtration Efficiency

Figure 4.23a compares the filtration rate for the considered cases (10 and 20 ppi). The filtration efficiency of the complete system η is defined as the ratio of the filtered inclusions to the total number of inclusions inserted at the beginning of the simulation. The filtration efficiency of the filter η_filter is calculated as the ratio of the filtered inclusions to the total number of inclusions entering the filter. It is evident that the pore density of the filter has an impact on its performance. A higher filtration efficiency can be achieved using a filter with higher pore density (20 ppi). This finding

can be attributed to the higher filtration coefficient λ in case of 20 ppi, as can be seen in Figure 3.1. The higher efficiency can be obtained by using a filter with 20 ppi, although the mass flow rate through the filter with 10 ppi is higher than that in case of 20 ppi because of the lower κ_1 in case of 10 ppi (see Figure 4.23b).

Furthermore, a difference between η and η_{filter} can be observed. η_{filter} is considerably higher than η. The lower value of η is related to the placement of the filter, chosen in the experiment. The location of the filter allows only a small amount of the melt to flow through the filter during the filtration time (300 s), as can be deduced from Figure 4.23b.

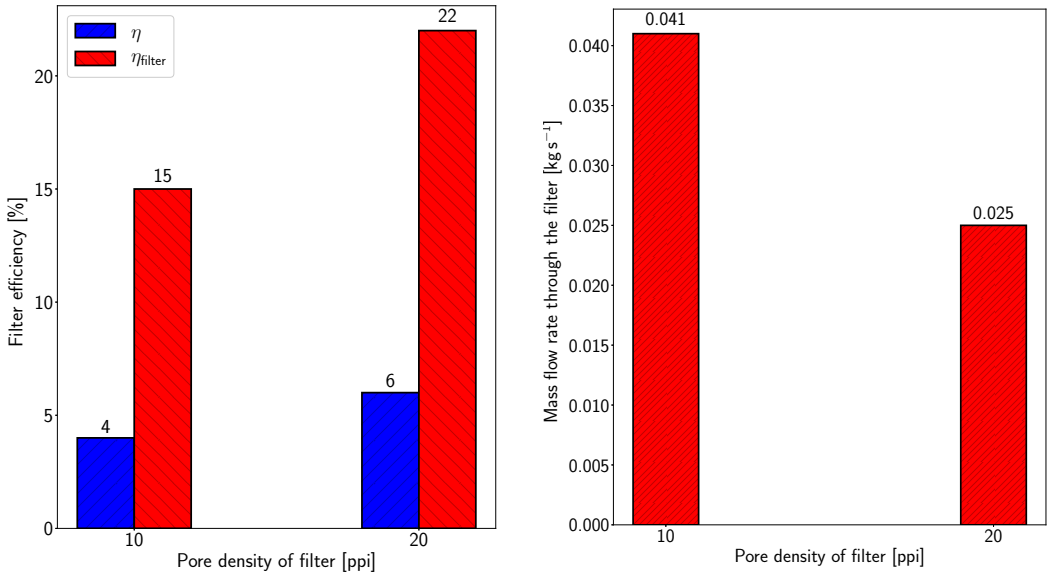

(a) **(b)**

Figure 4.23: Impact of pore density of the used filters (10 and 20 ppi) on a) the filtration efficiency of the filter η_{filter} and η and b) the mass flow rate through the filter.

Summary

Comparing the filtration efficiency with the cleaning efficiency in case of bubble formation on inclusion surface, one can conclude that the filtration efficiency is clearly lower than the cleaning efficiency in spite of the longer filtration time in case of active filtration. The low filtration efficiency is attributed to the low probability of inclusion deposition on the filter because of many reasons, e.g. the big size of filter pores compared to the inclusions diameter, which exists in the melt.

4.5 Combination of Active Filtration and Reactive Cleaning

After inspecting the three hypotheses of reactive cleaning, including bubble formation on inclusion surface as well as on the filter surface, and of active filtration separately, reactive cleaning is combined with active filtration in order to show the effect of such combination on the melt cleanliness and on the flow field in ICF2. For this purpose, different cases are investigated here. In the investigated cases, the filters act either only active or both reactive and active. As shown previously, the bubble formation on the filter surface has a negligible influence on the melt cleanliness. Therefore, the CO bubble formation on the filter is neglected in the current section. This means that the CO bubbles can form only on the inclusion surface due to the reaction between carbon and oxygen.

4.5.1 Simulation Setup

Table 4.6 summarizes the cases investigated in the section. Figure 4.24 displays the positions of the filters. In the simulations, the filters exhibit a pore density of 10 ppi. In order to simulate the flow inside the ceramic filter, the Darcy-Forchheimer's law (Equation 3.25) is adopted. The required permeability and Forchheimer coefficient of the filter are listed in Table 3.1. The filtration model, which is employed for active filtration, is described in section 3.5.

Table 4.6: Description of cases investigated in the section of combination of active filtration and reactive cleaning. Filter positions are shown in Figure 4.24.

	Position (1)	Position (2)	Position (3)
case (1)	-	active, reactive	-
case (2)	active, reactive	active	active, reactive
case (3)	active	active, reactive	active

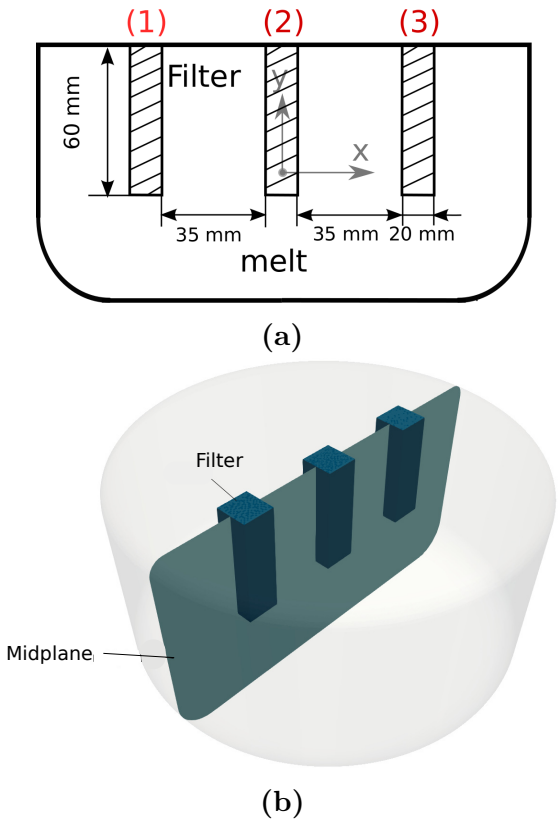

Figure 4.24: a) Schematic 2D sketch of filter positions in ICF2 and b) the flow field with the midplane used to illustrate the velocity and the concentration field in case of the combination between reactive cleaning and active filtration.

The filters act active in all investigated cases for 300 s, whereas the filters can act reactive only for the first ten seconds. This means that carbon can be dissolved from the filter only during this time interval (10 s). Please note that the magnetic field is enabled for the whole simulation time (300 s), which means that the Lorentz force can drive the melt in ICF2 for this time interval in contrast to the case investigated in section 4.3, where the magnetic field acts only for 10 s. The concentration in the filter region is assumed to be constant and equal to $c = 1\ \mathrm{mol\,m^{-3}}$ during the reactive phase of the filter (10 s).

The same grid of ICF2 used in section 4.2 is utilized in the following simulations. The number and initial properties of the inclusions are similar to that in section 4.3 as well. To predict the turbulent melt flow in ICF2, ILES is employed. The discretization schemes are listed in Table 4.2. The time step is set to $\Delta t = 0.001$ s and the flow field is averaged over 300 s.

Time-Averaged Flow Field

Figure 4.25 presents the time-averaged flow field in the vertical midplane and in the horizontal plane at $y = 0$ for case (1), case (2) and case (3). As mentioned previously, the Lorentz force drives the melt for 300 s in ICF2 and the velocity field is averaged over this time interval. Comparing the investigated cases, it is distinct that the flow field is considerably influenced by the position and the number of used filters. In all cases, the torodial vortices are still dominant in the flow field as can be seen in the vertical midplanes. However, the toroidal vortices are compressed in the region between the filter and crucible walls in case (2) and case (3). In contrast to the time-averaged velocity field in Figure 4.9, the velocity is low close to the filter because the CO bubbles form only in the first ten seconds as the filters act both reactive and active. This means that their effect is damped out owing to long time-averaging after disabling the reactive effect of the filter.

Comparing the velocity field in case (2) and case (3), it is evident that slight differences can still be observed in the vertical and horizontal plane, although the both cases have the same operating conditions over approximately 290 s. This might be attributed to the fact that the effect of CO bubbles, which form only in the reactive phase of the

filter, on the flow field is still dominant in spite of the long time-averaging with the same operating conditions. It is expected that these differences in the time-averaged velocity field will disappear if it is time-averaged over a longer time period.

Carbon Concentration

Figure 4.26 compares the concentration field of carbon for the investigated cases in the vertical midplane and in the horizontal plane at $y = 0$ (see Figure 4.24). The concentration field is completely different comparing the investigated cases. As expected, carbon is more distributed in case (2) because carbon is dissolved from two reactive filters located at positions (1) and (3). In case (2), it is evident that carbon can not be transported in the central region of the filter in the shown midplane, where the filter is located. In case (3), carbon, which is dissolved from the reactive filter at position (2), can not reach the side region in the shown midplane. This has a negative effect on the reaction and bubble formation at inclusion surface in the side region of the crucible.

Melt Cleanliness

Figure 4.27 depicts the increase of melt cleanliness, which is represented by η, during the simulation, which results only from reactive cleaning and the CO bubble formation. The inclusions, which are removed by the filter, are not considered in the figure. η is calculated similar to section 4.3.2. As can be seen in the figure, the number of the removed inclusions is obviously higher in case (2) compared to cases (1) and (3). In case (2), carbon can be better distributed due to the two reactive filters, which means that the reaction can occur in more regions in the flow field. The difference in η between case (1) and case (3) is not huge because one reactive filter is inserted in the melt in both cases. However, it is shown that η in case (1) is higher than in case (3). The reason for this difference is that the two active filters prevent carbon to be transported in the side regions as can be seen in Figure 4.26c, which decreases the possibility of the bubble formation on inclusions in the side regions.

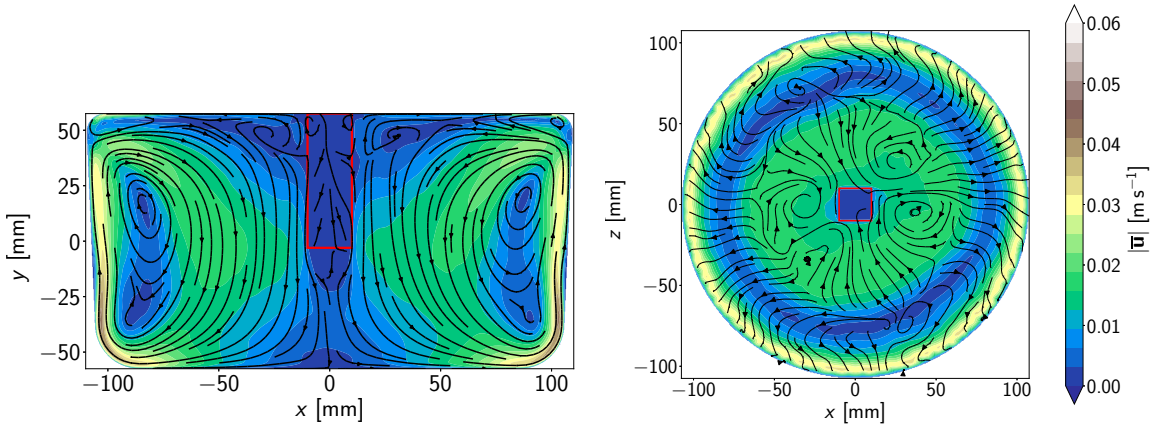

(a) Case (1)

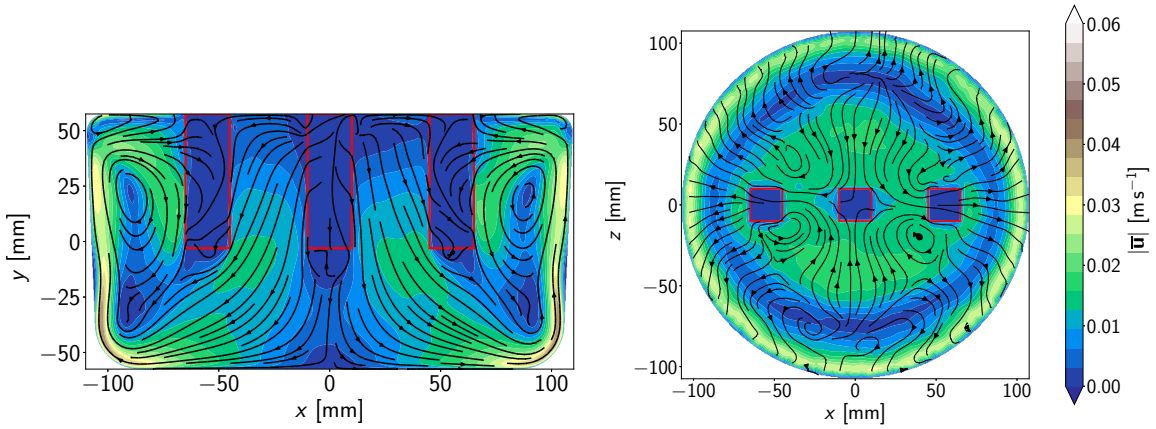

(b) Case (2)

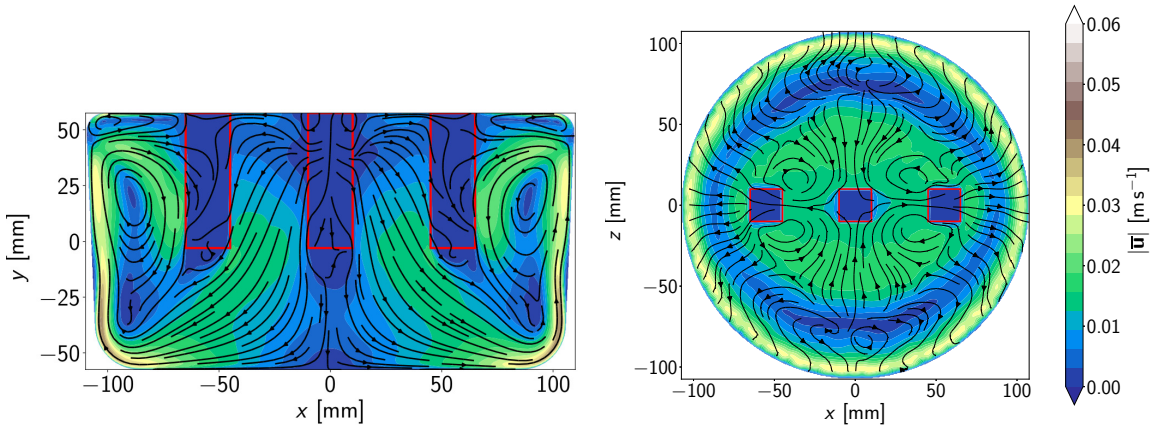

(c) Case (3)

Figure 4.25: Magnitude of the time-averaged flow field of the melt in the vertical midplane of the induction crucible furnace (ICF2) (left) and in the horizontal plane (y= 0) (right) for case (1) and case (2) and case (3)(see Table 4.6). The red rectangles represent the location of the filters.

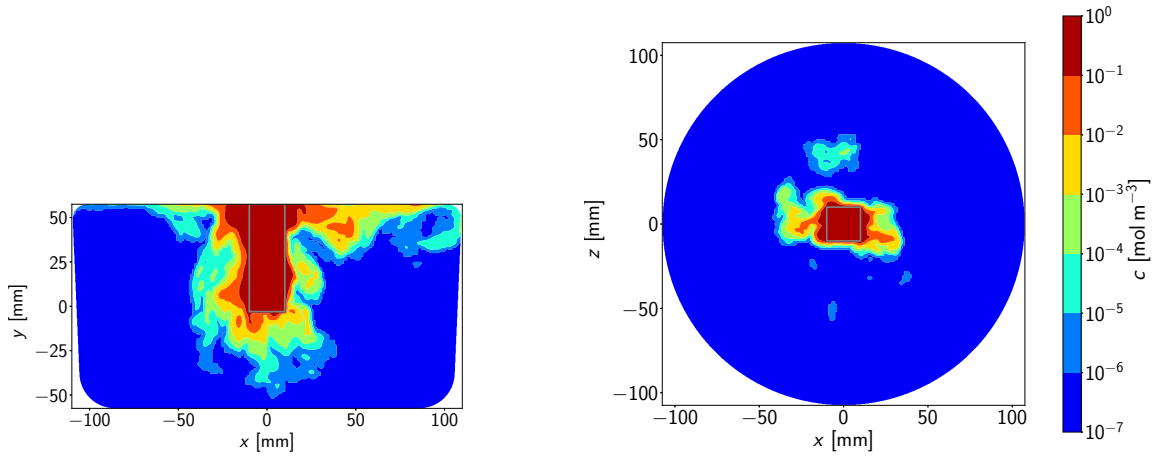

(a) Case (1)

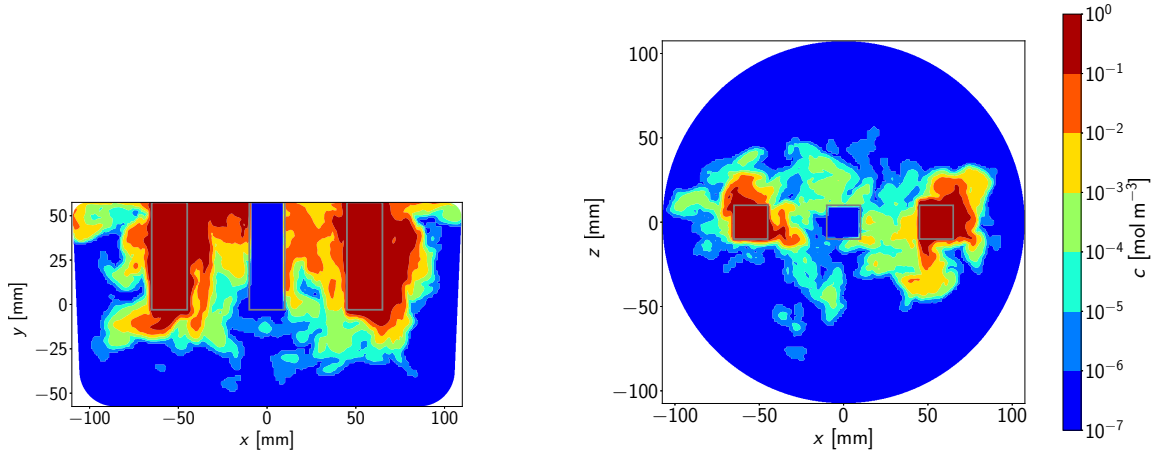

(b) Case (2)

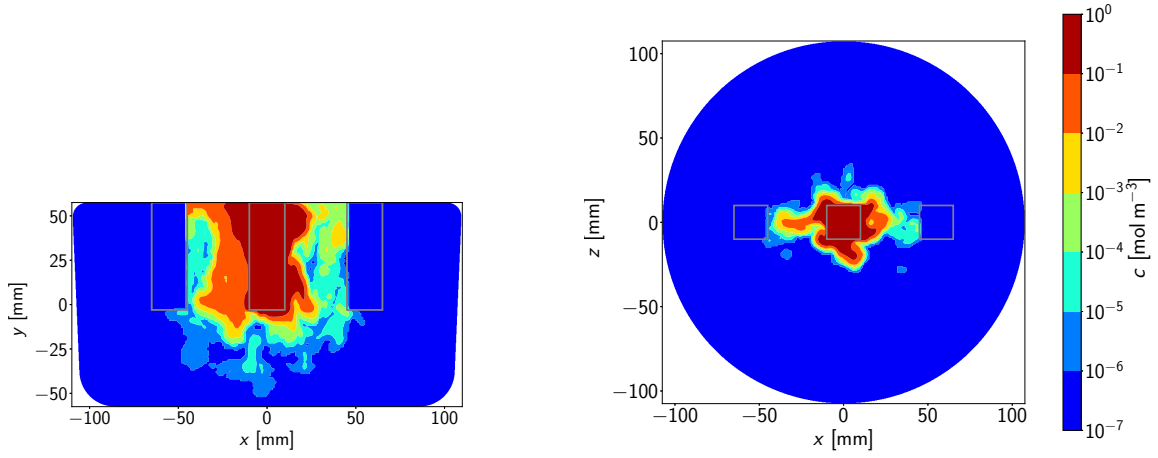

(c) Case (3)

Figure 4.26: Concentration of carbon in the vertical midplane of the induction crucible furnace (ICF2) and in the horizontal plane ($y = 0$) at time t= 10 s for the investigated cases (see Table 4.6).

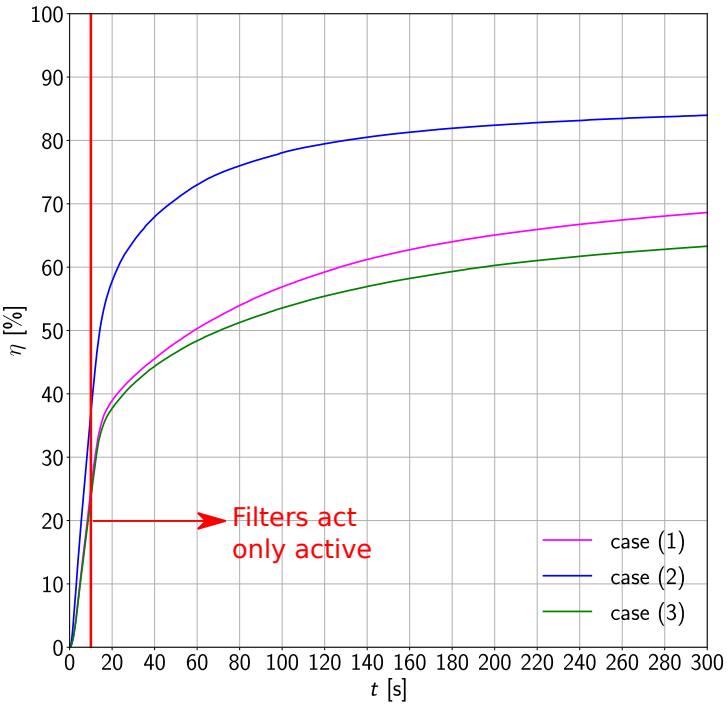

Figure 4.27: Increase of steel cleanliness during simulation time due to reactive cleaning of the steel melt in case of the combination between active filtration and reactive cleaning in ICF2 (see Table 4.6).

In Figure 4.28, the ratio of inclusions removed by the active filters to the initial number of inclusions is compared with the ratio of the removed inclusions due to reactive cleaning of the melt. One can easily notice that the ratio of the removed inclusions in case of reactive cleaning is much higher than the ratio resulting from active filtration, although the time of active filtration is longer than the time of reactive cleaning. This finding proves again that the huge difference between the experiment conducted by Storti et al. [20] and the simulations of pure active filtration in ICF2 performed by Asad et al. [115] might be attributed to the formation of CO bubbles on inclusions.

Summary

The previous section discusses the combined effect of active filtration and reactive cleaning. From the results, one can conclude that reactive cleaning dominates active filtration. In all cases, the number of the removed inclusions in case of reactive

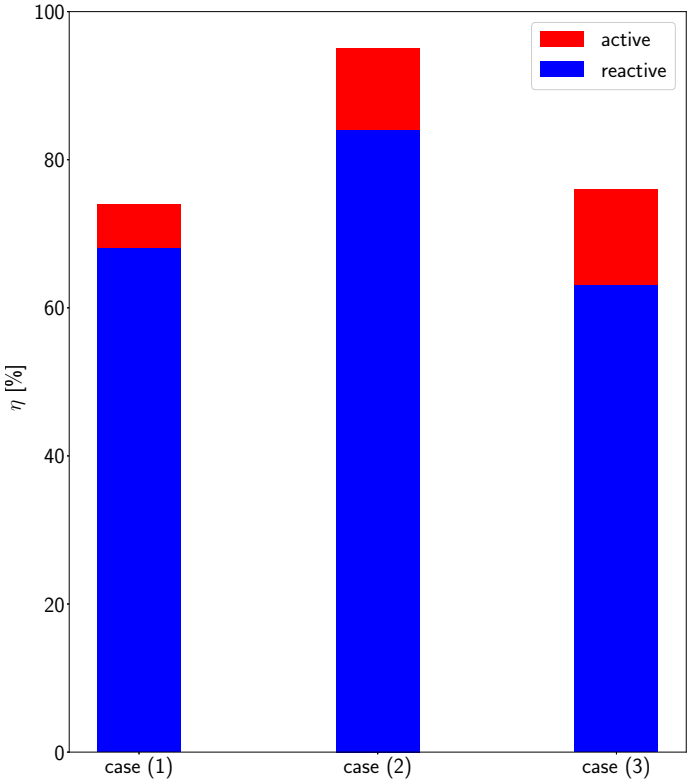

Figure 4.28: Ratio of the number of inclusions, which are removed from the melt due to active filtration and reactive cleaning, to the initial number of inclusions inserted in the flow field at the beginning of the simulation (see Table 4.6).

cleaning is much higher than that in case of active filtration. Furthermore, it can be summarized that increasing the number of the reactive filters enhances significantly inclusion removal and the corresponding level of melt cleanliness. On the contrary, an increasing number of active filters can reduce the positive effect of reactive cleaning on inclusion removal. The active filters can prevent carbon to be well distributed in the flow domain. Therefore, filter positions have to be properly chosen in the ICF.

4.6 Effect of Turbulence Modeling

In this section, the effect of turbulence modeling on the flow field and inclusion transport in ICF2 is highlighted. Moreover, the influence of the DRW dispersion model on the inclusion behavior is discussed. Reactive cleaning and active filtration are not considered here. Partial results of the current section have already been published in Asad et al. [147].

4.6.1 Simulation Setup

To determine the effect of turbulence modeling on the prediction of the melt flow and inclusion transport, the turbulent melt flow in ICF2 is simulated either by the SST $k-\omega$ turbulence model in case of URANS simulation, the SST $k-\omega$ SAS turbulence model for the RANS-LES hybrid simulation, ILES or WALE subgrid turbulence model for LES simulations. The turbulence models are explained in more details in a previous section (see section 3.3.1). The number of inclusions injected in the flow field is $2 \cdot 10^6$ and they have a constant diameter of $d_\mathrm{p} = 20$ µm. The time step is set to be 0.001 s. The flow field is averaged over 300 s. The discretization schemes, which are adopted in the following simulations, are listed in Table 4.2. The computational grid is identical to the grid of ICF2 used in section 4.2.

Time-averaged Flow Field

Figure 4.29 compares the time-averaged flow field for different simulations. It is evident that the time-averaged flow patterns are similar for all simulations. The flow patterns are dominated mainly by toroidal vortices in all cases. The only noticeable difference between the time-averaged flow fields is that a small recirculating flow region is present at the lower edge of the filter in case of LES simulations (WALE and ILES) and SST $k-\omega$ SAS, while it does not exist in case of the SST $k-\omega$ turbulence model.

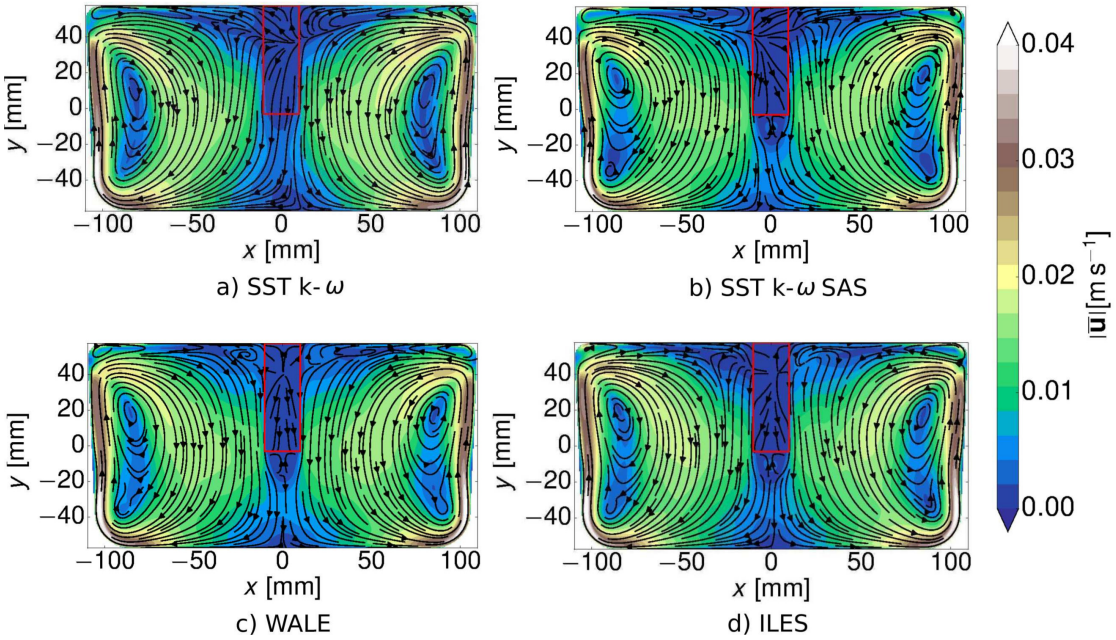

Figure 4.29: Magnitude of time-averaged velocity field and streamlines of the melt flow in the vertical midplane of the induction crucible furnace. The red rectangle represents the position of the ceramic filter [147].

Instantaneous Flow Field

Figure 4.30 depicts the instantaneous velocity field of the melt flow for the conducted simulations. Here, the main difference between SST $k-\omega$ simulation and other simulations can clearly be observed. The small turbulent scales are damped out in case of SST $k-\omega$ simulation and only the large scales are present. This is not ideal for describing the heat and mass transfer in the ICF. The SST $k-\omega$ SAS simulation shows a transition between SST $k-\omega$ and LES simulations, where more unsteadiness can be observed compared to SST $k-\omega$ simulation. However, only ILES and WALE simulations are able to also resolve smaller turbulent scales in the flow. These scales are known to be responsible for the heat and mass transfer in the ICF.

Turbulent Kinetic Energy

The resolved turbulent kinetic energy k of the flow field can be seen in Figure 4.31. k is estimated employing Equation (4.1). Due to axisymmetric distribution of k in the

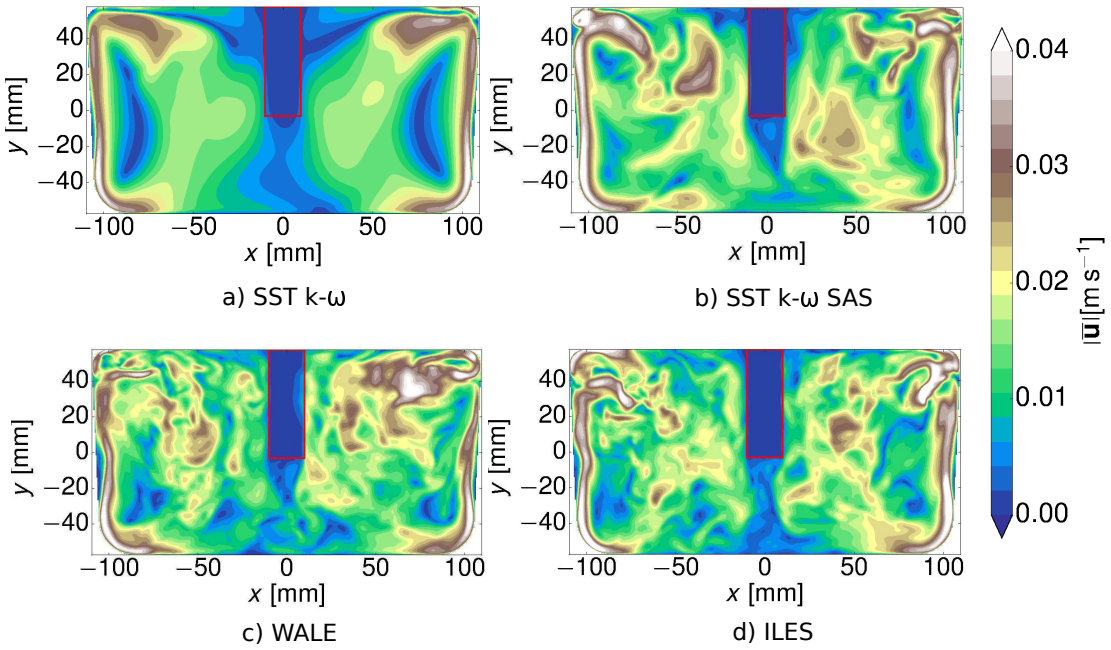

Figure 4.30: Instantaneous velocity field of the melt flow in the vertical midplane of the induction crucible furnace. The red rectangle represents the position of the filter [147].

simulations, only one half of ICF2 is presented in Figure 4.31. This figure indicates that k is maximal in the region, where the upper vortex is located (upper corner of the flow field). For all simulations, k is low in the filter region. However, it is observed that k is lower in case of SST $k-\omega$ compared to SST $k-\omega$ SAS and LES simulations. Furthermore, the turbulent kinetic energy spreads from the upper corner to the core region of the melt more in case of SST $k-\omega$ SAS and LES simulations compared to URANS simulation. This can enhance the mixing and mass transfer in the melt through the turbulent motion of the flow. A small difference of the distribution of k between LES simulations and SST $k-\omega$ SAS can be noticed in Figure 4.31.

Energy Spectrum

The smoothed energy spectrum at three points (see Figure 4.5) for all simulations is shown in Figure 4.32. It is clear from this figure that energy spectrum exhibits the inertial subrange ($f^{-5/3}$) and the range of energy dissipation (f^{-3}), which are typical for fully turbulent flow [148]. They are still present in spite of the effect of

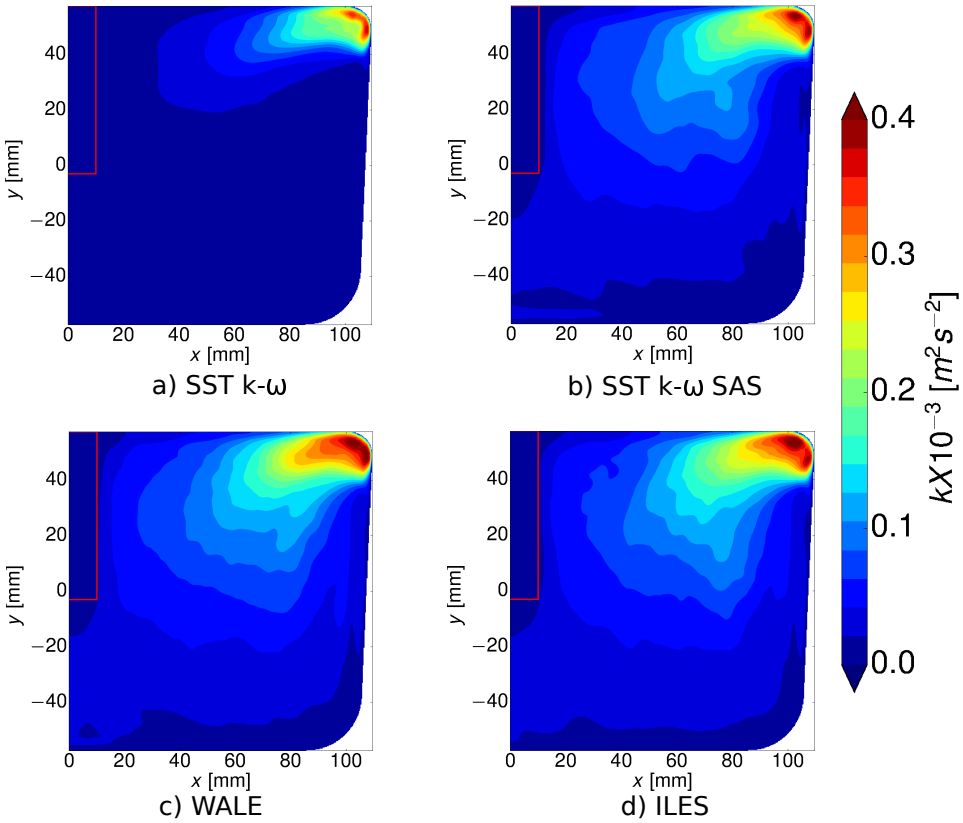

Figure 4.31: The time-averaged resolved turbulent kinetic energy k. The red rectangle represents the location of the filter [147].

the magnetic field. However, the range of the inertial subrange is smaller at point P3 compared to the other points. Moreover, it is obvious that the energy spectrum lays higher in case of LES simulations and SST $k-\omega$ SAS at all chosen points, which implies that the system has higher energy in these cases. That may account for the better mixing of inclusions in LES simulation, as can be seen later. Moreover, it is found that the energy spectrum in case of LES simulations has a nearly similar behavior at all points. The energy spectrum in case of SST $k-\omega$ drops earlier to show the dissipation range at all points, which means that less scales of the flow are resolved. The point P1 is located in the region with high turbulent energy. Therefore, the energy spectrum at this point is located over the energy spectrum at points P2, P3. The inconsistent drop of the energy spectrum at point P1 may be attributed to an error in the smoothing process of the spectrum.

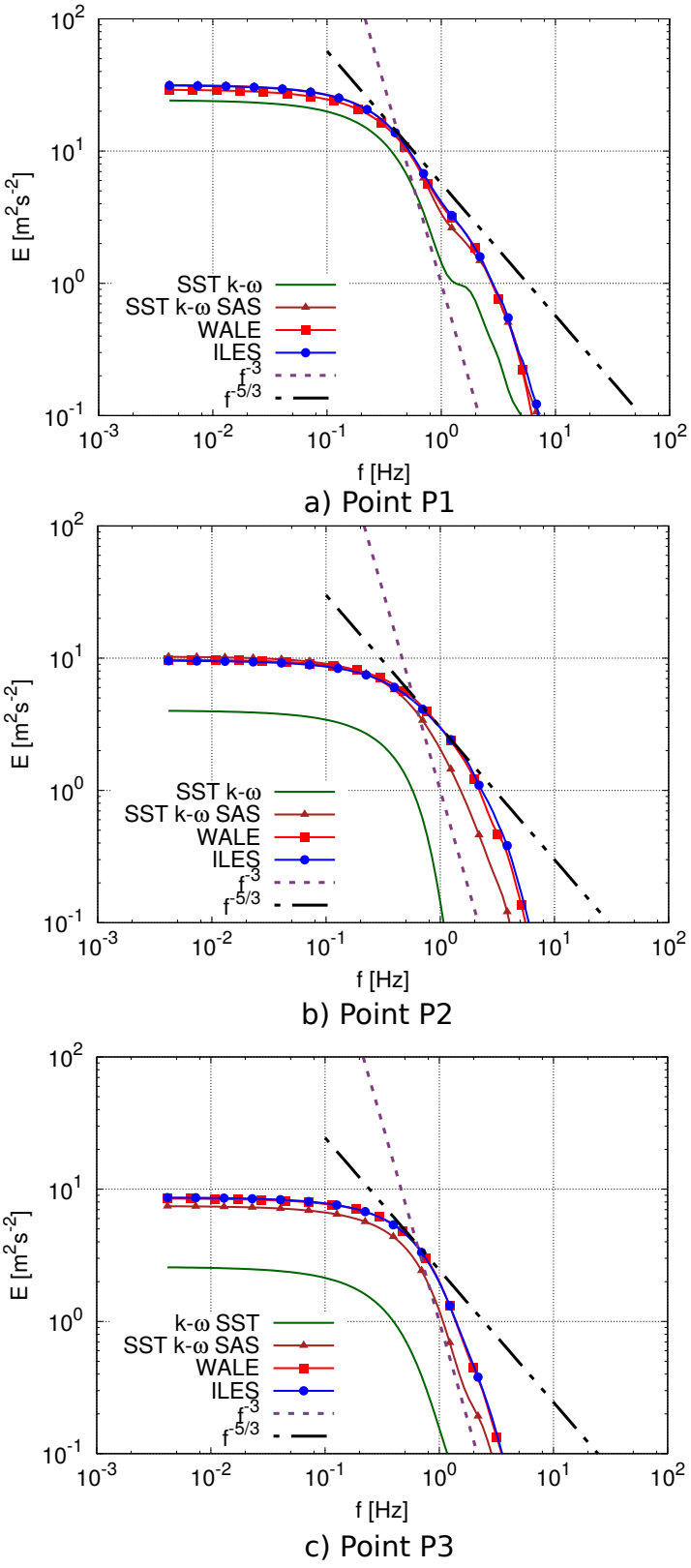

Figure 4.32: Energy spectrum of the melt flow at three different points. The location of the points can be seen in Figure 4.5.

Inclusion Distribution

Figure 4.33 presents the time-averaged void fraction of the inclusions α_p. From this figure, the considerable effect of the DRW model and turbulence modeling on the inclusion dispersion in the melt can be seen. If the DRW model is adopted in case of SST $k-\omega$ simulation, it can be noticed that the inclusions are accumulated in the central region of the dominated lower vortex and close to the bottom of the crucible. Moreover, the void fraction of inclusions is high in the filter region. This means that the inclusions stay for a long time in the filter. This finding may point out that using the DRW model may cause a wrong behavior of inclusions in the low-velocity region, in which the turbulent kinetic energy is relatively low. On the contrary, the inclusions are almost homogeneously dispersed in case of SST $k-\omega$ without using the DRW model. Additionally, it is evident that α_p has low values inside and beneath the filter. The inclusions are distributed consistently in case of SST $k-\omega$ SAS simulations in the melt either with or without using the DRW model. However, α_p is high inside the filter in case of using the DRW model. This implies that the inclusions exhibits relatively high residence time in the filter. The results differ significantly in case of LES simulations compared to those of SST $k-\omega$. Here, α_p is low in the filter. Moreover, the inclusions are dispersed well in the flow field. The results of ILES and WALE simulations are similar.

The inclusions experience fluctuating velocity $\boldsymbol{u}'$ because of turbulence. The magnitude of $\boldsymbol{u}'$ is plotted in Figure 4.34 over time (30 s) at points P2, P3 (see Figure 4.5) for SST $k-\omega$ and WALE simulations. $\boldsymbol{u}'$ in case of ILES shows similar behavior to $\boldsymbol{u}'$ in case of WALE. Therefore, it is not shown here. As can be seen previously, there is a main difference in the distribution of inclusions between URANS simulation using the DRW model and LES simulations. This difference can be attributed to $\boldsymbol{u}'$ acting on the inclusions in the simulations. The inclusions experience a constant $\boldsymbol{u}'$ over the lifetime of an eddy in case of SST $k-\omega$ due to the used DRW model. On the other hand, $\boldsymbol{u}'$ varies continuously at each time step in case of LES simulations. This provides a better dispersion of the inclusions in this case.

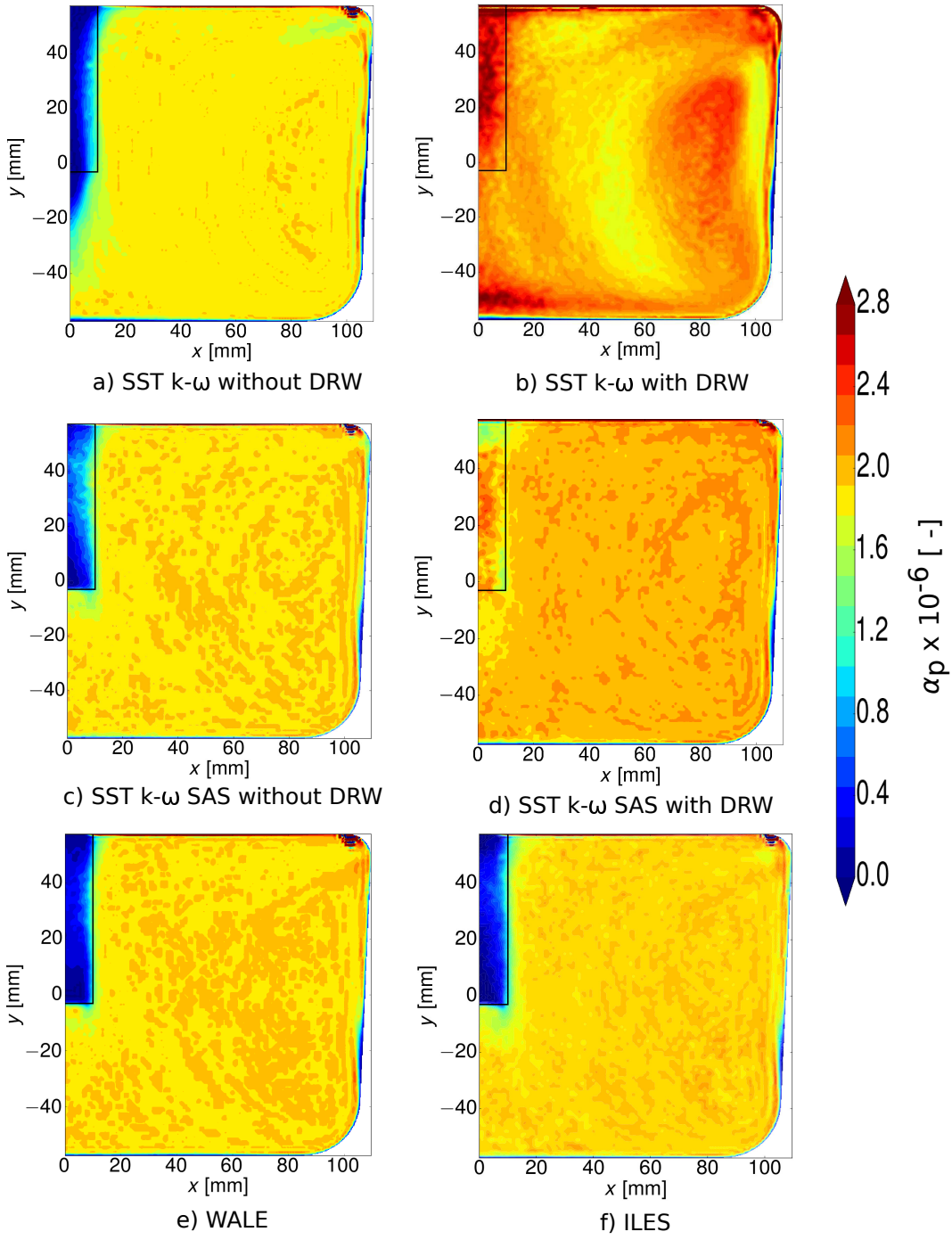

Figure 4.33: Time-averaged field of the void fraction of inclusions α_p in axisymmetrical section of ICF2. The black rectangle represents the location of the ceramic filter [147].

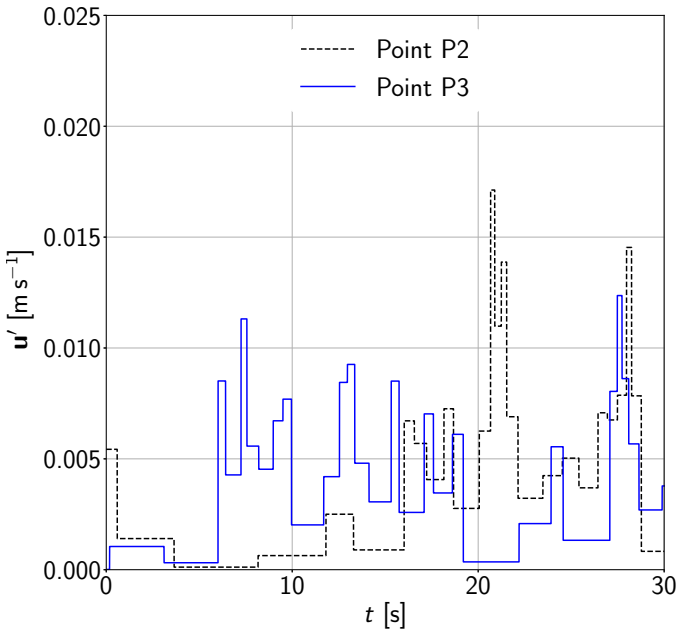

(a) SST $k - \omega$

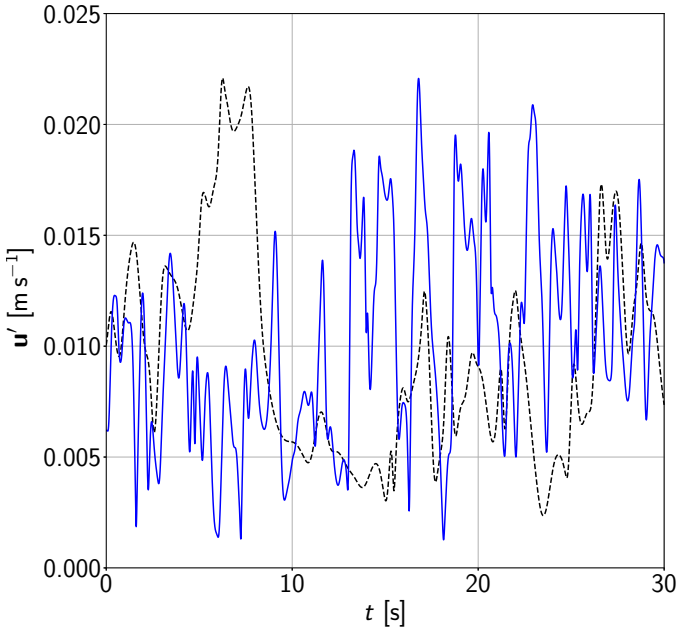

(b) WALE

Figure 4.34: Comparison between the magnitude of the fluctuating velocity $\boldsymbol{u}'$ acting on the inclusions in case of SST $k - \omega$ and WALE [147].

Summary

The results of this section indicate that the choice of the turbulence model plays a significant role in predicting the recirculating turbulent melt flow and inclusion transport. LES simulations show good performance to predict the turbulent flow and inclusion behavior in the turbulent flow. On the contrary, the results of the URANS simulations coupled with the DRW model show a possible wrong behavior of inclusions in a turbulent flow caused by the DRW Model. Therefore, it is advised to perform LES simulations to predict inclusion transport in an acceptable accuracy.

5 Summary and Conclusion

This thesis dealt mainly with reactive cleaning and active filtration of the steel melt using ceramic foam filters, which have been developed in CRC 920. These filters are immersed in the steel melt in order to remove the inclusions moving in the melt.

A new water model experiment was presented in the thesis. The water model was created to mimic the turbulent recirculating flow in the induction crucible furnace and to examine the capability of the turbulence models to predict the recirculating flow. The results showed that the water model could produce similar toroidal vortices to that taking place in the induction furnace. Moreover, the turbulence models were able to predict the recirculating turbulent flow.

The PhD thesis focused on reactive cleaning of the steel melt, which has not been investigated in details in literature so far. In reactive cleaning, a carbon-bonded ceramic foam filter is immersed in the melt. Then, carbon can be dissolved in the melt and react directly with oxygen either on the surface of the filter or on inclusion surface. As a consequence of this reaction, carbon monoxide bubbles can form. Besides reactive cleaning, active filtration was investigated shortly to compare its effect on inclusion removal with reactive cleaning. In active filtration, the inclusions are removed only by the ceramic foam filter. To investigate reactive cleaning and active filtration, a corresponding numerical model was developed in OpenFOAM to investigate the turbulent, reactive multiphase melt flow in the induction crucible furnace in these cases. The magnetohydrodynamic melt flow in the induction crucible furnace was validated using experimental data from literature. The numerical model could predict the melt flow in the induction crucible furnace to a good extent. At the beginning, reactive cleaning and active filtration were investigated separately. The results showed that reactive cleaning improved the cleanliness of the melt significantly in case of

bubble formation on inclusion surface. The bubble could grow fast on the inclusion, increasing significantly the buoyancy of the bubble-inclusion aggregate. Then, the inclusion could float up fast to the slag layer (free surface). On the contrary, the bubble formation on filter surface did not increase the cleanliness level of melt significantly. Moreover, the filtration rate in case of active filtration was very low compared to the cleaning efficiency in case of reactive cleaning in spite of the long filtration time.

Furthermore, the combination between reactive cleaning and active filtration in the induction crucible furnace was investigated in this PhD thesis. The number of inclusions removed by reactive cleaning was much higher in the whole investigated cases compared to the number of inclusions removed by active filtration of the melt. Furthermore, the results revealed the considerable effect of the position and the number of used filters on the flow field and the concentration distribution as well.

Beside investigating reactive cleaning and active filtration, the effect of turbulence modeling on the prediction of the flow field and inclusion dispersion in the induction crucible furnace was investigated. From the results, it was obvious that the characterization of the flow field depended considerably on the turbulence modeling. Furthermore, this investigation indicated that using the random walk dispersion model was not able to describe the inclusion distribution in a turbulent recirculating flow and turbulent velocity fluctuations, which inclusions experienced in a turbulent flow.

The numerical models, which were developed and implemented in OpenFOAM, can be employed as well to investigate active filtration and reactive cleaning in other equipment in continuous casting, e.g. tundish.

6 Outlook

This PhD thesis offered good understanding about reactive cleaning and active filtration in the induction crucible furnace. However, there are still some open issues, which have to be clarified in order to enhance the numerical models and the solvers used in this PhD thesis. The following points summarize these issues, which have to be handled in future works:

- The agglomeration of inclusions has to be considered in the numerical model. The small inclusions can agglomerate and create inclusions clusters. This enhances the inclusions flotation to the free surface of the melt (slag layer).
- New models have to be developed and adopted in order to consider bubble-inclusions attachment depending on the flow conditions.
- The numerical model has to be extended to consider the coalescence of carbon monoxide bubbles. If the coalescence of bubbles with attached inclusions takes place, a model has to be developed to take into account the detachment of the inclusions.
- In this thesis, a drag model of a solid spherical particle was adopted for the bubble-inclusion aggregate. In order to enhance the prediction of aggregate behavior in the melt, a new drag model has to be implemented.
- In order to detect the exact size of carbon monoxide bubbles and the decrease of carbon concentration in the filter, other elements, e.g. Aluminum, have to be considered in the reaction taking place on the filter or on the inclusion. For this purpose, OpenFOAM has to be coupled with thermodynamic databases to consider this reaction in more details.

Bibliography

[1] L. Zhang and B. G. Thomas. "State of the Art in Evaluation and Control of Steel Cleanliness". In: *ISIJ International* 43.3 (2003), pp. 271–291. DOI: 10.2355/isijinternational.43.271.

[2] L. Zhang and Y. Wang. "Modeling the Entrapment of Nonmetallic Inclusions in Steel Continuous-Casting Billets". In: *JOM* 64.9 (2012), pp. 1063–1074. DOI: 10.1007/s11837-012-0421-2.

[3] R. A. Olson and L. C. B. Martins. "Cellular Ceramics in Metal Filtration". In: *Advanced Engineering Materials* 7.4 (2005), pp. 187–192. DOI: 10.1002/adem.200500021.

[4] S. Dudczig et al. "Application of Oxide Coatings for Improved Steel Filtration with the Aid of a Metal Casting Simulator". In: *Advanced Engineering Materials* 15.12 (2013), pp. 1177–1187. DOI: 10.1002/adem.201300121.

[5] C. G. Aneziris et al. "Alumina Coatings on Carbon Bonded Alumina Nozzles for Active Filtration of Steel Melts". In: *Ceramics International* 39.3 (2013), pp. 2835–2843. DOI: 10.1016/j.ceramint.2012.09.055.

[6] S. Dudczig et al. "Characterization of Carbon-bonded Alumina Filters with Active or Reactive Coatings in a Steel Casting Simulator". In: *Ceramics International* (2014). DOI: 10.1016/j.ceramint.2014.08.038.

[7] Y. Sahai and T. Emi. *Tundish Technology for Clean Steel Production*. World Scientific, 2008. ISBN: 978-9812706218.

[8] Y. Sahai. "Tundish Technology for Casting Clean Steel: A Review". In: *Metallurgical and Materials Transactions B* 47.4 (2016), pp. 2095–2106. DOI: 10.1007/s11663-016-0648-3.

[9] W. Yang et al. “Nucleation, Growth, and Aggregation of Alumina Inclusions in Steel”. In: *JOM* 65.9 (2013), pp. 1173–1180. DOI: 10.1007/s11837-013-0687-z.

[10] R. Dekkers et al. “Crystal Growth in Liquid Steel During Secondary Metallurgy”. In: *Metallurgical and Materials Transactions B* 34.2 (2003), pp. 161–171. DOI: 10.1007/s11663-003-0003-3.

[11] G. F. Vander Voort. *Metallography, Principles and Practice*. McGraw-Hill Mechanical Engineering. McGraw-Hill, 1984. ISBN: 978-0070669703.

[12] E. Koch et al. “Verbesserung des Makroreinheitsgrades beim Brammenstrangguss”. In: *Berg and Huttenmännische Monatshefte* 143 (1998), pp. 338–344.

[13] H. Ling et al. “Mathematical Modeling on the Growth and Removal of Nonmetallic Inclusions in the Molten Steel in a Two-Strand Continuous Casting Tundish”. In: *Metallurgical and Materials Transactions B* 47.5 (2016), pp. 2991–3012. DOI: 10.1007/s11663-016-0743-5.

[14] L. Zhang. “Nucleation, Growth, Transport, and Entrapment of Inclusions During Steel Casting”. In: *JOM* 65.9 (2013), pp. 1138–1144. DOI: 10.1007/s11837-013-0688-y.

[15] M. Haustein et al. “Collision of Micro-sized Non-metallic Inclusions in Liquid Steel Flows: A Computational Study”. In: *JOM* 70.12 (2018), pp. 2943–2949. DOI: 10.1007/s11837-018-3113-8.

[16] K. Higashitani et al. “Kinetic Theory of Shear Coagulation For Particles in a Viscous Fluid”. In: *Journal of Chemical Engineering of Japan* 15.4 (1982), pp. 299–304. DOI: 10.1252/jcej.15.299.

[17] J. Gleinig et al. “Characterization of Nonmetallic Inclusions in 18CrNiMo7-6”. In: *Metallurgical and Materials Transactions B* 50.1 (2019), pp. 337–356. DOI: 10.1007/s11663-018-1431-4.

[18] C. Schröder et al. “Interactions between Exogenous Magnesia Inclusions with Endogenous Inclusions in a High Alloyed Steel Melt”. In: *Advanced Engineering Materials* 19.9 (2017), p. 1700146. DOI: 10.1002/adem.201700146.

[19] M. Seleznev et al. “Cluster Detection of Non-Metallic Inclusions in 42CrMo4 Steel”. In: *Steel Research International* 89.11 (2018), p. 1800216. DOI: 10.1002/srin.201800216.

[20] E. Storti et al. “Filter Functionalization with Carbon Nanotubes and Alumina Nanosheets for Advanced Steel Filtration”. In: *Steel Research International* 88.10 (2017), p. 1700142. DOI: 10.1002/srin.201700142.

[21] Q. Yuan and B.G. Thomas. “Transport and Entrapment of Particles in Continuous Casting of Steel”. In: *ICS 2005 - Proceedings of the 3rd International Congress on the Science and Technology of Steelmaking*. 2005, pp. 745–759.

[22] K. Morales-Higa et al. “Ladle Shroud as a Flow Control Device for Tundish Operations”. In: *Metallurgical and Materials Transactions B* 44.1 (2013), pp. 63–79. DOI: 10.1007/s11663-012-9753-0.

[23] H. Yang et al. “Modeling of Argon Gas Behavior in Continuous Casting of Steel”. In: *CFD Modeling and Simulation in Materials Processing 2018*. Cham: Springer International Publishing, 2018, pp. 119–131.

[24] Y. Xu et al. “A Numerical Study about the Influence of a Bubble Wake Flow on the Removal of Inclusions”. In: *ISIJ International* 56.11 (2016), pp. 1982–1988. DOI: 10.2355/isijinternational.ISIJINT-2016-249.

[25] W. Lou and M. Zhu. “Numerical Simulations of Inclusion Behavior in Gas-Stirred Ladles”. In: *Metallurgical and Materials Transactions B* 44.3 (2013), pp. 762–782. DOI: 10.1007/s11663-013-9802-3.

[26] L. Zhang et al. “Inclusion Removal by Bubble Flotation in a Continuous Casting Mold”. In: *Metallurgical and Materials Transactions B* 37.3 (2006), pp. 361–379. DOI: 10.1007/s11663-006-0021-z.

[27] L. Zhang et al. “Large Inclusions in Plain-carbon Steel Ingots Cast by Bottom Teeming”. In: *ISIJ International* 46.5 (2006), pp. 670–679. DOI: 10.2355/isijinternational.46.670.

[28] Y. Miki and S. Takeuchi. “Internal Defects of Continuous Casting Slabs Caused by Asymmetric Unbalanced Steel Flow in Mold”. In: *ISIJ International* 43.10 (2003), pp. 1548–1555. DOI: 10.2355/isijinternational.43.1548.

[29] F. C. Campbell. *Metals Fabrication: Understanding the Basics*. ASM International, 2013. ISBN: 978-1627080187.

[30] P. L. Jones et al. "Electroheat and Materials Processing". In: *Electrical Engineer's Reference Book*. Oxford: Newnes, 2003, pp. 1 –38. ISBN: 978-0750646376.

[31] M. Kirpo. "Modeling of Turbulence Properties and Particle Transport in Recirculated Flows". PhD thesis. University of Latvia, 2009.

[32] A. Asad et al. "Numerical Study of Particle Filtration in an Induction Crucible Furnace". In: *International Journal of Heat and Fluid Flow* 62 (2016), pp. 299 –312. DOI: j.ijheatfluidflow.2016.10.002.

[33] E. Baake et al. "Extension of the k-ε Model for the Numerical Simulation of the Melt Flow in Induction Crucible Furnaces". In: *Metallurgical and Materials Transactions B* 26.3 (1995), pp. 529–536. DOI: 10.1007/BF02653870.

[34] R. Schwarze and F. Obermeier. "Modelling of Unsteady Electromagnetically Driven Recirculating Melt Flows". In: *Modelling and Simulation in Materials Science and Engineering* 12.5 (2004), pp. 985–993. DOI: 10.1088/0965-0393/12/5/015.

[35] A. Umbrashko et al. "Modeling of the Turbulent Flow in Induction Furnaces". In: *Metallurgical and Materials Transactions B: Process Metallurgy and Materials Processing Science* 37.5 (2006), pp. 831–838. DOI: 10.1007/s11663-006-0065-0.

[36] A. Umbrashko et al. "Thermal and Hydrodynamic Analysis of the Melting Process in the Cold Crucible Using 3D Modeling". In: *Heat Transfer Research* 39.5 (2008), pp. 413–421. DOI: 10.1615/HeatTransRes.v39.i5.50.

[37] E. Baake et al. "Numerical Modelling of Metallurgical Processes Using LES". In: *Archives of Electrical Engineering* 54.214 (2005), pp. 425–437.

[38] E. Baake et al. "Experimental and Numerical Investigations of the Temperature Field and Melt Flow in the Induction Furnace with Cold Crucible". In: *COMPEL - The International Journal for Computation and Mathematics in Electrical and Electronic Engineering* 22.1 (2003), pp. 88–97. DOI: 10.1108/03321640310452196.

[39] E. Baake et al. “Turbulent Flow Dynamics, Heat Transfer and Mass Exchange in the Melt of Induction Furnaces”. In: *COMPEL - The International Journal for Computation and Mathematics in Electrical and Electronic Engineering* 22.1 (2003), pp. 39–47. DOI: 10.1108/03321640310452006.

[40] M. Ščepanskis. “The Modelling of the Behaviour of Solid Inclusions in the EM Induced Recirculated Turbulent Flows of Liquid Metal”. PhD thesis. University of Latvia, 2013.

[41] S. Spitans et al. “Numerical Modeling of Free Surface Dynamics of Melt in an Alternate Electromagnetic Field: Part I. Implementation and Verification of Model”. In: *Metallurgical and Materials Transactions B* 44.3 (2013), pp. 593–605. DOI: 10.1007/s11663-013-9809-9.

[42] P. Buliński et al. “Numerical Modelling of Multiphase Flow and Heat Transfer within an Induction Skull Melting Furnace”. In: *International Journal of Heat and Mass Transfer* 126 (2018), pp. 980–992. DOI: 10.1016/j.ijheatmasstransfer.2018.06.074.

[43] M. Kirpo et al. “Particle Transport in Recirculated Liquid Metal Flows”. In: *COMPEL - The International Journal for Computation and Mathematics in Electrical and Electronic Engineering* 27.2 (2008), pp. 377–386. DOI: 10.1108/03321640810847661.

[44] M. Ščepanskis et al. “Solid Inclusions in an Electromagnetically Induced Recirculated Turbulent Flow: Simulation and Experiment”. In: *International Journal of Multiphase Flow* 64 (2014), pp. 19 –27. DOI: 10.1016/j.ijmultiphaseflow.2014.04.004.

[45] M. Ščepanskis et al. “Statistical Analysis of the Influence of Forces on Particles in EM Driven Recirculated Turbulent Flows”. In: *Journal of Physics: Conference Series* 333.1 (2011), pp. 012–015. DOI: 10.1088/1742-6596/333/1/012015.

[46] H. Barati et al. “Assessment of Different Turbulence Models for the Motion of Non-metallic Inclusion in Induction Crucible Furnace”. In: *IOP Conference Series: Materials Science and Engineering* 143.1 (2016), pp. 012–026. DOI: 10.1088/1757-899x/143/1/012026.

[47] K. H. K. Chung et al. “Local Gas and Liquid Phase Velocity Measurement in a Miniature Stirred Vessel Using PIV Combined with a New Image Processing Algorithm”. In: *Experimental Thermal and Fluid Science* 33.4 (2009), pp. 743–753. DOI: 10.1016/j.expthermflusci.2009.01.010.

[48] A. Gabriele et al. “Use of PIV to Measure Turbulence Modulation in a High Throughput Stirred Vessel with the Addition of High Stokes number Particles for Both Up- and own-Pumping configurations”. In: *Chemical Engineering Science* 66.23 (2011), pp. 5862–5874. DOI: 10.1016/j.ces.2011.08.007.

[49] A. Gabriele et al. “Use of Angle Resolved PIV to Estimate Local Specific Energy Dissipation Rates for up- and Down-Pumping Pitched Blade Agitators in a Stirred Tank”. In: *Chemical Engineering Science* 64.1 (2009), pp. 126–143. DOI: 10.1016/j.ces.2008.09.018.

[50] F. Alberini et al. “Comparison between 3-D-PTV and 2-D-PIV for Determination of Hydrodynamics of Complex Fluids in a Stirred Vessel”. In: *Chemical Engineering Science* 171 (2017), pp. 189–203. DOI: 10.1016/j.ces.2017.05.034.

[51] B. Liu et al. “Experimental Study on the Mixing and Dispersing of Floating Particles in Viscous System”. In: *The Canadian Journal of Chemical Engineering* 94.10 (2016), pp. 2013–2022. DOI: 10.1002/cjce.22581.

[52] S. Motamedvaziri and P. M. Armenante. “Flow Regimes and Surface Air Entrainment in Partially Filled Stirred Vessels for Different Fill Ratios”. In: *Chemical Engineering Science* 81 (2012), pp. 231–250. DOI: 10.1016/j.ces.2012.05.050.

[53] D. P. Karadimou et al. “Mathematical Modelling and Numerical Simulation of Two-phase Gas-liquid Flows in Stirred Tank Reactors”. In: *Journal of King Saud University - Science* (2017). DOI: 10.1016/j.jksus.2017.05.015.

[54] B. A. Ali et al. “Numerical Analysis of Hydrodynamics and Crystal Motion in a Batch Crystallizer”. In: *Journal of Crystal Growth* 372 (2013), pp. 219 –229. DOI: 10.1016/j.jcrysgro.2013.01.041.

[55] H. Bashiri et al. “Investigation of Turbulent Fluid Flows in Stirred Tanks Using a Non-intrusive Particle Tracking Technique”. In: *Chemical Engineering Science* 140 (2016), pp. 233 –251. DOI: 10.1016/j.ces.2015.10.005.

[56] M. Soos et al. “Determination of Maximum Turbulent Energy Dissipation Rate Generated by a Rushton Impeller Through Large Eddy Simulation”. In: *AIChE Journal* 59.10 (2013), pp. 3642–3658. DOI: 10.1002/aic.14206.

[57] S. Malik et al. “Shear Improved Smagorinsky model for Large Eddy Simulation of Flow in a Stirred Tank with a Rushton Disk Turbine”. In: *Chemical Engineering Research and Design* 108 (2016), pp. 69–80. DOI: 10.1016/j.cherd.2016.02.035.

[58] J. E. Dore et al. Pat. 3,962,081. 1976.

[59] K. Schwartzwalder and A.V. Somers. Pat. 3,090,094.

[60] A. R. Studart et al. “Processing Routes to Macroporous Ceramics: A Review”. In: *Journal of the American Ceramic Society* 89.6 (2006), pp. 1771–1789. DOI: 10.1111/j.1551-2916.2006.01044.x.

[61] Y. H. Yang et al. “Effect of Revert Addition on Microstructure and Mechanical Properties of M951 Ni-base Superalloy”. In: *Materials Science and Engineering: A* 532 (2012), pp. 6 –12. DOI: 10.1016/j.msea.2011.10.054.

[62] P. Bakke et al. “Magnesium Filtration with Ceramic Foam Filters and Subsequent Quantitative Microscopy of the Filters”. In: *Materials and Manufacturing Processes* 9.1 (1994), pp. 111–138. DOI: 10.1080/10426919408934888.

[63] J. Wang et al. “Influence of Melt Purification on Mechanical Properties of AZ31 Magnesium Alloy”. In: *International Journal of Cast Metals Research* 25.3 (2012), pp. 165–169. DOI: 10.1179/1743133611Y.0000000015.

[64] K. Stránský et al. “Re-oxidation Phenomena During the Filtration of Steel by Means of Ceramic Filters”. In: *Materials and Technology* 5 (2008).

[65] C. Settgast et al. “Fracture Mechanical Analysis of Open Cell Ceramic Foams Under Thermal Shock Loading”. In: *Journal of Multiscale Modelling* 07.04 (2016), p. 1640006. DOI: 10.1142/S1756973716400060.

[66] M. Scheffler and P. Colombo. *Cellular Ceramics: Structure, Manufacturing, Properties and Applications*. Wiley-VCH Verlag, 2005. ISBN: 978-3527606702.

[67] R. N. Sacramento et al. “Deep Bed and Cake Filtration of Two-size Particle Suspension in Porous Media”. In: *Journal of Petroleum Science and Engineering* 126 (2015), pp. 201 –210. DOI: 10.1016/j.petrol.2014.12.001.

[68] A. Rushton et al. *Solid-Liquid Filtration and Separation Technology*. Wiley-VCH Verlagsgesellschaft mbH, 2008. ISBN: 978-3527614967.

[69] D. Janke and K. Raiber. *Grundlegende Untersuchungen zur Optimierung der Filtration von Stahlschmelzen*. Amt für Amtliche Veröffentlichungen der Europäischen Gemeinschaften, 1996. ISBN: 978-9282764589.

[70] K. Uemura et al. "Filtration Mechanism of Non-metallic Inclusions in Steel by Ceramic Loop Filter". In: *ISIJ International* 32.1 (1992), pp. 150–156. DOI: 10.2355/isijinternational.32.150.

[71] G. Kasper et al. "Structure and Density of Deposits Formed on Filter Fibers by Inertial Particle Deposition and Bounce". In: *Journal of Aerosol Science* 41.12 (2010), pp. 1167 –1182. DOI: 0.1016/j.jaerosci.2010.08.006.

[72] S. Bao et al. "Inclusion (particle) Removal by Interception and Gravity in Ceramic Foam Filters". In: *Journal of Materials Science* 47.23 (2012), pp. 7986–7998. DOI: 10.1007/s10853-012-6688-4.

[73] F. Heuzeroth et al. "Wetting and its Influence on the Filtration Ability of Ceramic Foam Filters". In: *Particuology* 18 (2015), pp. 50 –57. DOI: 10.1016/j.partic.2014.06.001.

[74] L. Ditscherlein et al. "Impact of the Roughness of Alumina and Al2O3–C Substrates on the Adhesion Mechanisms in a Model System". In: *Advanced Engineering Materials* 19.9 (2017), p. 1700088. DOI: 10.1002/adem.201700088.

[75] C. G. Aneziris et al. Pat. DE201110109681. 2013.

[76] C. G. Aneziris et al. Pat. DE201110109684. 2013.

[77] A. Asad et al. "Numerical Assessment of a Filtration Experiment Influenced by Microscale Carbon Monoxide Bubbles Arising in Steel Melt". In: *JOM* 70.12 (2018), pp. 2927–2933. DOI: 10.1007/s11837-018-3117-4.

[78] A. Schmidt et al. "Functionalized Carbon-Bonded Filters with an Open Porous Alumina Coating: Impact of Time on Interactions and Steel Cleanliness". In: *Advanced Engineering Materials* 19.9 (2017), p. 1700170. DOI: 10.1002/adem.201700170.

[79] E. Storti. “Functionalization of Carbon-bonded Ceramic foam Filters With Nano-scaled Materials for Steel Melt Filtration”. PhD thesis. Technischen Universität Bergakademie Freiberg, 2018.

[80] D. Rzehak. “Beschleunigte Entkohlung von Stahlschmelzen im Vakuum durch Kombination von Sauerstoff und Metalloxiden”. PhD thesis. RWTH Aachen, 2013.

[81] M. Cournil et al. “Modelling of Solid Particle Aggregation Dynamics in Non-wetting Liquid Medium”. In: *Chemical Engineering and Processing: Process Intensification* 45.7 (2006), pp. 586 –597. DOI: 10.1016/j.cep.2006.01.003.

[82] S. Yang et al. “Characterization of Nanobubbles on Hydrophobic Surfaces in Water”. In: *Langmuir* 23.13 (2007), pp. 7072–7077. DOI: 10.1021/la070004i.

[83] D. Lohse and X. Zhang. “Surface nanobubbles and nanodroplets”. In: *Rev. Mod. Phys.* 87 (2015), pp. 981–1035. DOI: 10.1103/RevModPhys.87.981.

[84] O. Dávila-Maldonado et al. “Simulation of Fluid and Inclusions Dynamics during Filtration Operations of Ductile Iron Melts Using Foam Filters”. In: *Metallurgical and Materials Transactions B* 39.6 (2008), pp. 818–839. DOI: 10.1007/s11663-008-9190-2.

[85] M. W. Kennedy et al. “Characterization of Ceramic Foam Filters Used for Liquid Metal Filtration”. In: *Metallurgical and Materials Transactions B* 44.3 (2013), pp. 671–690. DOI: 10.1007/s11663-013-9799-7.

[86] H. Hwang et al. “A Study on Effects of Ceramic Foam Filter on Flow Aspect Through Water Modeling Experiment”. In: *China Foundry* 14.3 (2017), pp. 216–225. DOI: 10.1007/s41230-017-6108-0.

[87] H. Hashemi and R. Raiszadeh. “Naturally-Pressurized Running Systems: The Role of Ceramic Filters”. In: *Journal of Applied Sciences,* 9 (2009), pp. 2115–2122. DOI: 10.3923/jas.2009.2115.2122.

[88] L. N. W. Damoah and L. Zhang. “Removal of Inclusions from Aluminum Through Filtration”. In: *Metallurgical and Materials Transactions B* 41.4 (2010), pp. 886–907. DOI: 10.1007/s11663-010-9367-3.

[89] E. Werzner et al. “Influence of Foam Morphology on Effective Properties Related to Metal Melt Filtration”. In: *Advanced Engineering Materials* 19.9 (2017), p. 1700240. DOI: 10.1002/adem.201700240.

[90] C. Demuth et al. “Non-Isothermal Simulations of Aluminum Depth Filtration”. In: *Advanced Engineering Materials* 19.9 (2017), p. 1700238. DOI: 10.1002/adem.201700238.

[91] C. Tian et al. “Analyses of the dynamic processes of liquid metal filtration”. In: *Metallurgical and Materials Transactions B* 30.5 (1999), pp. 891–900. DOI: 10.1007/s11663-999-0094-6.

[92] E. Laé et al. “Experimental and Numerical Study of Ceramic Foam Filtration”. In: Cham: Springer International Publishing, 2006, pp. 285–290. ISBN: 978-3319482286.

[93] OpenFOAM Foundation Ldt. URL: http://www.openfoam.org.

[94] H. K. Versteeg and W. Malalasekera. *An Introduction to Computational Fluid Dynamics: The Finite Volume Method*. Pearson Prentice Hall, 2007. ISBN: 978-0131274983.

[95] S. V. Patankar. *Numerical Heat Transfer and Fluid Flow*. Electro Skills Series. Hemisphere Publishing Corporation, 1980. ISBN: 978-0070487406.

[96] P. A. Davidson. *An Introduction to Magnetohydrodynamics*. Cambridge Texts in Applied Mathematics. Cambridge University Press, 2001. ISBN: 978-0511626333.

[97] R. J. Moreau. *Magnetohydrodynamics (Fluid Mechanics and Its Applications)*. Springer, 1990. ISBN: 978-0792309376.

[98] J. M. Galpin and Y. Fautrelle. “Liquid-metal Flows Induced by Low-frequency Alternating Magnetic Fields”. In: *Journal of Fluid Mechanics* 239 (1992), pp. 383–408. DOI: 10.1017/S0022112092004452.

[99] F. Felten et al. “Numerical Modelling of Electromagnetically-driven Turbulent Flows Using LES Methods”. In: *Applied Mathematical Modelling* 28.1 (2004), pp. 15 –27. DOI: 10.1016/S0307-904X(03)00116-1.

[100] MaxFEM. *Universidade de Santiago de Compostela*. URL: http://www.usc.es.

[101] A. Bermúdez et al. “The eddy currents model”. In: *Mathematical Models and Numerical Simulation in Electromagnetism*. Cham: Springer International Publishing, 2014, pp. 183–216. ISBN: 978-3319029481.

[102] S. Maneewongvatana and D. M. Mount. “Analysis of Approximate Nearest Neighbor Searching with Clustered Point Sets”. In: *Data Structures, Near Neighbor Searches, and Methodology* 59 (2002), pp. 105–123. DOI: 10.1090/dimacs/059.

[103] F. R. Menter. “Two-equation Eddy-Viscosity Turbulence Models for Engineering Applications”. In: *AIAA journal* 32.8 (1994), pp. 1598–1605. DOI: 10.2514/3.12149.

[104] B. E. Launder and D. B. Spalding. “The Numerical Computation of Turbulent Flows”. In: *Computer Methods in Applied Mechanics and Engineering* 3.2 (1974), pp. 269–289. DOI: 10.1016/0045-7825(74)90029-2.

[105] D. C. Wilcox. “Reassessment of the Scale-Determining Equation for Advanced Turbulence Models”. In: *AIAA journal* 26.11 (1988), pp. 1299–1310. DOI: 10.2514/3.10041.

[106] F. R. Menter and T. Esch. “Elements of Industrial Heat Transfer Predictions”. In: *16th Brazilian Congress of Mechanical Engineering (COBEM)*. Uberlandia, Minas Gerais, Brazil, 2001, pp. 117–127.

[107] A. Hellsten. “Some Improvements in Menter’s k-omega SST Turbulence Model”. In: *29th AIAA, Fluid Dynamics Conference*. Albuquerque,NM,U.S.A, 1998, pp. 1–11. DOI: 10.2514/6.1998-2554.

[108] F. R. Menter et al. “Ten Years of Industrial Experience with the SST Turbulence Model”. In: *the 4th International Symposium on Turbulence, Heat and Mass Transfer*. Antalya, Turkey, 2003, pp. 625–632.

[109] F. R. Menter and Y. Egorov. “A Scale Adaptive Simulation Model using Two-Equation Models”. In: *43rd AIAA Aerospace Sciences Meeting and Exhibit*. Reno, Nevada, 2005. DOI: 10.2514/6.2005-1095.

[110] F. R. Menter and Y. Egorov. “The Scale-Adaptive Simulation Method for Unsteady Turbulent Flow Predictions. Part 1: Theory and Model Description”. In: *Flow, Turbulence and Combustion* 85.1 (2010), pp. 113–138. DOI: 10.1007/s10494-010-9264-5.

[111] Y. Egorov and F. Menter. “Development and Application of SST-SAS Turbulence Model in the DESIDER Project”. In: Berlin, Heidelberg: Springer Berlin Heidelberg, 2008, pp. 261–270. ISBN: 978-3540778158.

[112] F. Nicoud and F. Ducros. “Subgrid-scale Stress Modelling Based on the Square of the Velocity Gradient Tensor”. In: *Flow, Turbulence and Combustion* 62.3 (1999), pp. 183–200. DOI: 10.1023/A:1009995426001.

[113] S. Hickel. “Implicit Turbulence Modeling for Large-Eddy Simulation”. PhD thesis. 2008.

[114] F. Grinstein et al. *Implicit Large Eddy Simulation: Computing Turbulent Fluid Dynamics*. Cambridge University Press, 2007. ISBN: 978-1900364966.

[115] A. Asad et al. “Numerical Modeling of Flow Conditions during Steel Filtration Experiments”. In: *Advanced Engineering Materials* 19.9 (2017), p. 1700085. DOI: 10.1002/adem.201700085.

[116] L. Cheng and D. Mewes. *Advances in Multiphase Flow and Heat Transfer*. Bentham Science Publishers, 2012. ISBN: 978-1608055005.

[117] E. Michaelides et al. *Multiphase Flow Handbook, Second Edition*. Boca Raton: CRC Press, 2016. ISBN: 978-1498701006.

[118] E. Loth. “Numerical Approaches for Motion of Dispersed Particles, Droplets and Bubbles”. In: *Progress in Energy and Combustion Science* 26.3 (2000), pp. 161 –223. DOI: 10.1016/S0360-1285(99)00013-1.

[119] S. Elghobashi. “On Predicting Particle-laden Turbulent Flows”. In: *Applied Scientific Research* 52.4 (1994), pp. 309–329. DOI: 10.1007/BF00936835.

[120] R. Clift et al. *Bubbles, Drops, and Particles*. London: Academic Press, 1978. ISBN: 978-0486445809.

[121] C. T. Crowe et al. *Multiphase Flows with Droplets and Particles*. Boca Raten, Florida: CRC press, 1998. ISBN: 978-1439840504.

[122] A. B. Liu et al. “Modeling the Effects of Drop Drag and Breakup on Fuel Sprays”. In: *SAE Technical Paper*. SAE International, 1993. DOI: 10.4271/930072.

[123] A. Putnam. “Integrable Form of Droplet Drag Coefficient”. In: *ARS J.* 31.10 (1961), pp. 1467–1470.

[124] F. Odar. “Verification of the Proposed Equation for Calculation of the Forces on a Sphere Accelerating in a Viscous Fluid”. In: *Journal of Fluid Mechanics* 25.3 (1966), 591–592. DOI: 10.1017/S0022112066000272.

[125] P. G. Saffman. “The Lift on a Small Sphere in a Slow Shear Flow”. In: *Journal of Fluid Mechanics* 22 (02 1965), pp. 385–400. DOI: 10.1017/S0022112065000824.

[126] R. Mei. “An Approximate Expression for the Shear Lift Force on a Spherical Particle at Finite Reynolds Number”. In: *International Journal of Multiphase Flow* 18.1 (1992), pp. 145–147. DOI: 10.1016/0301-9322(92)90012-6.

[127] Q. Wang et al. “Behavior of Non-metallic Inclusions in a Continuous Casting Tundish with Channel Type Induction Heating”. In: *ISIJ International* 54.12 (2014), pp. 2796–2805. DOI: 10.2355/isijinternational.54.2796.

[128] K. Takahashi and S. Taniguchi. “Electromagnetic Separation of Nonmetallic Inclusion from Liquid Metal by Imposition of High Frequency Magnetic Field”. In: *ISIJ International* 43.6 (2003), pp. 820–827. DOI: 10.2355/isijinternational.43.820.

[129] D. Leenov and A. Kolin. “Theory of Electromagnetophoresis. I. Magnetohydrodynamic Forces Experienced by Spherical and Symmetrically Oriented Cylindrical Particles”. In: *The Journal of Chemical Physics* 22.4 (1954), pp. 683–688. DOI: 0.1063/1.1740149.

[130] M. Ščepanskis et al. “Statistical Analysis of the Influence of Forces on Particles in EM Driven Recirculated Turbulent Flows”. In: *Journal of Physics: Conference Series* 333.1 (2011). DOI: 10.1088/1742-6596/333/1/012015.

[131] M. Ščepanskis et al. “Analysis of the Oscillating Behaviour of Solid Inclusions in Induction Crucible Furnaces”. In: *Magnetohydrodynamics* 48.4 (2012), pp. 677–686.

[132] D. Mazumdar and J. W. Evans. *Modeling of steelmaking processes*. CRC press, 2009. ISBN: 978-1420062434.

[133] R. I. L. Guthrie. *Engineering in Process Metallurgy*. Oxford Science Publications (Clarendon Press, 1992), 1992. ISBN: 978-0198563679.

[134] J. Smagorinsky. "General Circulation Experiments with the Primitive Equations". In: *Monthly Weather Review* 91.3 (1963), pp. 99–164. DOI: 10.1175/1520-0493(1963)091<0099:GCEWTP>2.3.CO;2.

[135] H. Kim et al. "Forward and Backward Reaction Rate Constants of the Reaction of C+O=CO (g) on Fe–C Melts". In: *ISIJ International* 50.5 (2010), pp. 678–685. DOI: 10.2355/isijinternational.50.678.

[136] A. Asad et al. "Numerical Investigation of Filtration Influenced by Microscale CO Bubbles in Steel Melt". In: *Advanced Engineering Materials* 22.2 (2020), p. 1900591. DOI: 10.1002/adem.201900591.

[137] L. Ditscherlein et al. "The Influence of Nanobubbles on the Interaction Forces between Alumina Particles and Ceramic Foam Filters". In: *Powder Technology* 357 (2019), pp. 408 –416. DOI: 10.1016/j.powtec.2019.08.077.

[138] M. Sommerfeld and S. Stübing. "A novel Lagrangian agglomerate structure model". In: *Powder Technology* 319 (2017), pp. 34 –52. DOI: 10.1016/j.powtec.2017.06.016.

[139] A. Asad et al. "Numerical and Experimental Modeling of the Recirculating Melt Flow Inside an Induction Crucible Furnace". In: *Metallurgical and Materials Transactions B* (2018), pp. 1543–1916. DOI: 10.1007/s11663-018-1200-4.

[140] F. Stefani et al. "Contactless Inductive Flow Tomography". In: *Physical Review E* 70.5 (2004), p. 056306. DOI: 10.1103/PhysRevE.70.056306.

[141] C. Heinicke and T. Wondrak. "Spatial and Temporal Resolution of a Local Lorentz Force Flowmeter". In: *Measurement Science and Technology* 25.5 (2014), p. 055302. DOI: 10.1088/0957-0233/25/5/055302.

[142] DaVis 8.4.0. URL: https://www.lavision.de/.

[143] M. Sommerfeld and S. Decker. "State of the Art and Future Trends in CFD Simulation of Stirred Vessel Hydrodynamics". In: *Chemical Engineering & Technology* 27.3 (2004), pp. 215–224. DOI: 10.1002/ceat.200402007.

[144] Creative Fields Holding Ldt. URL: https://cfmesh.com/.

[145] X. Jiang and C. Lai. *Numerical Techniques for Direct and Large-Eddy Simulations*. CRC press, 2009. ISBN: 978-1138113831.

[146] S. Rezaeiravesh and M. Liefvendahl. "Effect of Grid Resolution on Large Eddy Simulation of Wall-bounded Turbulence". In: *Physics of Fluids* 30.5 (2018), p. 055106. DOI: 10.1063/1.5025131.

[147] A. Asad et al. "Effect of Turbulence Modeling on the Melt Flow and Inclusions Transport in a Steel Filtration Experiment". In: *Metallurgical and Materials Transactions B* 49.5 (2018), pp. 2270–2277. DOI: 10.1007/s11663-018-1343-3.

[148] S. B. Pope. *Turbulent Flows*. Cambridge University Press, 2000. ISBN: 978-0521598866.